Synthesis of Micelle-Templated Metal Oxides as Catalysts for the Oxidative Coupling of Methane

vorgelegt von
Diplom-Chemiker Björn Eckhardt
aus Königs Wusterhausen

Von der Fakultät II - Mathematik und Naturwissenschaften
der Technischen Universität Berlin
zur Erlangung des akademischen Grades
Doktor der Naturwissenschaften
Dr. rer. nat.

genehmigte Dissertation

Promotionsausschuss:

Vorsitzender:	Prof. Dr. rer. nat. Martin Schoen
Gutachter:	Prof. Dr. rer. nat. Peter Strasser
Gutachter:	Prof. Dr. rer. nat. Michael Wark
Gutachter:	Dr.-Ing. Ralph Krähnert

Tag der wissenschaftlichen Aussprache: 01.04.2014

Berlin 2014
D83

"This would be the way of the misanthrope,
in order to create you must destroy"
Satyricon - Prime Evil Renaissance

Danksagung

Hiermit möchte ich mich bei allen Menschen bedanken die mich im Entstehen dieser Arbeit unterstützt haben:

Ganz besonders möchte ich mich bei Dr.-Ing. Ralph Krähnert bedanken, der mir erlaubt hat die vorliegende Arbeit in seinem Arbeitskreis anzufertigen. Vielen Dank für die vielen zielorientierten Diskussionen der experimentellen Daten und der Versuchsplanung sowie für die gewährte Freiheit meine eigenen Lösungswege zu finden. Ralph Krähnerts Fähigkeit Arbeit und Gedankengänge logisch zu strukturieren, haben mich weit über die Wissenschaft hinaus geprägt.

Ich danke Prof. Peter Strasser für seine Beiträge zu unseren gemeinsamen Veröffentlichungen, ebenso wie für die Möglichkeit seine Labore zu nutzen. Außerdem danke ich ihm für die Übernahme des Erstgutachtens.

Prof. Michael Wark danke ich für die Bereitschaft zur Übernahme des Zweitgutachtens.

Für die finanzielle Unterstützung danke ich dem Exzellenzcluster "Unifying Concepts in Catalysis" (UniCat) der Deutschen Forschungsgemeinschaft, sowie Prof. Peter Strasser und Dr. Anna Fischer.

Dr. Stefan Enthaler danke ich nicht nur für die Möglichkeit sein FTIR zu verwenden, sondern vor allem für seine Freundschaft und die vielen inspirierenden Gespräche. Dr. Ulla Vainio danke ich für die Unterstützung bei SAXS Messungen. Vielen Dank auch an Dr. Oliver Görke und Gregor Koch für die Unterstützung bei thermogravimetrischen Untersuchungen. Sören Selve sowie dem ganzen ZELMI-Team danke ich für die Unterweisung in der Anwendung des TEM und das Wissen über Elektronenmikroskopie, das ich als große Bereicherung meines Erfahrungsschatzes erachte. Evgenii Kondratenko danke ich für die OCM-Messungen am Leibnitz Institut für Katalyse in Rostock. Dem Massenspektrometrie Service der TU Berlin unter Leitung von Maria Schlangen danke ich ebenfalls für seine Hilfe. Dr. Franziska Emmerling danke ich für den Rat in XRD Fragen, sowie für ihren Beitrag zur gemeinsamen Veröffentlichung.

Mein allergrößter Dank gebührt meinen lieben Kollegen des Arbeitskreises Krähnert. Kornelia Weh für die Unterstützung im Labor, bei ICP-OES Messungen und den vielen aufbauenden Gesprächen. Benjamin Paul danke ich für seine praktischen Ratschläge, seine fast künstlerischen Fähigkeiten am Rasterelektronenmikroskop sowie für die unzähligen interessanten Gespräche jenseits der Forschung. Erik Ortel, Denis Bernsmeier, Michael Bernicke und Roman Schmack danke ich für fruchtbare wissenschaftliche Diskussionen sowie die Stunden grenzenlosen Spaßes. Dr. Jörg Polte und Maria Wuithschick danke ich für die vielen wissenschaftlichen und kulturellen Diskussionen als auch für die anstrengenden und doch lustigen Stunden während der Synchrotronmesszeiten sowie nach der Arbeit.

Außerdem danke ich dem AK Strasser für die angenehme Zerstreuung während der Kaffeepausen. Ganz besonders danke ich Arno Bergmann für die tolle Atmosphäre im Büro und unseren freundschaftlichen Umgang.

Natürlich danke ich ganz besonders meinen Eltern, die mir mein Leben geschenkt und versüßt haben. Die nicht nur als Eltern sondern vor allem als Freunde immer an meiner Seite stehen. Auch meiner Schwerster Sabine und ihrem Mann Martin Eckhardt danke ich für ihre moralische Unterstützung, Liebe und Freundschaft. Weiterhin danke ich all meinen Freunden und Freundinnen für Spaß und Inspiration neben der Arbeit.

Zusammenfassung

In der vorliegenden Arbeit werden Synthesen von Modellkatalysatoren für die oxidative Kupplung von Methan ("oxidative coupling of methane", OCM) mit mizell-templatierter Porosität vorgestellt. Die erhaltenen Katalysatoren wurden in der OCM getestet um den Einfluss der Porengröße auf die C_2-Selektivität zu untersuchen.

Die Synthese von MgO und Li@MgO OCM Katalysator wurde zunächst für mesoporöse MgO-Filme entwickelt. Das neue Synthesekonzept ermöglicht neben der Herstellung von geordnet mesoporösen MgO-Filmen auch die Herstellung von mizell-templatierten Schichten von Al_2O_3, ZnO und Co_3O_4, sowie von den templatierter Karbonaten der Metalle Magnesium, Aluminium, Zink und Kobalt, über deren Synthese bis jetzt nicht berichtet wurde. Der Schlüssel zur erfolgreichen Synthese liegt in der Verwendung eines für EISA-basierende Ansätze neuartigen chemischen Komplexes aus Metallnitrat und Zitronensäure als Materialvorstufe. Die chemische Zusammensetzung der Komplexe sowie deren thermische Zersetzungsverhalten wurden in Abhängigkeit des Metallions untersucht und die Kriterien für eine erfolgreiche Filmsynthese abgeleitet. Die erhaltenen mizelltemplatierten Filme wurden im Hinblick auf ihre chemische Zusammensetzung, ihre Kristallinität und ihre Morphologie charakterisiert. Die Vielseitigkeit des neuen Konzeptes konnte durch die Synthese von ZnO mit verschiedenen Porensystem demonstriert werden. Schließlich werden die Kriterien für eine erfolgreiche Anwendung des neuen Synthesekonzepts sowie die Einschränkung im Detail abgeleitet.

Nach der erfolgreichen Herstellung von mizelltemplatierten MgO-Filmen wurde das Synthesekonzept übertragen, um so MgO und Li@MgO-Pulver als OCM Katalysator zu erhalten. Die Synthese und die Charakterisierung in Bezug auf Porenmorphologie und Kristallinität der resultierenden MgO-Pulver werden in dieser Arbeit vorgestellt und die katalytische Performance in der OCM Reaktion diskutiert. Weiterhin werden die morphologischen und kompositorischen Eigenschaften der Katalysatoren nach der Katalysetestung mit den Eigenschaften frisch präparierter Katalysatoren verglichen und die Auswirkung der Restrukturierung auf die OCM-Performance diskutiert.

Neben MgO und Li@MgO wurden in dieser Arbeit auch W-Mn/SiO_2 Katalysatoren mit kontrollierter Mesoporösität hergestellt, charakterisiert und ihre Performance während der OCM getestet. Es konnte gezeigt werden, dass das neu entwickelte Syntheseverfahren W-Mn/SiO_2 Katalysatoren mit enger Porengrößenverteilung und kontrollierter Porenstruktur liefert. Unter Verwendung von Polymertemplaten verschiedener Größe wurde die Porengröße in acht Stufen zwischen 3,5 und 18 nm eingestellt. Die so erhaltenen Katalysatoren sind aktiv und selektiv in der OCM. In der vorliegenden Arbeit wird der Einfluss des initialen Porendurchmessers auf die C_2-Selektivität der OCM bei 775 °C und 800 °C untersucht und die Ergebnisse im Hinblick auf mechanistische Aspekte der OCM diskutiert. Des Weiteren werden die Auswirkungen der katalytischen Tests auf die Morphologie und die Phasenzusammensetzung des Katalysators nach der Katalyse analysiert. Schließlich wird die Phasenzusammensetzung und OCM-Performance der synthetisierten W-Mn/SiO_2 Katalysatoren mit den Ergebnissen der Literatur verglichen und der Einfluss des Porendurchmessers auf die C_2-Selektivität in der OCM diskutiert.

Abstract

In this thesis, novel procedures for the synthesis of model catalysts for the oxidative coupling of methane (OCM) with micelle-templated mesoporosity are presented. The obtained catalysts were tested in the OCM reaction in order to investigate the influence of the pore diameter on the C_2-selectivity.

At first, a synthetic procedure for MgO and Li@MgO OCM catalysts was developed for films. In addition to mesoporous MgO, the new concept enables the preparation of Al_2O_3, ZnO und Co_3O_4 films with templated mesoporosity. Moreover, micelle-structured carbonate films of magnesium, aluminium, zinc and cobalt become accessible for first time. The new synthesis concept is based on chemical complexes as new type of material precursor in EISA-based synthesis which are formed by metal nitrate and citric acid. The chemical compositions of the complexes as well as their thermal decomposition behaviour were analysed in dependence of the metal ions allowing the deduction of criteria necessary for the successful synthesis of micelle-templated films. The chemical composition, crystallinity and morphology of the resulting metal carbonate and oxide films were characterized. In addition, the versatility of the new synthesis concept is demonstrated by synthesizing ZnO films with different pore systems. Finally, the criteria for a successful synthesis as well as the limitation of the new synthesis concept are discussed.

After the successful preparation of the MgO-films, the synthesis concept was transferred to obtain MgO and Li@MgO-powders. The synthesis of this MgO-based OCM catalysts is described and the characterisation of the pore system as well as the phase composition are presented in this thesis. The obtained MgO-based powders were tested in OCM reaction and the catalytic results of the active and selective catalysts are discussed in detail. Moreover, the morphological and compositional characterisation of MgO and Li@MgO-powders after catalytic testing are presented and compared to the freshly prepared OCM catalysts. Thereafter, the effect of the morphological restructuring of MgO-based powders during OCM reaction is discussed and the catalytic results are compared to the literature.

In addition to the MgO-based materials, a synthesis for W-Mn/SiO_2 OCM catalysts with templated mesoporosity is developed. It is shown that the developed synthesis yields OCM catalyst with a narrow pore size distribution and controlled pore structure. Employing different sized templates enabled the variation of the pore diameters in eight steps between 3.5 nm and 18 nm in the OCM catalysts. The resulting catalysts were active and selective in the OCM reaction. The influence of the initial pore diameter on the C_2-selectivity at 775 °C and 800 °C are analysed and the results are discussed with a focus on mechanistic aspects of the OCM reaction. Moreover, the morphological restructuring as well as the phase composition of the catalyst after OCM testing is analysed. Finally, the phase composition and OCM performance is compared to the literature and the influence of the pore diameter on the C_2-selectivity on the OCM reaction is discussed.

Contents

1. Motivation

The threat of a potential world energy crisis and exhaustion of fossil oil reserves requires material science to develop new solutions. Many promising solutions rely on heterogeneous catalysis, electrocatalysis or photocatalysis carried out on metal oxides. Especially the investigation of metal oxides as versatile materials not only for the chemical industry can contribute to overcome the challenges of the current century.

One challenge for material science is the effective use of solar energy. The metal oxide ZnO as a cost-efficient transparent conducting oxide can be applied as electrode material for photovoltaic devices. The gathered solar energy can be stored in chemical energy carriers (for example hydrogen) when not used directly. This energy conversion can be accomplished e.g. by electrochemical water splitting. The metal oxide Co_3O_4 is a promising electrocatalyst for the oxygen evolution reaction (OER),[1] which is the challenging half cell reaction of electrochemical water splitting. Although the conversion of sunlight into a chemical fuel in form of hydrogen is an attractive route, the efficiency of light harvesting as well as water splitting have yet to be increased to an economically interesting level.[2]

Besides electrochemistry, metal oxides are widely applied as catalyst and catalyst supports in heterogenous catalysis. The performance of catalysts often benefits from a high surface area of the material. A materials specific surface area can be increased by introduction of small pores. Unfortunately, the need for fast diffusion of catalytic reactants in porous systems prohibits too small pores. Hence, mesoporous materials often provide the best compromise between high surface area and fast mass transport. Therefore, control over the pore size is needed to tailor optimized catalyst systems.

Pore size potentially plays also an essential role in the catalytic oxidative coupling of methane (OCM). The OCM reaction converts methane into higher alkanes and alkenes, mainly ethane and ethylene. Therefore, the OCM can contribute to cover the demands of many branches of the chemical industry for olefins by employing fossil or bio gas as starting material.

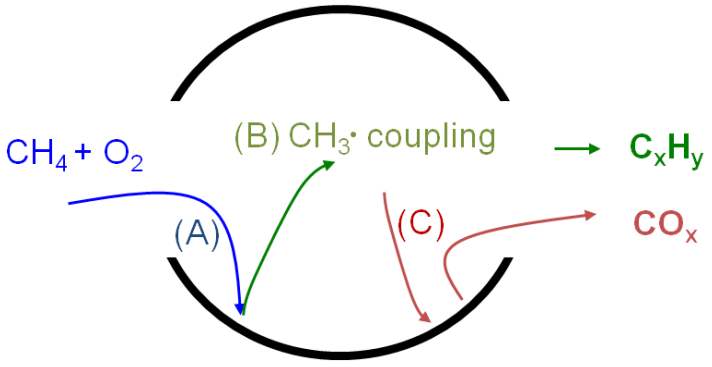

Figure 1.1.: Schematic reaction mechanism of the OCM reaction with (A) generation of methyl radicals on the catalyst surface, (B) coupling of methyl radicals, (C) undesired overoxidation to CO and CO_2 on the catalyst surface

Many different materials such as MgO, Li@MgO or W-Mn/SiO_2 have been proposed as active and selective OCM catalyst.[3] However, the exact reaction mechanism of the OCM remains subject of controversial discussions. Lunsford et al. suggested that the formation of methyl radicals (A) as well as the overoxidation products CO_x (C) are formed on the catalyst surface, while the

combination of methyl radicals to the desired C_2-products (B) takes place in the gas phase (see Figure 1.1).[4] However, the interplay of gas phase volume and surface area on the C_2-selectivity has not been reported so far.

The contribution of gas phase and surface reaction can be analysized by controlling the ratio of gas phase and surface area. This ratio can be tuned by introducing controlled porosity into the catalyst. The influence on the C_2-selectivity can be investigated by the preparation of a series of OCM catalyst with different pore sizes and subsequent OCM testing. The controlled synthesis and variation of a sufficiently wide range of pore sizes in OCM catalysts has not been reported yet.

Many templated mesoporous metal oxides can be synthesized for example by replication of the mesoporous silica ("SBA") via nanocasting. However, direct soft-templating approaches for the synthesis of MgO, ZnO, Co_3O_4 powders and films failed so far due to the lack of appropriate oxide precursors. The reasons for failure are intrinsically tied to the chemical and physical properties of known precursors as well as to mechanisms of mesophase formation and template removal.

Typically, oxides were synthesized from (I) alkoxides or partially alkoxylated metal chlorides, (II) preformed colloidal nanoparticles and (III) thermally decomposable metal compounds.[5] Route I based on hydrolysis and condensation of alkoxy groups fails for precursors with high hydrolysis and condensation rates, because rapid condensation results in undesired precipitation prior to mesophase assembly. Route II requires high-quality building blocks such as a redispersible nanocrystalline colloid with a small particle diameter ($d < \sim 5$ nm) and a narrow size distribution. However, for many metal oxides, such nanoparticle syntheses remain challenging. Approach III is limited to metal precursors that do not show excessive crystallization upon drying; otherwise, the ordered mesostructure cannot be formed. Moreover, oxide formation must occur at temperatures significantly below the typical temperatures of template combustion (~300 °C); otherwise, pores collapse because of premature template removal. Other constraining factors are the limited solubility of many precursor compounds, melting during calcination, and rapid crystallite growth of the metal oxide before template removal. Additionally, a general limitation of all methods described here is that they do not provide access to the soft-templated synthesis of mesoporous metal carbonates.

In this thesis a new synthesis concept is presented which is based on a novel type of material precursor. This new type of precursor allows the synthesis of MgO, ZnO and Co_3O_4 with micelle templated mesopores for the first time. Moreover, this is the first synthesis strategy yielding also metal carbonate films with templated mesoporosity.

The developed synthesis concept can be transferred to yield powders with controlled porosity. The obtained mesoporous MgO based powders are tested in OCM reaction and analysed concerning the influence of the pore size on the C_2-selectivity. The results are compared to the additional catalyst system W/Mn-SiO_2. To obtain W/Mn-SiO_2 with controlled porosity, a synthesis procedure for the introduction of tungsten and manganese as OCM active elements in the hydrothermal synthesis of SBA silica was developed. The performance of the resulting catalysts with a broad range of pore diameters is tested in the OCM reaction. The C_2-selectivity is analysed in dependence of the pore size and allows a better mechanistic understanding of the OCM reaction.

Parts of the results of this thesis have been submitted for publication[BE1,BE2] and in a patent application[BE3].

2. State of the Art

This chapter explains some basics of metal oxide synthesis and their application in catalysis. At first, the importance of metal oxides for various catalysis approaches is presented in section 2.1. Section 2.2 focuses in particular on the oxidative coupling of methane (OCM) and describes the proposed reaction mechanism as well as the synthesis and catalytic results of typical OCM catalysts. Moreover, the synthesis of metal oxides with templated mesoporosity is explained in section 2.3. Finally, the aims of this thesis are deduced in section 2.4.

2.1. Metal Oxides as Catalysts

A catalyst is a material that converts reactants into products, through a series of elementary steps, in which the catalyst participates while being regenerated to its original form at the end of each cycle during its lifetime.[6] A catalyst changes the kinetics of the reaction, but does not change the thermodynamics. The catalyst offers an alternative pathway for the rearrangement of chemical bonds. Therefore, a catalyst can accelerate the reaction rate or facilitate a chemical reaction that would not occur. Furthermore, a catalyst can increase the selectivity towards a desired product, when a chemical reaction yields a variety of reaction products. Approximately 90% of the products of the chemical industry are synthesized with the help of catalytic processes. Hence, catalysis is of major importance for the chemical industry.

Most of the applied catalysis in industry is heterogeneous catalysis. In heterogeneous catalysis the catalyst is typically present in solid state and the reactants are in liquid or gas phase. The majority of heterogeneous catalysts are based on metal oxides as catalyst or catalyst support. One example for the importance of metal oxides in heterogeneous catalysis is the synthesis of methanol. Methanol as a base chemical is produced by reacting carbon monoxide with hydrogen over a catalyst based on a mixture of copper and zinc oxide on aluminium oxide support.[7]

However, applications in catalysis require a high surface area in order to maximize the number of accessible surface sites. A material's specific surface area can be increased by introduction of small pores in the catalyst. Unfortunately, diffusion limitations of catalytic reactants in porous systems prohibit too small pores. Therefore, mesoporous materials provide often the best compromise between high surface area and fast mass transport.

An example of a catalyst system with optimized mass transport is the car exhaust catalytic converter.[8,9] The main body is a ceramic monolith with macroscopic channels. The channel's internal surface is impregnated by a washcoat typically of Al_2O_3. This washcoat is the carrier of highly dispersed catalytic active platinum, palladium or rhodium nanoparticles. The macroscopic channels distribute the exhaust gas to ensure the external mass transport over the whole monolith. The internal mass transport to the catalytically active metals by diffusion is mainly determined by the mesostructure of the Al_2O_3 washcoat. Therefore, controlling the pore size of the alumina support can enhance the catalytic performance of car exhaust catalysts.

Another example for the increase of catalytic activity by introduction of controlled porosity are electrocatalysts. Co_3O_4 is a promising electrocatalyst for the oxygen evolution reaction (OER).[1] The OER is the challenging half cell reaction of electro chemical water splitting, that could facilitate the effective conversion of electrical into chemical energy in the form of H_2. The catalytic performance of Co_3O_4 could be improved by introducing mesoporosity to increase the electrochemical active surface. However, a synthesis of Co_3O_4-films with controlled pore sizes has not been reported so far.

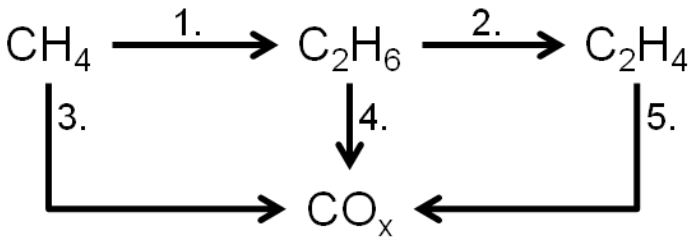

Figure 2.1.: Reaction scheme of OCM: 1. coupling of methane to ethane; 2. dehydrogenation of ethane to ethylene; 3. oxidation of methane to CO_x; 4. oxidation of ethane to CO_x; 5. oxidation of ehtylene to CO_x; adapted from Lunsford[10]

In addition, not only the surface area but also the accessible gas volume can influence the performance of a catalyst. One example for the influence of gas phase reaction on the catalyst performance is the oxidative coupling of methane (OCM). The next section explains the reaction mechanism as well as the synthesis and catalytic performance of typical employed catalyst.

2.2. Oxidative Coupling of Methane

Currently, industrial production of olefins is based on fossil oil. The reserves of natural gas which are estimated to exceed those of fossil oil and the increasing production of biogas are considered as preferable raw material for olefines.[3] Hence, a strong economic interest exists in developing alternative processes to convert natural or biogas into higher-valued products. The oxidative coupling of methane (OCM) is one option to overcome the dependency on crude oil of chemical industry. The OCM is a catalyst assisted coupling of CH_4 to higher alkanes and alkenes mainly yielding the C_2-products ethane and ethylene.

Figure 2.1 presents the suggested reaction sequence and products involved in OCM.[10] In the first step (1.) methane is oxidized and coupled to ethane. Oxygen O_2 is typically employed as oxidizing agent, but also N_2O[11] was employed successfully in OCM. In the second step of the reaction sequence (Figure 2.1 2.) ethane is oxidative dehydrogenated to yield ethylene.[10,4] The reaction steps 1 and 2 (combination of step 1. and 2. $\Delta G_R(800\ °C)$ = -153 kJ/mol) are exergonic processes.[12] Therefore, the formation of C_2-products by coupling of methane should occur readily. However, the thermodynamically favoured reaction is the overoxidation of CH_4 (Figure 2.1 3.) to CO_x (to CO: $\Delta G_R(800\ °C)$ = -611 kJ/mol; to CO_2 $\Delta G_R(800\ °C)$ = -801 kJ/mol).[13] Moreover, the C_2-products, ethylene and ethane, readily react with oxygen to CO_x and can be activated for oxidation more easily (Figure 2.1 4. and 5.) compared to methane.[10] The formation of CO_2 from oxidation of methane as well as ethan and ethylene is undesirable, since it represents a decreased yield of hydrocarbons.

Since the pioneering works of Keller and Bhasin[23] as well as Hinsen and Baerns[24] a large number of different catalytic materials have been investigated. Figure 2.2 compares the performance of selected catalytic materials in OCM reaction.[3] Many different oxides such as Li doped MgO,[4] La doped MgO,[16] BaO/Ga_2O_3, Rb_2WO_4/SiO_2,[17] 95mol%BaF_2/Y_2O_3,[15] $Bi_{1.5}Y_{0.3}Sm_{0.2}O_{3-d}$,[18] Na_2WO_4/SiO_2,[17] Mn-Na_2WO_4/SiO_2[12] have been proposed as active and selective OCM catalysts. However, the catalysts show high selectivity only at low conversion. High methane conversion results in low C_2-selectivity. Industrial application demands high selectivity accompanied by high conversion to be economically interesting. This has not been achieved with any catalyst system, yet.

In addition, the reaction mechanism of OCM remains subject of controversial discussions. Lunsford et al. extensively studied the mechanism and catalytic performance of OCM on Li@MgO (Li doped MgO) catalyst. They prepared Li@MgO by wet impregnation of MgO with Li_2CO_3 to yield lithium contents of 0.2 - 26%wt. The catalytic testing was performed to evaluate the

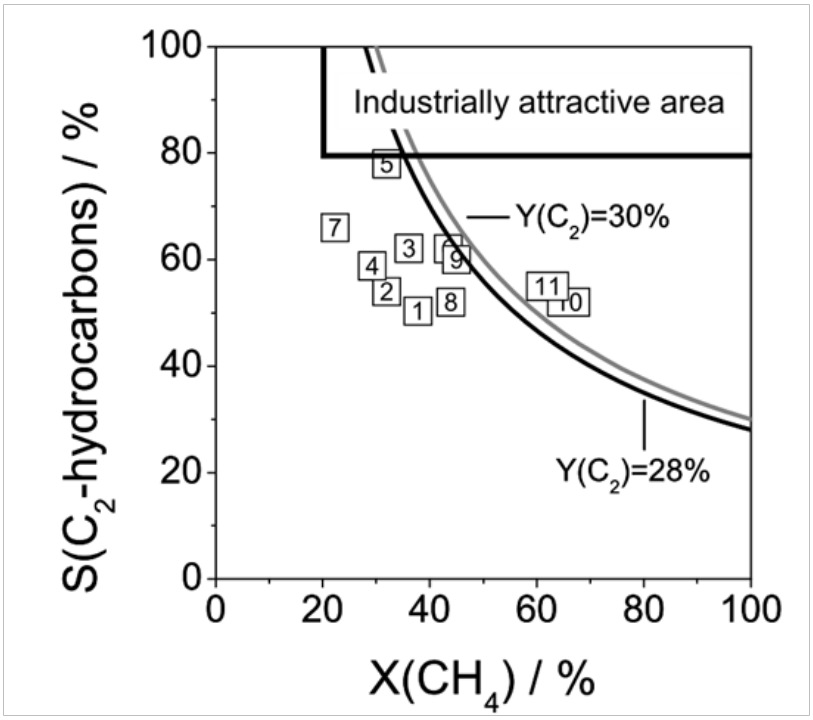

Figure 2.2.: OCM performance over selected catalytic materials: 1 - Li/MgO,[4] 2 - 30%BaO/Ga_2O_3,[14] 3 - 95mol%BaF_2/Y_2O_3,[15] 4 - La/MgO,[16] 5- Rb_2WO_4/SiO_2,[17] 6 - $Bi_{1.5}Y_{0.3}Sm_{0.2}O_{3-d}$,[18] 7 - La_2O_3-CeO_2,[19] 8 - Na_2WO_4/SiO_2,[17] 9 - 10%Y_2O_3-89%ZrO_2-1%TiO_2 membrane with $Li_2O/MgO/ZrO_2$,[20] 10 - Ba(1-0.5x)TiO_3SnCl_2 (0.05x) (x is 1 mol),[21] 11 - $Bi_{1.5}Y_{0.3}Sm_{0.2}O_{3-d}$;[22] image and references taken from Kondratenko et al.[3]

dependence of OCM on temperature and lithium content. The pure MgO as well as Li@MgO are both active in OCM at temperatures $>$ 600 °C. The pure MgO yielded higher methane conversion compared to Li@MgO. However, the lithium doped catalyst has shown significantly higher C_2-selectivity.

They performed electron paramagnetic resonance spectroscopy (EPR) to indentify the active centre in Li@MgO.[4] They concluded from the detected EPR signal a $[Li^+O^-]$ species to be the centre of the methane activation. In the first step of the proposed mechanism (so called Lunsford mechanism), the $[Li^+O^-]$ species abstract a hydrogen atom from methane and the resulting methyl radicals recombine in the gas phase to form ethane which further reacts with surface O^- ions to produce ethylene. The active site is regenerated by oxidation with O_2.

After proposing the active centre, the Li@MgO catalyst was tested on long term stability for 40 h time-on-stream at 700 °C. The catalyst prepared with 7%wt lithium content had shown a strong initial loss in the first 10 h on stream, but stabilises subsequent at approximately 40% methane conversion with a C_2-selectivity of 45%.

However, Arndt et al.[25] published 2010 an comprehensive study on the OCM performance of MgO and Li@MgO to validate the results of the Lunsford group. In addition to the wet-impregnation method of Lunsford, the group prepared magnesium oxide based OCM catalysts by thermal decomposition of a single source precursor of the type $LiOR{\cdot}[CH_3MgOR]_3$ (R=alkylgroup), by a sol-gel route employing $Mg(NO_3)_2$, ammonia and LiOH as well as by mixed milling of MgO with $LiNO_3$. The lithium content was varied in each synthesis route. The OCM performances of the catalysts were compared according to the preparation method, lithium content and stability over time-on-stream.

Arndt et al. described the catalysts as active in OCM. However, the overall performance is rather low disregarding the preparation procedure or the Li-loading.

After an initial loss of methane conversion in the first 3 - 4 h the C_2-selectivity had reached

values of approximately 30 - 35% at a methane conversion of $< 10\%$ after 5 h time-on-stream at 750 °C. The intensity of the initial decrease in OCM activity was found to be mostly influenced by the preparation method, although it is observed for all catalyst. In addition, Arndt et al. reported a significant loss of lithium from the Li@MgO during the first hour time-on-stream. They suggested that the loss of lithium is related to the initial activity drop. Arndt et al., therefore, questioned the assumption of Lunsford[4] that $[Li^+O^-]$ is the active centre of the methane activation. No correlation between the OCM activity and the lithium content (probed in dependence of time-on-stream) could be found. The catalyst prepared without lithium had showen the highest methane conversion in comparison with Li@MgO, although the C_2-selectivity is significantly lower. Hence, lithium is still considered to be included in the methane activation and coupling. However, Arndt et al. observed the trend of decreasing methane conversion with increasing lithium content $> 0.5\%$wt. A similar trend related the C_2-selectivity was not reported. Thus, the role of lithium in Li@MgO OCM catalyst is not finally understood and is still subject of controversial discussion.

Moreover, Arndt et al. tested the stability of the Li@MgO at 750 °C for 40 h time-on stream. In contrast to Lunsford[4] et al., they reported proceeding decrease in activity over time-on-stream. They considered to be originated in the significant loss of surface area due to strong crystallite growth. Thus, MgO and Li@MgO are no longer proposed as potential candidates for industrial application in OCM. However, magnesium oxide based catalysts are still model catalysts for mechanistic studies of the OCM reaction due to its simple composition and broad knowledge base collected over the years on this catalyst system.

An alternative to Li@MgO is the OCM catalyst W-Mn/SiO_2 which is subject of a growing number of investigations since its first publication in 1992.[26] First mentioned by Lin et al.[26] as W-Mn/SiO_2 the same catalyst system prepared by different methods is often referred to as Mn-$Na_2WO_4SiO_2$.[12] This catalyst is reported to have a remarkable catalytic stability at the high temperatures which are required for the oxidative coupling of methane.[12] Moreover, the catalytic performance with C_2-selectivities of 70 - 80% at methane conversions of 20 - 30% is interesting for industrial application.

The various synthesis methods to synthesize W-Mn/SiO_2 are reported in literature. Lin et al. prepared this type of catalyst first by wet impregnation[27,28] of silica particles with an aqueous solution of $Mn(NO_3)_2$ and $Na_2WO_4{\cdot}2H_2O$,[26,27] but also compared the OCM performance to catalysts synthesized by physical mixing,[27] mixed slurry[28] and sol-gel.[28] However, in the majority of subsequent publications, W-Mn/SiO_2 catalysts were prepared via an incipient wetness impregnation method due to the simple preparation procedure and the high catalytic performance. A variation of the composition was studied in detail by Ji et al.[29] (Na: 0.4 - 2.3 wt%, W: 2.2 - 8.9 wt%, Mn: 0.5 - 3.0 wt%) without major changes of the resulting catalytic activity. The typically employed catalyst yielded mostly a composition of 5 wt% Na_2WO_4 and 2 wt% Mn corresponding to SiO_2.

The characterisation of the crystalline composition after typical calcination temperature between 800 °C and 900 °C by XRD revealed the presence of SiO_2 in the various modifications tetragonal α-cristobalite, α-tridymite and cubic quartz as well as in amorphous form.[12,30,11,28] Tungsten and manganese were found in the crystallite composition Mn_2O_3, Na_2WO_4 and WO_3. It was reported that for the impregnation method, the components Mn, Na and W were mainly found on the surface, while for the catalysts prepared by mixed slurry and sol-gel the elements were equally distributed between bulk and surface.[12,26,27,30]

Li et al. compared the catalytic performance of W-Mn/SiO_2 OCM catalysts in dependence of the preparation method for 500 h at 820 °C. A C_2-selectivity of 69% had been reached for catalysts prepared by wet impregnation at a methane conversion of 30% as well as for catalysts prepared by mixed slurry 27% conversion.[28] The catalysts prepared by a sol-gel route have shown a modest activity with 22% methane conversion for 69% C_2-selectivity. This, in comparison to Li@MgO, high performance was confirmed by Arndt et al. yielding 78% C_2-selectivity at 4% methane conversion (750 °C) by their catalyst prepared by wet impregnation. Moreover, both

groups reported outstanding long term stability in OCM performance.

In contrast to the catalytic stability, some morphological and compositional changes were reported. Lin et al. observed the transformation of amorphous SiO_2 ultimatly transforms into cristobalite phase[28] during catalysis for 50 h time-on-stream at 820 °C. However, a long term stability test up to 500 h causes further phase transition of α-cristobalite into quartz and α-tridymite without significant changes in the catalytic performance. This indicates that α-cristobalit is not always indispensable for high active and selective OCM catalysts. In addition, Simon et al.[30] reported the slow formation of $MnWO_4$ from Na_2WO_4 and $Mn(NO_3)_2$ as well as partial melting of the catalyst. They assumed that sodium ions form eutectic melts with silica and tungsten oxide. They concluded that this melting could be the reason of morphological restructuring of the catalyst during OCM. Despite all morphological and compositional changes of the catalyst, large amounts of identified surface species and different preparation methods, the catalytic performance was never significantly affected. Therefore, the active center as well as the reaction mechanisms of W-Mn/SiO_2 OCM catalysts are still subject of controversial discussions.

Moreover, the performance of an OCM catalyst is assumed not only to be determined by the nature and the number of active centres. Considering the Lunsford mechanism,[4] the formation of methyl radicals as well as the overoxidation products CO_x occur on the catalyst surface. The combination of methyl radicals to the desired C_2-products, however, takes place in the gas phase. Hence, the accessible gas phase volume as well as the surface of the catalyst pores should affect the resulting selectivity towards ethane and ethylene.

However, the influence of the gas volume to catalyst surface area ratio on C_2-selectivity has not been reported so far. This contribution to the OCM performance could be investigated by synthesizing a model catalyst with controlled gas volume to surface area ratio by introducing a controlled porosity into the material and testing in OCM reaction. The lack of a synthesis procedure to obtain materials with a tailored pore system prevented this investigation up to now. The next sections explain in detail procedures for the synthesis of metal oxides with controlled pore size.

2.3. Synthesis of Metal Oxides with Templated Mesoporosity

In comparison to bulk materials without porosity, porous materials exhibit a large internal surface area. When the activity of a material in an application correlates with its surface area, the performance of the material will be increased by introducing porosity. Therefore, absorbent materials,[31,32] gas sensors,[33] electrodes,[34,35] and catalysts[9,36] are often designed to have a high porosity with large surface area.

IUPAC classifies porous materials depending on the pore diameter into microporous (< 2 nm), mesoporous (2 - 50 nm) and macroporous (> 50 nm) materials.[37] Although, numerous preparation methods exist yielding materials with micro-, meso- and macropores, in this thesis only syntheses for metal oxides with controlled mesoporosity are addressed.

So-called "templating" is one of the most versatile methods to control the nanostructure of a metal oxide during wet-chemical synthesis.[38,39] Templating of metal oxides requires material precursors and preformed nanostructures, so called templates. These structure directing agents are molecular or supramolecular units possesses or forming a predefined nanostructure. Employing structure directing agents in the synthesis of metal oxides the inverse shape of the template can be introduced into the final material by removal of the template. Material precursors are chemicals which can be transformed into the desired material. This transformation as well as the removal of the template is typically accomplished by a thermal treatment, a so called calcination. The calcination temperature and time is of critical importance for a successful synthesis especially for the synthesis of templated mesoporous metal oxides. The importance of the calcination temperature for the synthesis of metal oxide catalysts with templated pore structure is exemplarily explained for the electrocatalyst IrO_2.

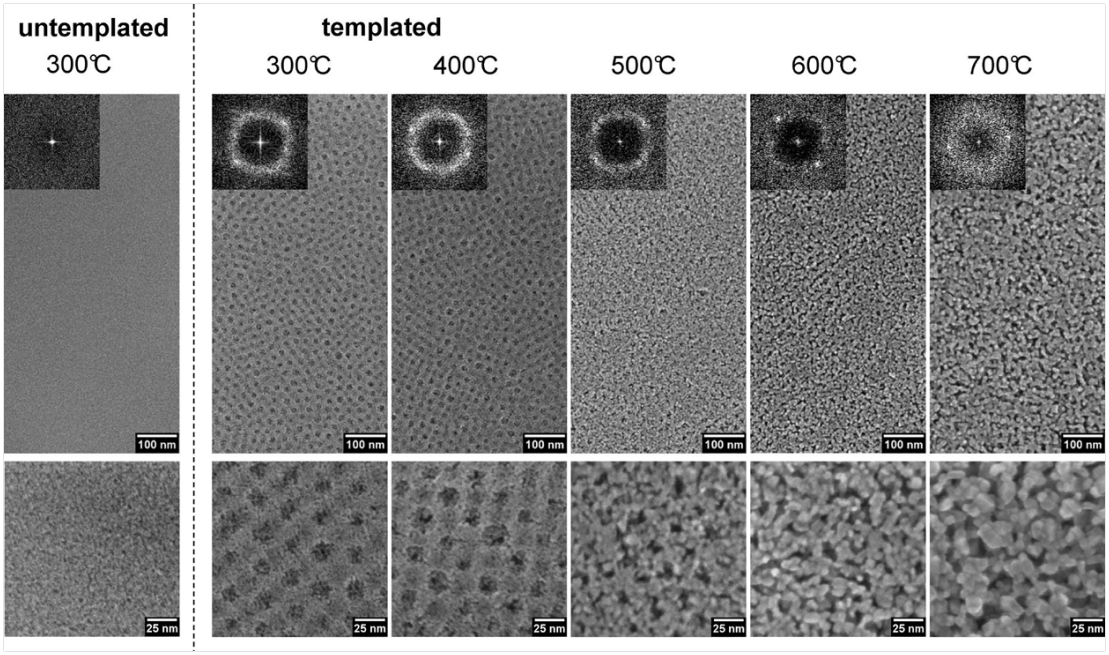

Figure 2.3.: SEM images of mesoporous ("templated") iridium oxide films templated with PEO_{213}-PB_{184}-PEO_{213} calcined at 300, 400, 500, 600, and 700 °C (from left to right) including the respective FFT of the image as inset. Corresponding SEM images at higher magnification are shown in the bottom row. The iridium oxide film prepared without pore template and calcined at 300 °C ("untemplated") is shown for comparison in the left column; taken from Ortel et al.[40]

Ortel et al. demonstrated the influence of the calcination temperature on the template removal and the sintering behaviour of IrO_2 crystallites in templated mesoporous IrO_2 films. The group employed iridium acetate as material precursor and micelles of triblock-copolymer as template. After film deposition of the conjoint precursor and template, the samples were calcined at temperatures between 25 °C and 800 °C.

Figure 2.3 presents the SEM study of IrO_2 films calcined at temperatures between 300 °C and 700 °C. At temperatures between 250 °C and 400 °C the template is removed and a mesoporous film is obtained. However, at this temperature the pore walls are still X-ray amorphous. In contrast, at $T > 500$ °C the pore walls consist of IrO_2 crystallites. While at 500 °C the mesoporous structure can still be observed, at $T > 600$ °C the crystallite size is drastically increased due to sintering. The sintering is accompanied by a reorganization of the templated mesoporous structure into a so-called "gridlike" structure, which has been first observed by Grosso et al. for templated TiO_2.[41] Hence, too high temperatures can result in the loss of the templated pore structure.

Ortel et al. concluded the optimal calcination temperature to be 450 °C. At this temperature the template is fully removed and the material precursor is transformed into nanocrystalline IrO_2 pore walls with retained mesopore structure. Thus, the optimization of the calcination temperature is crucial in the synthesis of templated metal oxides to remove the template completely and retain the pore structure with nanocrystalline walls.

The next sections present a classification and give examples of mesopore templates (see section 2.3.1) and material precursors (see section 2.3.2). Moreover, approaches for the synthesis of metal oxide films (see section 2.3.3) and powders (see section 2.3.4) with controlled mesoporosity are explained.

2.3.1. Pore Templates

Template-based syntheses have been reported for metal oxides with mesopores,[42,5] macropores,[43–46] and hierarchical porosity.[45–47] Depending on the nature of the employed template,

so-called hard- and soft-templating can be distinguished.

Hard templates are typically preformed scaffolds formed of porous silica[38] (e.g. MCM-41,[48] SBA-15,[49] KIT-6[50]), carbons[38,51,52] (e.g. CMK-3[53]) or colloidal crystal[54] (e.g. poly(methyl methacrylate),[55] polystyrene[45]). Hard templating is commonly employed for the synthesis of macroporous (e.g. ZnO,[43,44] Co_3O_4[45,46]) and mesoporous (ZnO,[42] Co_3O_4[36,56]) oxides in the form of powders. A detailed description on the synthesis of hard templates and the hard-templated metal oxides is given in section 2.3.4. However, soft-templating is by far the most common synthesis approach for mesoporous oxides.[38,5,39]

Soft-templates are typically aggregates of surfactants, so called micelles. Surfactants are amphiphilic molecules composed of hydrophilic and hydrophobic parts. The surfactants are usually classified into ionic and non-ionic.

Ionic tensides are typically composed of hydrophobic alkyl chains and hydrophilic functional groups, for example carboxylate or ammonium groups. This type of surfactants forms relatively small templating micelles yielding mesopores with a diameter < 4 nm for example in silica materials MCM-41 which is templated with cetyltrimethylammonium bromid (CTAB).[48]

Oxides with larger mesopores can be obtained by employing non-ionic templates in the synthesis. Typically block-copolymers are used. They consist of two or more covalently bonded hydrophilic and hydrophobic homopolymer blocks. Many different hydrophilic homopolymers exist, for example glucoside and polyethylene oxide. However, polyethylene is typically employed in non-ionic polymer templates.

In contrast to the hydrophilic blocks, numerous hydrophobic blocks are employed in amphiphilic polymer templates. Examples for hydrophobic blocks in block-copolymer templates are polypropyleneoxide (PPO),[57–60] polyisoprene (PI),[61,62] polyisobutylen (PIB),[63–65] polybutadiene (PB),[66,67] polystyrene (PS)[68–72] or polymethylacrylat (PMA).[73] Simple alkyl chains are also employed as hydrophobic part, for example the available Brij diblock-copolymers for example Brij56 with the structure ($C_{16}H_{33}$-PEO_{10}-OH).[74,75]

In addition, the commercially available triblock-copolymers of the Pluronic family with the structure PEO-PPO-PEO are the mostly employed templates in literature.[57–60] The typically used Pluronic templates are F127 (PEO_{106}-PPO_{70}-PEO_{106}), F108 (PEO_{130}-PPO_{50}-PEO_{133}) and P123 (PEO_{20}-PPO_{70}-PEO_{20}). Unfortunately, Pluronic polymers are commercially available only with relatively short hydrophobic PPO blocks resulting in metal oxides with a maximum mesopore diameter of 11 nm.[49,76]

In addition to the size of the polymer blocks, the hydrophilic-hydrophobic contrast between the constituent blocks of the amphiphilic block copolymer is of crucial importance, since it represents the driving force for micelle formation and directly influences the micelle shapes.[77] Pluronic F127, for example, does not form micelles even at a concentration of 1.2%wt in solution due to the low amphiphilic contrast between the PPO and PEO blocks.[66]

In contrast, due to the stronger amphiphilic contrast in triblock-copolymers composed of polybutadiene (PB) middle and PEO end blocks form micelles already at 0.12%wt in solution. Excellent self-assembly behaviour, very low critical micelle concentration (cmc), slow exchange rates between the solvated polymer molecules and micelles, and high micelle stability have been reported for PB-PEO diblock[78–80] and PEO-PB-PEO triblock[66] copolymers. Moreover, Ortel et al. demonstrated by employing PEO-PB-PEO polymer templates the individual control of wall thickness and pore size in mesoporous titania films.[66]

The pore size in a material cannot only be increased by employing templates with higher molecular weight, but also by enlargement of the micelles with a so-called swelling agent.[49,57] Swelling agents are typically aromatic molecules, for example benzene or mesitylene.[81] The hydrophobic agent is introduced into the hydrophobic core of a micelle and, therefore, leads to an increase of its size.[49,57] Zhao et al. demonstrate the increase of pore diameter in mesoporous silica powders up to $\sim$30 nm by employing Pluronic P123 and trimethylbenzene as swelling agent.

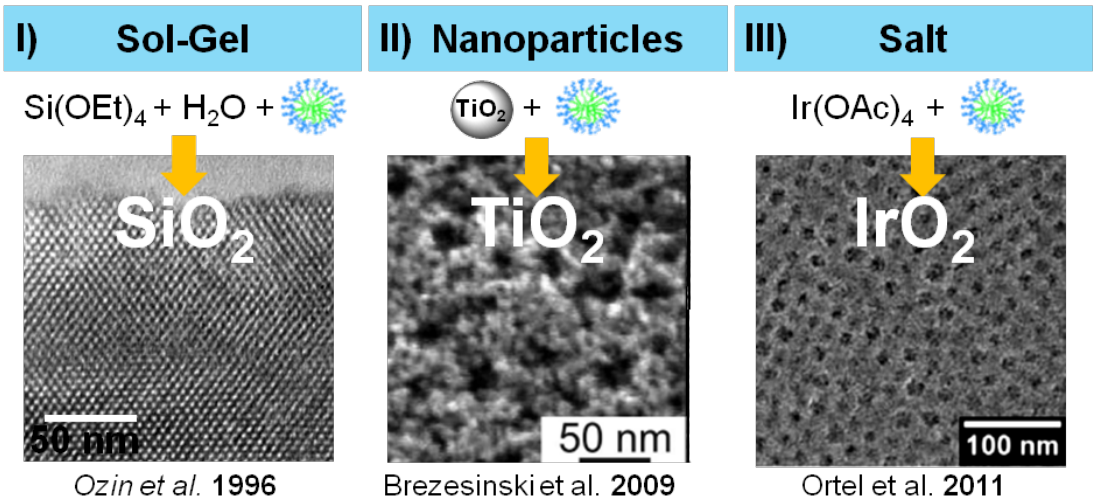

Figure 2.4.: Examples of mesoporus films synthesized by employing different precursor types; SEM of a) a SiO_2 film synthesized by CTAB and $Si(OEt)_4$ as sol-gel precursor,[82] b) TiO_2 film synthesized with preformed TiO_2 nanocrystals and PIB_{89}-PEO_{79} template[83] and c) IrO_2 film synthesized with PEO_{213}-PB_{184}-PEO_{213} and $Ir(OAc)_4$ as salt-type metal oxide precursor[40]

2.3.2. Material Precursors

Material precursors are chemicals that transform into a desired material by chemical or thermal treatment. During the synthesis of metal oxides with templated mesoporosity, the material precursor is structured by the template. The final mesoporous material is obtained after removal of the template transformation of the precursor into the desired material.

For the synthesis of templated metal oxides, 3 types of material precursor should be distinguished: (I) sol-gel precursor, (II) nanoparticles and (III) salts.[5] Figure 2.4 presents exemplarily SEM images of different materials prepared with these material precursors.

Typical sol-gel precursors (I) comprise hydrolysis sensitive alkoxides or partially alkoxylated metal chlorides, for example $Si(OEt)_4$,[49,82,84] $Al(O^iPr)_3$,[85,86] $(MeZnOBu)_4$,[87] $TiCl_4$,[88–90,66] $ZrCl_4$,[88,91] $NbCl_5$.[92,88] The principle reaction steps of sol-gel precursors are similar but differ in the reaction kinetics depending on the chemical nature of the metal ion.[54]

The typical reaction pathway can be summarized as follows:[93] In the first reaction step the sol-gel precursor undergoes hydrolysis reaction. The resulting metal hydroxides start to condensate and form M-O-M bonds. The linkage of additional hydroxyl groups occurs as a polycondensation reaction resulting at first in the formation of small sol particles. Progressing polycondensation accelerated by the increase of the concentration or the temperature leads to an isotropic metal oxide network, the so called gel.

The sol-gel approach in the synthesis of mesoporous metal oxides often results in unstructured and amorphous pore walls, for example SiO_2[49,82,84] or TiO_2[88–90,66] One example for the synthesis of soft-templated silica thin films employing the sol-gel precursor tetraethyl orthosilicate and the ionic template CTAB is presented in Figure 2.4a. Sol-gel precursors are the most applied precursor type in the synthesis of templated metal oxides.[5] However, The sol-gel approach fails in the synthesis of some micelle structured oxides. For example, ZnO, Co_xO_y and MgO have not been reported as micelle templated films so far. The reason is originated in the reactivity of the metal alkoxides. The alkoxides of Zn, Mg and Co show a high hydrolysis and condensation rate resulting in undesired precipitation prior to mesophase assembly. Hence, no templated mesoporous oxide of Zn, Co or Mg can be obtained after calcination with sol-gel precursors.

The nanoparticle approach[94,83,5] (II) (also reported as building-blocks[83,5]) employs preformed nanocrystals or nanoclusters as material precursor. The nanocrystals are coemployed with a template and they have to assemble into a structured mesophase during synthesis. After the

formation of the templated mesophase, the nanoparticles are transformed into a compact material by sintering. The nanoparticles need to fulfil some requirements to be suitable for templating approaches. The nanoparticle need to have a small particle diameter (< 5 nm) and narrow size distribution for the optimal enclosure of the template. Further, they have to be redispersible in the presence of the template in solvents typically applied for the mesophase formation. Figure 2.4b) presents an SEM image of mesoporous titania reported by Brezesinski et al. prepared with preformed TiO_2 nanoparticles and PIB_{89}-PEO_{79} template (KLE). The pore walls appear to be significantly more structured and crystalline compared to TiO_2-films obtained by the sol-gel approach.[88–90,66] The nanoparticles templating approach has been successfully applied for the synthesis of different micelle templated metal oxides, for example TiO_2,[83] Al_2O_3,[95] Mn_3O_4,[96] $MnFe_2O_4$, $In_xSn_yO_z$ (ITO).[96,97] However, soft-templating of ZnO, Co_3O_4 and MgO nanoparticles have not been reported, yet. The reason for this could be originated in the lack of suitable synthesis procedures yielding redispersible, monodisperse nanoparticles with diameters < 5 nm.

The salt approach (III) employs thermally decomposable metal salts (e.g. acetates, nitrates, citrates, chlorides, ...). These salts enclose the template unreacted and decompose into the final oxide during calcination. Figure 2.4c) presents an SEM image of mesoporous IrO_2 yielded from iridium acetate salt.[40] This approach is very straight forward, because no preceding synthesis or reaction is necessary and the procedures are rather simple. However, this approach often fails due to reasons intrinsically tied to the mechanisms of mesophase formation and template removal. For example halides, nitrates and acetates often show the tendency of excessive crystallization during drying which prevents the formation of the required structured mesophase. Other constraining factors are limited solubility of many precursor compounds (oxalate, lactate, acetylacetonate, carbonate or citrate), melting during calcination or rapid crystallite growth of the metal oxide already before template removal.

In summary, the presented oxide precursor types (I) sol-gel, (II) building block and (III) salts can yield numerous of soft-templated oxide materials.[5] However, soft-templated MgO, ZnO and Co_3O_4 cannot be synthesized with these approaches. The reasons are intrinsically tied to the chemical and physical properties of known precursors as well as to mechanisms of mesophase formation and template removal. The ideal oxide precursor should be well soluble in typically applied solvents (water, ethanol, tetrahydrofuran), but should not crystallize subsequently to deposition. Furthermore, the precursor should not precipitate due to fast sol-gel chemistry and should allow a control over rapid crystallite growth of the oxide.

2.3.3. Synthesis Approach for Metal Oxides Films

The most common approach to synthesize soft-templated metal oxide films involves "evaporation induced self-assembly" (EISA) of micelles.[77,98,39] EISA-based syntheses offer three major advantages: (i) porous materials are accessible in form of films, fibers or powders; (ii) the pore size and shape can be controlled by the physical properties and the concentration of the template; (iii) the synthesis protocols are simple and reproducible.[77,98,5]

The principle synthesis steps of EISA-based film synthesis are schematically illustrated in Figure 2.5. The procedure usually starts with the preparation of a coating solution by dissolving an amphiphilic block-copolymer and oxide precursor in volatile solvent (e.g. ethanol, water, tetrahydrofuran, ...) or solvent mixture. Thereafter, the homogeneous coating solution is deposited on the surface of substrates like silicon wafers, stainless steel plates or glass. Many different solution-based deposition methods, e.g. spin coating or drop casting, can be applied for film deposition. However, dip-coating is the most common deposition method in EISA synthesis. Applying dip coating, the substrate is introduced into the coating solution and drawn out with controlled withdrawal rate. Initiated by the evaporation of the solvent from the deposited film, the concentration of the oxide precursor as well as the amphiphilic template is progressively increased. The increase of the surfactant concentration drives a self-assembly of surfactant micelles and the material pre-

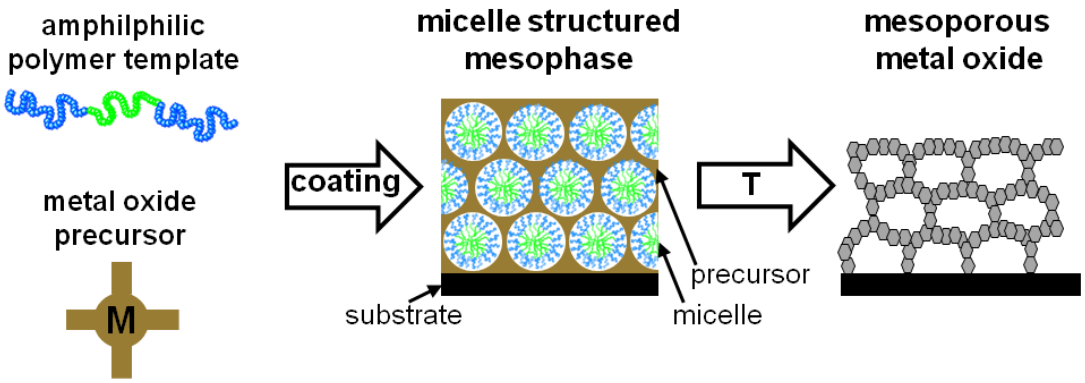

Figure 2.5.: Schematic of the preparation steps of soft-templated metal oxide films: coating solution (a) contains an amphiphilic polymer template and a material precursor, after coating a micelle structured mesophase (b) is obtained, subsequent calcination yields the mesoporous metal oxide (c)

cursor into a liquid-crystalline mesophase.[77]

The mechanism of the mesophase formation is depending on the hydrophilic-hydrophobic contrast of the template. This amphiphilic contrast mainly determines the concentration at which micelles are formed in solution, the critical micelle concentration (cmc).

Templates with a relatively high cmc, for example F127 (∼20%wt at 20 °C[99]) or P123 (∼20%wt at 20 °C[99]), are initially present in the coating solution in a non-micellar isotropic phase at typical concentrations of 3 - 5%wt (20 °C). The formation of templating micelles occurs first during the evaporation of the solvent after film deposition. Therefore, the drying speed is essential for a controlled mesophase formation. The drying speed can be controlled by adjusting the temperature and the humidity[100] as well as the withdrawal rate.[101] Optimized atmospheric conditions and withdrawal rate[101] result in highly ordered pore system after calcination.

In contrast to surfactants with a high cmc, amphiphilic templates with low cmc, for example PEO-PB-PEO[66] or PS-PEO,[102] form micelles already in the coating solution. The evaporation of the solvent after film deposition results in the self-assembly of the preformed micelles on the substrate. Therefore, the mechanism of mesophase formation using polymer template with low cmc is referred to as evaporation induced micelle assembly (EIMA).[102] The EIMA process is very robust; during film formation, the synergetic coupling between surfactant self-assembly and precursors is not required. Ortel et al.[66] demonstrated by employing templates with high hydrophilic-hydrophobic contrast that the pore wall thickness of the resulting films after calcination can be controlled by the initial template concentration. Hence, employing templates with low cmc in different molar weights allows the individual control of wall thickness and pore diameter in the desired material after calcination.[66]

The calcination temperature after film deposition and drying is crucial to obtain nanocrystalline walls and a preserved pore system (see section 2.3). Templates decompose typically at temperatures $>$ 250 °C.[103,104] The calcination temperature for precursor decomposition and the generation of nanocrystallinity vary depending on the nature of the metal oxide as well as the type of precursor.[5] However, the calcination temperature has to be chosen with care in order to prevent the oxide crystallite from excessive sintering. Thermogravimetric analysis of pore templates as well as precursors facilitates the selection of the appropriate calcination temperature. So far, employing thermo analysis for the optimization of calcination conditions is not a standard procedure for the synthesis of templated metal oxides films with templated mesoporosity.

2.3.4. Synthesis Approach for Metal Oxides Powders

Metal oxide powders with templated mesoporosity can be synthesized employing either hard or soft-templating approaches. The most direct approach to obtain metal oxide powders with tem-

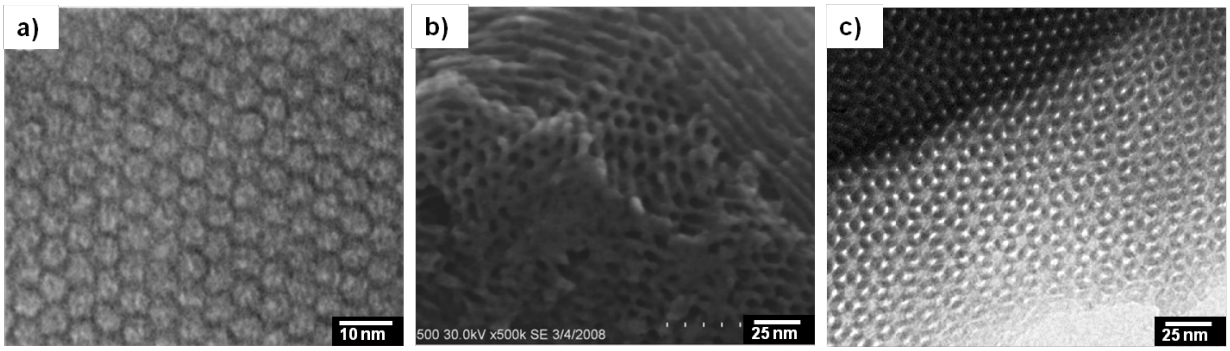

Figure 2.6.: Examples of silica materials with different pore structures and pore diamters a) TEM image of MCM-41 templated with CTACl[48] b) SEM image of SBA-15[36] templated with P123 c) TEM image of KIT-6 templated with a mixture of P123 and butanol[50]

plated mesostructure can be synthesized by soft-templating. In the first step, a sol-gel precursor and amphiphilic template are dissolved in a solvent, typically water or ethanol in analogy to film synthesis of mesoporous metal oxides. In contrast to EISA-based film synthesis (see section 2.3.3), the mesophase formation occurs in solution. The mesophase assembling occurs either cooperatively by the oxide precursor with ionic templates ("assembly driven by liquid crystal formation"[105]) or by infiltration of a (true) liquid crystal formed by block-copolymers with the precursor ("true liquid crystal templating"[106]).[107] The assembled templates are enclosed by the growing material network formed by polycondensation of the employed sol-gel precursors (see section 2.3.2). The solid mesophase assembly precipitates from the solution after a critical particle size is reached. The mesoporous metal oxide powder is obtained after filtration, washing and calcination to remove the template and crystallise the oxide lattice.

The first example of soft-templated oxide powders was published in 1992 from Mobile Company reporting the synthesis of the silica (called MCM-41) obtained from sodium silicate as oxide precursor and cetyltrimethylammonium chloride (CTACl) as pore template.[48] In the following years, the synthesis principle was extended for the synthesis of many other metal oxides powders with soft-templated mesopores for example: γ-Al_2O_3,[108] TiO_2,[88,109,110] ZrO_2,[111,88] V_2O_5,[112] Nb_2O_5,[113,88,114] Ta_2O_5[88,115] and WO_3[116,117]

However, silica is the most investigated oxide with templated mesopores. The simple handling of silica precursors and the easy synthesis protocols results in a wide range of accessible pore structures and diameters accessible for mesoporous SiO_2. Depending on the pore structure or employed template silica materials are named after the institution where the first synthesis succeeded, for example MCM-41,[48] KIT-6,[50] COK-12[118] and SBA-15.[49,57] Figure 2.6 presents exemplarily micrographs of a) TEM image of MCM-41 templated with CTACl b) SEM image of SBA-15[36] templated with P123 c) TEM image of KIT-6 templated with a mixture of P123 and 1-butanol.

Moreover, ordered mesoporous silica can be employed as hard template. In the so-called "nanocasting" approach[38] mesoporous silica is infiltrated by an oxide precursor solution. Afterwards, the oxide precursor infills the pore structure of silica template and is transformed into the oxide by calcination. In the last step the silica-mould is removed by etching and the desired oxide material is obtained in inverse shape of the initial silica pore structure.[38]

Nanocasting extended the range of accessible metal oxides powders with ordered mesoporosity, for example Co_3O_4,[119–121,36] Mn_xO_y,,[122] Fe_2O_3,[122] Cr_2O_3,[122–124] NiO,[122,124] CuO,[125] WO_3,[126] CeO_2[124] and In_2O_3[120,127] or non-oxide materials like the mesoporous carbon CMK-3.[53]

Mesoporous carbon CMK-3 can also be employed as hard template. The procedure for the so-called double replica approach is similar to the synthesis by nanocasting. The preformed mesoporous carbon is infiltrated with an oxide precursor solution. The precursor is transformed

into the desired metal oxide and the carbon hard-template is removed by oxidative decomposition. This so-called double replica approach can yield mesoporous oxide with the negative of the initial carbon pore structure, for example MgO,[128,129,55] SiO_2[130,51] and ZnO.[87,33] However, the double replica approach is time consuming and expensive due to many synthesis steps.

2.4. Aims of this Thesis

The oxidative coupling of methane (OCM) is proposed to be a key technology to overcome the dependency on crude oil of many branches of the chemical industry. However, the elementary steps of the OCM are still not fully understood. In particular, the role of the pore system in the proposed coupling between surface reaction and radical-based gas phase reaction has not been investigated so far. For the investigation of such effects OCM catalysts with narrow pore size distribution and the ability to control and tune the pore size are required.

Aim of this thesis is the development of synthesis procedures yielding model catalysts with controlled mesoporosity for the OCM reaction. The synthesis procedures have to yield catalysts with homogenous pore structure and controlled pore diameters. The pore system and material composition of the resulting materials have to be investigated by analytical methods. Thereafter, the performance of the obtained catalysts have to be tested in the OCM reaction. Finally, the correlation of C_2-selectivity and pore diameter can reveal insights of the proposed coupling between surface reaction and radical-based gas phase reaction in the OCM.

In this thesis the synthesis of MgO and Li@MgO OCM catalyst was first developed for mesoporous MgO films (see chapter 4). The new synthesis concept yielding not only ordered mesoporous MgO films, but also mesoporous films of Al_2O_3, ZnO and Co_3O_4 as well as the templated carbonate films of Mg, Al, Zn and Co is explained. The deduced criteria for the successful synthesis are discussed (see section 4.1). Thereafter, the composition of the new precursor complexes as well as their decomposition behaviour is analysed (see section 4.2) and limitations of the new concept are discussed. It will be demonstrated that employing these precursor complexes in EISA-based synthesis results in templated metal oxide and carbonates. For this purpose, the pore morphology, pore wall composition and crystallinity are characterized for films containing Mg (see section 4.3), Al (see section 4.4), Zn (see section 4.5) and Co (see section 4.6). Moreover, the versatility of the new concept is demonstrated by synthesizing and characterisation of ZnO with various pore sizes (see section 4.7). Finally, the criteria for a successful application of the new concept as well as its limitations are discussed in detail (see section 4.8).

After demonstrating the successful synthesis of micelle templated MgO films, the synthesis concept is transferred to obtain MgO and Li@MgO powders as OCM catalysts (see chapter 5). The synthesis and the characterisation in respect to pore morphology and crystallinity of the resulting MgO powders are presented (see section 5.1) before OCM testing. The catalytic performance of MgO and Li@MgO is discussed in section 5.2. Thereafter, the morphological and compositional properties of the catalysts after catalysis are characterized and changes of the catalysts are compared to the freshly prepared catalysts (see section 5.3). In the final section of this chapter the OCM performance is discussed in respect to the restructuring of the catalysts during OCM (see section 5.4).

In addition to MgO and Li@MgO, the W-Mn/SiO_2 OCM catalysts are synthesized with controlled mesoporosity (see chapter 6). It will be shown that the developed synthesis procedure yields W/Mn-SiO_2 OCM catalysts with a narrow pore size distribution and controlled pore morphology (see section 6.1). Employing different sized templates in this synthesis procedure yield a set of catalysts with pore diameters between 3.5 to 18 nm with comparable phase composition. It will be demonstrated that the synthesized catalysts are active and selective in OCM reaction (see section 6.2). The combined reproducibility of synthesis and OCM testing are subsequently estimated in section 6.3. Thereafter, the influence of the initial pore diameter on the C_2-selectivity at 775 °C and 800 °C is analysed and the results are discussed for mechanistic aspects of the OCM.

The effect of catalytic testing on the morphology and phase compositions of the catalysts after catalysis is analysed in section 6.5. In the final section of this chapter, the phase composition and OCM performance of the synthesized W-Mn/SiO_2 catalysts are compared to the literature and the influence of the pore diameter on the C_2-selectivity is discussed (see section 6.6).

3. Experimental

This chapter presents the synthesis procedures developed and applied in this thesis as well as the analytical methods. Section 3.1 lists the employed chemicals. Section 3.2 describes the synthesis of ordered mesoporous metal carbonates and metal oxides. In section 3.3 the synthesis of the OCM catalysts is explained. Section 3.4 describes the methods that were applied for material characterisation.

3.1. Chemicals

Zinc nitrate hexahydrate (98%, extra pure) and 1,3,5-trimethylbenzene (97%) were obtained from Acros. Aluminium nitrate nonahydrate (> 99%, pro analysis), magnesium nitrate hexahydrate (> 99%, pro analysis) and cobalt nitrate hexahydrate (> 98%, for analysis) were purchased from Merck. Water-free citric acid (> 99.5%, pro analysis) and HCl-solution (37%wt, pro analysis) were obtained from Roth. Concentrated sulfuric acid (95%wt, puriss) was purchased from Th. Geyer. Lithium nitrate (99.0%), nitric acid (65%wt) and ethanol (> 99.9%, absolute) were obtained from VWR. Sodium tungstate dehydrate (ACS), Pluronic F127, Brij56 and F108 were obtained from Sigma Aldrich. Pluronic P123 was purchased from BASF. PEO-PB-PEO polymers were synthesized by PSM Merseburg GmbH.[66] All chemicals were used without further purification.

3.2. Synthesis of Micelle-Templated Films of Metal Carbonate and Metal Oxide

All presented micelle-templated films were synthesized by dip-coating with controlled humidty, temperature and withdrawal rate using the dip-coater "Coater 5 AC" purchased from the company idLAB. Prior to film deposition the substrates (silicon-wafers and aluminium foil) were cleaned with ethanol and heated in air for 2 h at 600 °C. Single-side polished 500 - 600 μm thick silicon wafers in (111) or (100) orientation were used for electron microscopy and XRD measurements. Double-side polished 50 μm thick Si-wafers with (100) orientation were employed for SAXS measurements. BET-samples were prepared on aluminium foil.

All films were calcined in stagnant air directly after dip-coating. The films were placed into a preheated muffle furnace for calcination. The muffle furnace was held at constant temperature. After calcination the coated substrates were directly removed from the hot furnace and naturally cooled to room temperature. The starting materials, calcination time and temperatures are summarized in Table 3.1 for each respective type of film.

3.2.1. Magnesium Carbonate and Magnesium Oxide Films

Dip-coating solution for the synthesis of magnesium carbonate and magnesium oxide films were prepared by joining powders of the template PEO_{213}-PB_{184}-PEO_{213} (70 mg, 2.4 μmol), citric acid (144 mg, 0.75 mmol) and $Mg(NO_3)_2{\cdot}6\ H_2O$ (385 mg, 1.5 mmol). The joint powders were dissolved by adding a mixture of 1.5 ml ethanol and 1.5 ml milliQ water and applying subsequent ultrasound for two hours to obtain a clear solution. The solutions remained colourless and transparent for at least 8 weeks. In a next step the solution was filtered through a 0.2 μm syringe filter prior to film deposition. Films were then prepared by dip-coating of substrates at a withdrawal rate of 150 mm/min under controlled atmosphere (25 °C, 40% relative humidity). Thereafter, the films

Table 3.1.: Synthesis conditions employed for the preparation of micelle-templated mesporous carbonates and oxides of Zn, Al, Co and Mg. Column 1 features the sample name. Columns 2, 3 and 4 detail the compositions of the dip-coating solution, column 4 the calcination procedure (i) that yields the carbonate and column 5 the respective calcination (ii) that transforms the carbonate into the corresponding oxide

sample name	precursor system	template	(i) calcination to obtain the carbonate	(ii) calcination to obtain the oxide
Mg, large mesopores	$Mg(NO_3)_2$·6 H_2O & citric acid	PEO_{213}-PB_{184}-PEO_{213}	60 min/400 °C	120 min/400 °C + 60 min/600 °C
Al, large mesopores	$Al(NO_3)_3$·9 H_2O & citric acid	PEO_{213}-PB_{184}-PEO_{213}	60 min/300 °C	60 min/300 °C + 30 min/900 °C
Co, large mesopores	$Co(NO_3)_2$·6 H_2O & citric acid	PEO_{213}-PB_{184}-PEO_{213}	60 min/250 °C	60 min/250 °C + 20 min/300 °C
Zn, large mesopores	$Zn(NO_3)_2$·6 H_2O & citric acid	PEO_{213}-PB_{184}-PEO_{213}	60 min/250 °C	60 min/250 °C + 25 min/400 °C
Zn, medium mesopores	$Zn(NO_3)_2$·6 H_2O & citric acid	PEO_{104}-PB_{92}-PEO_{104}	60 min/250 °C	60 min/250 °C + 20 min/400 °C
Zn, small mesopores	$Zn(NO_3)_2$·6 H_2O & citric acid	PEO_{65}-PB_{59}-PEO_{104}	60 min/250 °C	60 min/250 °C + 20 min/400 °C
Zn, F127	$Zn(NO_3)_2$·6 H_2O & citric acid	PEO_{100}-PPO_{70}-PEO_{100}	60 min/250 °C	60 min/250 °C + 15 min/400 °C
Zn, bimodal mesopores	$Zn(NO_3)_2$·6 H_2O & citric acid	PEO_{213}-PB_{184}-PEO_{213} & PEO_{65}-PB_{59}-PEO_{104}	60 min/250 °C	60 min/250 °C + 20 min/400 °C

were allowed to dry in the dip-coater for at least 5 min. Films were then calcined in a preheated muffle furnace for either (i) 1 hour at 400 °C, or (ii) 3 hours at 400 °C followed by natural cooling to room temperature and subsequent calcining at 600 °C for 1 hour.

3.2.2. Aluminium Carbonate and Aluminium Oxide Films

The dip-coating solution for the aluminium carbonate and aluminium oxide films were prepared by mixing the powders of $Al(NO_3)_3$·$9H_2O$ (563 mg, 1.5 mmol), citric acid (144 mg, 0.75 mmol) and PEO_{213}-PB_{184}-PEO_{213} (70 mg, 2.4 μmol). The joint powders were dissolved by adding a mixture of 1.5 ml milliQ water and 1.5 ml ethanol and subsequent stirring over night resulting in a slightly yellow solution. In a next step the solution was filtered through 0.2 μm syringe filter prior to film deposition. Films were prepared by dip-coating of substrates at a withdrawal rate of 150 mm/min at 25 °C and 40% relative humidity. Thereafter, films were allowed to dry for at least 10 min in the dip-coater before transfer into the preheated muffle furnace. The mesoporous aluminium carbonate films were obtained after calcination (i) for 1 h at 300 °C. The mesoporous aluminium oxide films were obtained after calcination (ii) for 1 h at 300 °C, natural cooling to room temperature and subsequent calcination for 30 min to 900 °C in a preheated muffle furnace.

3.2.3. Zinc Carbonate and Zinc Oxide Films

The dip-coating solution for zinc carbonate and zinc oxide films were prepared by joining powders of $Zn(NO_3)_2$·$6H_2O$ (444 mg, 1.5 μmol), citric acid (144 mg, 0.75 mmol) and a polymer template. Either PEO_{213}-PB_{184}-PEO_{213} (70 mg, 2.4 μmol), PEO_{104}-PB_{92}-PEO_{104} (70 mg, 4.93 μmol), PEO_{65}-PB_{59}-PEO_{65} (70 mg, 7.9 μmol) or PEO_{106}-PPO_{70}-PEO_{106} (150 mg, 11.9 μmol) was employed as templates. The dual templated films were synthesized by employing PEO_{213}-PB_{184}-PEO_{213} (70 mg, 2.4 μmol) and PEO_{65}-PB_{59}-PEO_{65} (140 mg, 14.8 μmol) as templates. The

powders were dissolved by adding a mixture of milliQ water (1.5 ml) and ethanol (1.5 ml) and subsequent stirred over night resulting in a colourless solution. In a next step the solution was filtered through 0.2 μm syringe filter prior to film deposition. Films were then prepared by dip-coating of substrates at a withdrawal rate of 150 mm/min under controlled atmosphere (25 °C, 40% relative humidity). Thereafter, films were allowed to dry for at least 10 min in the dip-coater before being transfered into the preheated muffle furnace. Mesoporous $ZnCO_3$ films were obtained after calcination (i) for 1h at 250 °C. Mesoporous ZnO were obtained after calcination (ii) for 1h at 250 °C, natural cooling to room temperature followed by calcination at 400 °C for 25 min (mono templating PEO_{213}-PB_{184}-PEO_{213} and dual templating with PEO_{213}-PB_{184}-PEO_{213}/PEO_{65}-PB_{59}-PEO_{65}), 400 °C for 20 min (employing PEO_{104}-PB_{92}-PEO_{104} or PEO_{65}-PB_{59}-PEO_{65}), 400 °C for 15 min (employing PEO_{106}-PPO_{70}-PEO_{106}) in the preheated muffle furnace.

3.2.4. Cobalt Carbonate and Cobalt Oxide Films

The dip-coating solution for cobalt carbonate and cobalt oxide films were prepared by mixing the powders of $Co(NO_3)_2{\cdot}6H_2O$ (437 mg, 1.5 μmol), citric acid (144 mg, 0.75 mmol) and PEO_{213}-PB_{184}-PEO_{213} (70 mg, 2.4 μmol). The powders were dissolved by adding a mixture of milliQ water (1.5 ml) and ethanol (1.5 ml) and subsequente stirring over night resulting in a red/pink solution. In a next step the solution was filtered through 0.2 μm syringe filter prior to film deposition. Films were then prepared by dip-coating substrates at a withdrawal rate of 150 mm/min at 25 °C and 40% relative humidity. Thereafter, films were allowed to dry for at least 10 min before transfer into the preheated muffle furnace. The cobalt carbonate films employed calcination (i) for 1 h at 200 °C. Mesoporous cobalt oxide films were obtained after calcination (ii) for 1 h at 200 °C, natural cooling to room temperature and heating for 20 min at 300 °C in a preheated muffle furnace.

3.3. Synthesis of Micelle-Templated OCM Catalysts

3.3.1. MgO and Li@MgO

The MgO powder templated with PEO_{213}-PB_{184}-PEO_{213} was prepared by drying a solution containing $Mg(NO_3)_2{\cdot}6H_2O$, citric acid and the template followed by calcination. The template PEO_{213}-PB_{184}-PEO_{213} (1 g, 34.8 μmol) was dissolved in 15 ml ethanol by stirring over night at room temperature. Thereafter, citric acid (1.44 g, 7.5 mmol) and $Mg(NO_3)_2{\cdot}6H_2O$ (3.85 g, 15 mmol) were added as powders in this order to the template solution and dissolved by stirring for further 24 h resulting in a viscose, yellowish solution. The solution was then dried in a plain ceramic dish at 50 °C under an air stream yielding a transparent gel. Finally, the dish with the gel was heated with 5 K/min to 480 °C, kept there for 3 h followed by 500 °C for 1 h and naturally cooled to room temperature. This procedure results in 609 mg (yield: $>$ 99.9%) slightly greyish, light flakes.

The untemplated MgO powder was prepared drying a solution containing $Mg(NO_3)_2{\cdot}6H_2O$ and citric acid followed by calcination. Citric acid (1,44 g, 7.5 mmol) and $Mg(NO_3)_2{\cdot}6\ H_2O$ (3.85 g, 15 mmol) were mixed as powders and dissolved by adding 15 ml ethanol and applying ultrasound for 1 h resulting in a colorless solution. Thereafter, the solution was dried in a plain ceramic dish at 50 °C under an air stream yielding a transparent gel. Finally, the dish with the gel was heated with 5 K/min to 480 °C, kept there for 3 h followed by 500 °C for 1 h and natural cooled to room temperature. This procedure results in 591 mg (yield: 97.6%) slightly beige/grayish, light flakes.

The Li@MgO powder templated with PEO_{213}-PB_{184}-PEO_{213} was prepared drying a solution containing $Mg(NO_3)_2{\cdot}6H_2O$, $LiNO_3$ (6 mg, 0.09 mmol), citric acid and the template followed by calcination. The template PEO_{213}-PB_{184}-PEO_{213} (1 g, 34.8 μmol) was dissolved in 15 ml ethanol by stirring over night at room temperature. Thereafter, citric acid (1.44 g, 7.5 mmol), $LiNO_3$

(6 mg, 0.09 mmol) and $Mg(NO_3)_2{\cdot}6H_2O$ (3.85 g, 15 mmol) were added to the template solution as powders in this order and dissolved by stirring for further 24 h resulting in a viscose, yellowish solution. The solution then was dried in a plain ceramic dish at 50 °C under an air stream yielding a transparent gel. Finally, the dish with the gel was heated with 5 K/min to 480 °C, kept there for 3 h followed by 500 °C for 1 h and natural cooled to room temperature. This procedure results in 572 mg (yield: 94.5%) slightly grayish, light flakes.

The untemplated Li@MgO powder was prepared drying a solution containing $Mg(NO_3)_2{\cdot}6H_2O$, $LiNO_3$ and citric acid followed by calcination. Citric acid (1.44 g, 7.5 mmol), $LiNO_3$ (6 mg, 0.09 mmol) and $Mg(NO_3)_2{\cdot}6H_2O$ (3.85 g, 15 mmol) were mixed as powders and dissolved by addition of 15 ml ethanol and applying ultrasound for 1 h resulting in a colourless solution. Thereafter, the solution was dried in a plain ceramic dish at 50 °C under an air stream yielding a transparentgel. Finally, the dish with the gel was heated with 5 K/min to 480 °C, kept there for 3 h followed by 500 °C for 1 h and natural cooled to room temperature. This procedure results in 591 mg (yield: 91.1%) slightly beige/grayish, light flakes.

3.3.2. W-Mn/SiO_2

The W-Mn/SiO_2 OCM catalysts were obtained by a procedure combining the SBA- synthesis[49,57] and a sol-gel route[28] for this type of OCM catalyst. The pore sizes were varied by employing different sized polymer templates and swelling of the P123 micelles with different amounts of 1,3,5-trimethylbenzene (TMB).

For the preparation of the silica-based OCM catalysts with varied polymer templates 4 g of the respective polymer (Pluronic F127, Brij56, F108 or P123) was added into a 250 ml polypropylene hydrothermal flask, dissolved in 120 ml HCl-solution (2 mol/l) and additional 10 ml water resulting in a turbid solution. During dissolution the lid covered mixture was heated to 60 °C in a water bath and kept there for an additional hour. Thereafter, $Mn(NO_3)_2{\cdot}4H_2O$ (224 mg, 0.89 mmol) dissolved in 10 ml water was added to the now clear polymer solution. After additional 30 s $Na_2WO_4{\cdot}2H_2O$ (138 mg, 0.37 mmol) dissolved in 10 ml water was added resulting in a slightly yellow solution. After further stirring for 1 h, the solution was cooled down to 35 °C (in the case of F127 to 22 °C, see Zhao et al.[49]). Then, 9 ml $Si(OEt)_4$ (8.5 g, 40.8 mmol) was added by a glass pipette and the resulting mixture was vigorously stirred with closed lid for 20 h yielding a yellowish slurry. Afterwards, the flask was removed from the water bath and was transferred into the preheated furnace, to age at 80 °C for 21 h without stirring. In a next step the resulting yellowish solid was collected by filtration, washed several times with the filtrate and dried on the filter paper for at least 48 h at room temperature. The dried powder was then transferred from the filter paper to a plain ceramic dish, which was heated, thereafter, with 1 K/min in a tube furnace to 500 °C under air flow and kept at this temperature for 6 h prior to natural cooling to room temperature. The catalyst powder was obtained as yellowish powder.

For the preparation of the silica-based OCM catalysts with different amounts of swelling agent 4 g Pluronic P123 was added into a 250 ml polypropylene hydrothermal flask, dissolved by addition of 120 ml HCl-solution (2 mol/l) and additional 10 ml water resulting in a turbid solution. During dissolution the lid-covered mixture was heated to 60 °C in a water bath and kept there for an additional hour. Thereafter, $Mn(NO_3)_2{\cdot}4H_2O$ (224 mg, 0.89 mmol) dissolved in 10 ml water was added to the polymer solution. After 30 s $Na_2WO_4{\cdot}2H_2O$ (138 mg, 0.37 mmol) previously dissolved in 10 ml water was added resulting in a slightly yellow solution. After further stirring for 1 h, the solution was cooled down to 35 °C and 0.25 ml, 0.5 ml or 0.75 ml 1,3,5-trimethylbenzene (TMB) was added to the solution. After 30 min stirring with closest lid, 9 ml $Si(OEt)_4$ (8.5 g, 40.8 mmol) was added by a glass pipette and the resulting mixture was vigorously stirred with closed lid at 35 °C for 20 h yielding a yellowish slurry. Thereafter, the flask was removed from the water bath and was transferred into the preheated furnace, to age at 80 °C for 21 h without stirring. The resulting yellowish solid was collected by filtration, washed several times with filtrate and dried

on filter paper for at least 48 h at room temperature. The dried powder was then transferred from the filter paper to a plain ceramic dish. Thereafter, the dish with the obtained powders was heated with 1 K/min in a tube furnace to 500 °C in air flow and kept at this temperature for 6 h prior to natural cooling to room temperature. The catalyst powder was obtained as yellowish powder.

3.4. Characterisation Methods

Transmission Electron Microscopy (TEM)

Pore morphology and pore wall crystallinity were analysed by TEM measurements. TEM was recorded on a FEI Tecnai G 2 20 S-TWIN instrument operated at 200 kV on films scraped off from the substrates and transferred onto a copper grid coated with lacey carbon.

Scanning Electron Microscopy (SEM)

Pore morphology and crystallite size were analysed by SEM measurements. SEM imaging was performed using a JEOL 7401F instrument at 10 kV acceleration voltage and 4 mm working distance. Cross section images were recorded on a breaking edge. The edges were prepared immediately before the measurement by breaking the coated silicon wafer. Image J Version 1.44o (http://rsbweb.nih.gov/ij) was employed to determine pore diameter and film thickness.

Gas Physisorption

Poreshape, pore size distribution and BET surface area were determined by gas physisorption. Kr-adsorption isotherms were measured on film samples at 77 K with a Quantachrome Autosorb-1-C. The film samples were degassed in glass tube under vacuum at 150 °C for 2 h prior to physisorption. Thereafter, the glass tubes were naturally cooled to room temperature, filled with helium and subsequent transferred to the physisorption station of the Quantachrome Autosorb-1-C. Then, the physisorption data for 11 points between p/p_0 0.01 and 0.32 were collected. The surface area was calculated using the method of Brunauer-Emmett-Teller (BET). To determine the coating mass, the oxide films were dissolved and the concentration was measured at a Varian 715-ES ICP-OES. The MgO films were dissolved in a mixture of HCl-solution (2 ml, 37%wt), HNO_3 (6 ml, 65%wt) and 2 ml water by stirring at room temperature for 21 h. The Al_2O_3 films were dissolved in a mixture of H_2SO_4 (3ml, 95%wt) and H_3PO_4 (3 ml, 85%wt) for 30 min at 200 °C and 20 bar in a microwave (200 W). The ZnO films were dissolved in aqueous HCl-solution (8 ml, 37%wt) under stirring for 30 h at 25 °C. The Co_3O_4 films were dissolved in aqueous HCl-solution (8 ml, 37%wt) under stirring for 40 h at room temperature.

N_2-adsorption and desorption isotherms were measured on powder samples at 77 K with a Quantachrome Autosorb-1-C. The powder samples were degassed under vacuum at 150 °C for 2h prior to physisorption. Thereafter, the glass tubes were naturally cooled to room temperature, filled with helium and subsequent transferred to the physisorption station of the Quantachrome Autosorb-1-C. Then, the physisorption data for 89 points between p/p_0 0.01 and 0.99 were collected. Surface area was calculated using the method of Brunauer-Emmett-Teller (BET). The pore size distribution of MgO containing powders were calculated by applying the Barrett-Joyner-Halend (BJH) model on the desorption isotherm. The pore size distribution of W-Mn/SiO_2 powders were calculated by NLDFT model called "N2 at 77K on silica (cylindr./sphere. pore NLDFT ads. Modell)" integrated in the Quantachrome software AS1Win .

Small Angle X-ray Scattering (SAXS)

The pore order, d-spacing and pore structure were analysed by 2D-SAXS measurements. 2D-SAXS patterns of the templated metal carbonate and metal oxide films as well as the pristine W-Mn/SiO_2 catalysts were recorded at DORIS III storage ring, beamline B1 at DESY Hamburg with a PILATUS 1M detector (Dectris) at a sample-to-detector distance of 3589 mm or 1785 mm and X-ray energy of 16029 eV. Films were measured at 90° and 6° (for $MgCO_3$ and MgO at 90° and 13°) incident angle of the beam relative to the Substrate. The 2D-SAXS patterns of the W-Mn/SiO_2 catalysts after catalysis were recorded on a Bruker Nanostar using Cu-K_α-radiation. The W-Mn/SiO_2 powders were mounted on Scotch tape. The 2D-SAXS patterns were analysed using the Software Fit2D (Version 12.077).

Fourier Transform Infrared Spectroscopy (FTIR)

The composition of the decomposition products of precursor complexes were analysed by FTIR. The powder samples for FTIR were prepared by dissolving the metal nitrate and citric acid in a 2:1 molar ratio in ethanol followed by drying under reduced pressure. The yielded powders were calcined in the preheated muffle furnace on plain ceramic dishes at conditions analogue to the corresponding films (see table 3.1). FTIR spectra were recorded on a Perkin Elmer Spectrum 100 on samples pressed in KBr in transmission mode.

X-ray Diffraction (XRD)

The crystalline composition of film and powder samples was analysed by XRD. The XRD patterns were measured on a Bruker D8 Advance (Cu K_α-radiation). The film samples were measured in gracing incident configuration with an incident angle of the beam of 1° relative to the substrate. The powder samples were measured in Bragg-Brentano configuration. Bragg reflexes were assigned using PDFMaintEx library Version 9.0.133.

Thermogravimetry-Fourier Transformed Infrared Spectroscopy (TG-FTIR)

The decomposition behaviour of polymer template and metal precursor complexes were studied by thermogravimetry. The gaseous decomposition products were analysed simultaneously by FTIR. The dried metal complexes for TG-FTIR were prepared by dissolving the metal nitrate and citric acid in 2:1 molar ratio in ethanol followed by drying under reduced pressure. Thermogravimetry was measured on a Netzsch STA 409 PC with a heating rate of 5 K/min. The gaseous decomposition products were analysed with a connected Bruker Optik Equinox 55. Gas-phase IR spectra were assigned using the EPA vapour phase FTIR library.

Electron spray ionisation mass spectra (ESI-MS)

The composition of precursor complexes was studied by electron spray ionisation mass spectra (ESI-MS). Electron spray ionisation mass spectra (ESI-MS) of the Al, Zn and Co complexes were measured with a Thermo Scientific Orbitrap LTQ XL operating at a source voltage of 10 kV in anion mode. The ESI-MS spectrum of the Mg complex was recorded on a Micromass Bio-Q spectrometer with a cone voltage of 40 V in cation mode. The spray solutions were prepared by co-dissolving metal nitrates and citric acid in a 2:1 molar ratio in ethanol with a concentration of ~0.1 mg/ml and sprayed directly into the ESI-MS with a flow rate 5 μl/min.

3.5. Catalytic Tests

Catalytic tests on the OCM reaction were carried out in a multi-channel reactor system located at Leibniz Institute for Catalysis Rostock (LIKAT). This setup consists of 48 plug flow fixed-bed

quartz reactors with an inner diameter of 4 mm operating in parallel. The catalyst powder (MgO: 40 mg, W-Mn/SiO_2: 50 mg) was placed on a quartz wool plug and was covered with 300 mg SiC. The reactors filled with MgO derived catalyst were heated to 500 °C with 5 K/min under air prior to catalytic testing with CH_4/air feed (6:15 volume ratio) with a flow rate of 6 Nml/min at 500 °C, 550 °C, 600 °C, 650 °C, 700 °C, 750 °C, 800 °C.

The reactors filled with W-Mn/SiO_2 catalyst were heated to 600 °C with 5 K/min and from 600 °C to 775 °C with 2 K/min in air atmosphere. The catalysts were tested with CH_4/air (6:15 volume ratio) gas feed at 775 °C, 800 °C, 825 °C (Heating rate between steps 2 K/min) with 3 flow rates applied per each temperature subsequently (flow 1: 13.5 Nml/min; flow 2: 17.0 Nml/min; flow 3: 23.1 Nml/min). Afterwards the reactor was cooled down to 775 °C and the catalytic performance was tested agian at flow 1.

The feed components and the reaction products were analysed by an online gas chromatograph (Agilent 7890). The conversion of CH_4 was calculated from the inlet and outlet concentrations of CH_4. The product selectivities were calculated on the product basis. The GC analysis started after the system had reached reaction temperature and was carried out sequentially for each individual reactor.

4. Micelle-Templated Films of Metal Carbonates and Metal Oxides

In this chapter the new synthesis concept for the synthesis of micelle templated metal oxide and metal carbonates is presented. The concept is based on a new type of oxide precursors formed by metal nitrate and citric acid. Employing these precursors in the synthesis of mesoporous layers helps to overcome the limitation of the typically used precursors such as sol-gel, nanoparticles or salt precursors (see section 2.3.2).

In the following section 4.1 the new synthesis concept for the synthesis of micelle templated metal oxide and carbonate layers based on the EISA synthesis is described and the deduced requirements are explained. The complexation, composition in solution behaviour and thermal decomposition behaviour of the oxide precursors is analysed in section 4.2. Applying the synthesis concept enables the synthesis of micelle templated oxide and carbonate layers of magnesium, aluminium, zinc and cobalt. Their characterisation is described in sections 4.3 - 4.6. Moreover, the versatility of the concept is demonstrated by synthesizing ZnO with different pore sizes as well as dual templated layers (see section 4.7). Finally, the results are discussed in section 4.8.

4.1. General Synthesis Concept

Common soft-templating routines such as evaporation-induced self-assembling (EISA)[77] employ micelles of amphiphilic block copolymers as pore templates. In a typical EISA synthesis, a solution containing an oxide precursor and an amphiphilic block copolymer is deposited onto a substrate. The solvent evaporates during deposition while the template molecules arrange into micelles. Micelles and the partially condensed precursor assemble into an ordered mesophase. A subsequent calcination converts this mesophase into a mesoporous oxide film. However, neither the micelle-templated synthesis of Co_3O_4 films nor ZnO or MgO films have been reported so far.

The failure of EISA-based syntheses to produce templated zinc, magnesium or cobalt oxide films originates from the properties of commonly employed metal precursors. Typically oxides were synthesized from (I) alkoxides or partially alkoxylated metal chlorides (e.g. SiO_2,[82,84] TiO_2,[89,90] Al_2O_3,[131] ZrO_2[75,59]), (II) preformed colloidal nanocrystals (e.g. TiO_2,[83] Mn_3O_4,[96] $MnFe_2O_4$, $In_xSn_yO_z$ (ITO)[96,97]), and (III) thermally decomposable metal salts (e.g. IrO_2[40]). The reasons for failure are intrinsically tied to the mechanisms of mesophase formation and template removal (see section 2.3.2). Other constraining factors are limited solubility of many precursor compounds, melting during calcination or rapid crystallite growth of the metal oxide already before template removal. Additionally, a general limitation of all here described methods is that they do not provide access to the soft-templated synthesis of mesoporous metal carbonates.

This chapter will demonstrate that the self-assembly of triblock copolymers with citric-acid based metal complexes provides access to micelle-templated oxides and carbonates of zinc, cobalt and aluminium. Thus, mesoporous films of MgO, ZnO and Co_3O_4 as well as $MgCO_3$, $ZnCO_3$ and $Al_2(CO_3)_3$ with micelle-controlled pore structure become accessible for the first time. Based on a mechanistic understanding general criteria for the successful synthesis of metal oxides and metal carbonates with controlled porosity are deduced. The deduced criteria are illustrated in Figure 4.1 along with the proposed synthesis strategy:

1. Metal salt and ligands with carboxylic acid functionality must form a chemical complex. Chelating ligands are preferred due to the high stability of their complexes.

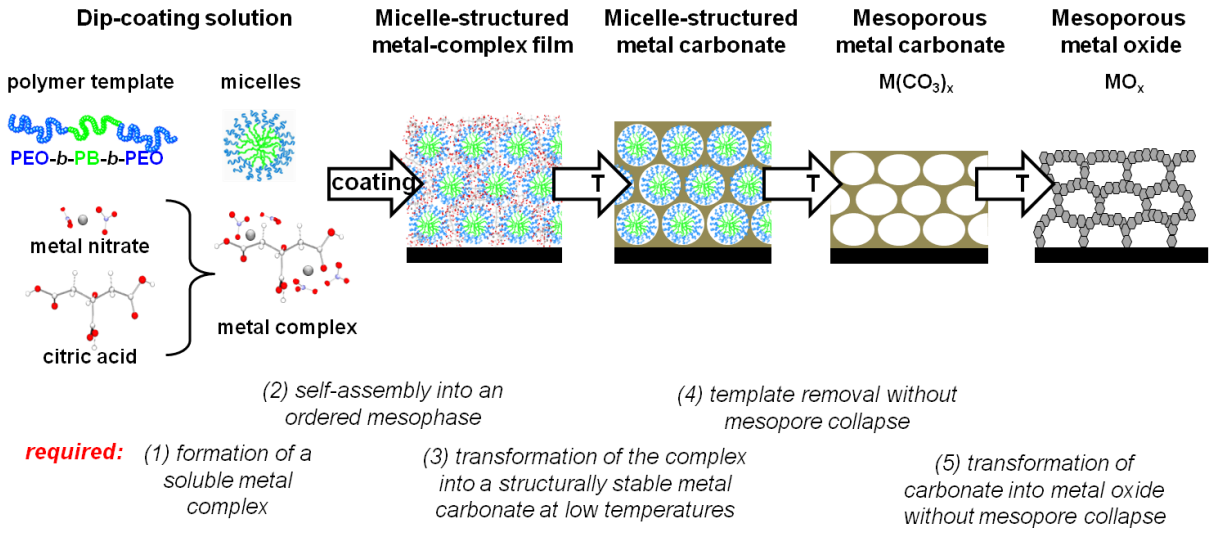

Figure 4.1.: Synthesis scheme and deduced requirements for the synthesis of mesoporous metal oxides via metal carbonate intermediates. 1) Formation of a soluble complex from metal nitrate and the complexing agent such as citric acid, 2) film deposition and concurrent self-assembly of the micelles of the polymer template with the precursor complex into an ordered mesophase, 3) decomposition of the precursor complex into a structurally stable metal-carbonate intermediate at low temperature while retaining the ordered mesophase, 4) thermal treatment in air to remove the polymer-template leading to open mesopores in the metal carbonate film 5) controlled decomposition of the amorphous carbonate that forms the pore walls into the nanocrystalline metal oxide.

2. Polymer micelles and metal complex must undergo self-assembly during deposition and drying to form an ordered mesostructure.

3. The chemical complex should decompose into a structurally stable metal carbonate at low temperatures while the templating micelles stabilize the formed mesostructure.

4. Subsequent template removal should yield the mesoporous metal carbonate, hence decomposition of the template polymer should occur at a temperature where the carbonate remains thermally stable.

5. The final thermal treatment should transform the carbonate into a nanocrystalline metal oxide while retaining the templated pores.

Guided by these requirements the physical and chemical processes that would constitute the synthesis of the mesoporous carbonate and oxide for the metals Mg, Al, Zn and Co were analysed. Formation of (1) a stable metal complex was studied by electron spray ionisation mass spectra (ESI-MS) of precursor solutions. Employing highly amphiphilic surfactants PEO-PB-PEO that form stable spherical micelles already prior to solution deposition assured (2) robust reproducible mesophase formation. Ordering of micelles and pore structures was assessed by small-angle X-ray scattering (SAXS). Adequate thermal treatment procedures for (3) carbonate formation, (4) template removal and (5) oxide formation were established based on thermogravimetric (TG) analysis of precursor complexes and templates. Additional characterisation revealed the structural evolution of the pore morphology (SEM, TEM) and surface area (Kr sorption) as well as phase composition (FTIR, XRD) and crystallinity of the pore walls (SAED, XRD). The derived mechanistic picture explains the formation of mesoporous carbonates and oxides. It reveals also why the synthesis of mesoporous $CoCO_3$ necessarily fails.

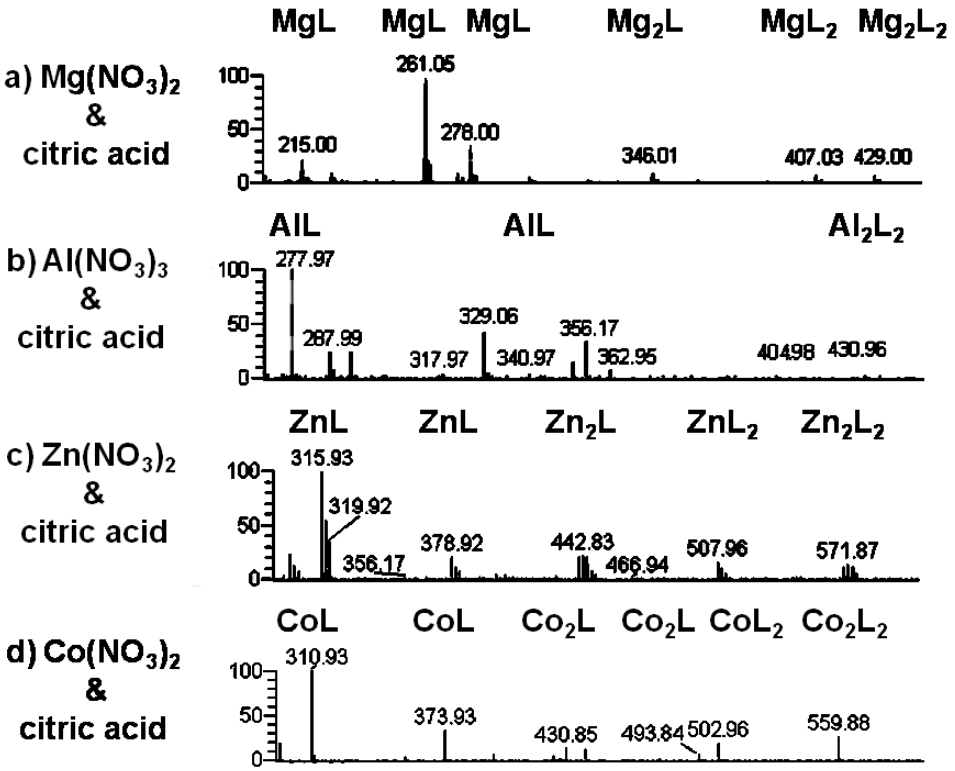

Figure 4.2.: Electron spray ionisation mass spectra of mixtures of citric acid with a) $Mg(NO_3)_2$ (cation spectra) b) $Al(NO_3)_3$ (anion spectra) c) $Zn(NO_3)_2$ (anion spectra) d) $Co(NO_3)_2$ (anion spectra). The characteristic mass fragments along with the corresponding isotope patterns are marked with the identified metal (M) to ligand (L) ratio.

4.2. Citric Acid Complexes with Metal Nitrates as Material Precursors

Complexation Behaviour of Citric Acid with Metal Nitrates

The proposed synthesis strategy (see section 4.1) requires the initial formation of a stable and soluble metal-precursor complex in solution (Figure 4.1, condition 1). The ability of citric acid to form complexes with the nitrates of Mg, Al, Zn and Co was therefore assessed by electron spray ionisation mass spectroscopy (ESI-MS) of the complex solutions.

The samples for ESI-MS were prepared by co-dissolving the powders of the metal nitrate and citric acid in ethanol (2:1 molar ratio). Different from the dip-coating solution, the concentration was reduced to ~0.1 mg/ml for instrumental reasons.

Figure 4.2 shows the mass spectra recorded from the solutions of citric acid and a) $Mg(NO_3)_2$ b) $Al(NO_3)_3$ c) $Zn(NO_3)_2$ d) $Co(NO_3)_2$. The characteristic mass fragments along with the corresponding isotope patterns are marked with the identified metal (M) to ligand (L) ratio. Along with these masses, signals corresponding to organic compounds derived from fragmentation of ligand and solvent were found. For clarity, these signals are not marked and the mass range was reduced to the part of the spectra containing mass patterns of metal complexes.

Figure 4.2a shows the mass spectra recorded in anion mode from magnesium nitrate and citric acid dissolved in ethanol (for details see Figure A.1). The identified complexes have different stoichiometries of magnesium and citric acid in the complexes, i.e. MgL (m/z 215.00 $[C_6H_7MgO_7]^+$,

m/z 261.05 $[C_8H_{13}MgO_8]^+$, m/z 278.00 $[C_6H_8MgNO_{10}]^+$), Mg_2L (m/z 346.01$[C_8H_{12}Mg_2NO_{11}]^+$), MgL_2 (m/z 407.03 $[C_{12}H_{15}MgO_{14}]^+$), Mg_2L_2 (m/z 429.00 $[C_{12}H_{13}Mg_2O_{14}]^+$).

These identifications of complexes magnesium nitrate with citric acid confirm the strong tendency of citric acid to bond to magnesium ions. Therefore, most likely the magnesium nitrate and citric acid also interact in the dipcoating solution forming a precursor complex.

The mass spectrum for aluminium nitrate and citric acid in ethanol (Figure 4.2b) recorded in anion mode shows characteristic mass fragments along with the corresponding isotope patterns of aluminum citric acid complexes (for details see Figure A.2). Masses corresponding to complex stoichiometries AlL (m/z 277.97 $[C_6H_5AlNO_{10}]^-$, m/z 340.97 $[C_6H_6AlN_2O_{13}]^-$) and Al_2L_2 (m/z 430.96 $[C_{12}H_9Al_2O_{14}]^-$) are observed.

These findings confirm the tendency of citric acid to bind to aluminium. However, the mass spectra show the least diversity of metal to ligand ratio compared to Mg, Zn and Co complexes, maybe due to a weaker interaction of the ligand to aluminum or alternative fragmentation mechanisms preventing the detection of labil complexes.

The mass spectrum recorded from a solution containing zinc nitrate and citric acid in ethanol (Figure 4.2c) shows characteristic mass fragments along with the corresponding patterns of complexes formed by zinc nitrate and citric acid (for details see Figure A.3). Most of the observed masses can be assigned to zinc ions bonded to citric acid with nitrate as counter ions. The identified complexes have different stoichiometries of Zn and citric acid in the complexe, i.e. ZnL (m/z 315.93 $[C_6H_6NO_{10}Zn]^-$, m/z 378.92 $[C_6H_7N_2O_{13}Zn]^-$), Zn_2L (m/z 442.83 $[C_6H_5N_2O_{13}Zn_2]^-$), ZnL_2 (m/z 507.97 $[C_{12}H_{14}NO_{17}Zn]^-$), Zn_2L_2 (m/z 571.87 $[C_{12}H_{12}NO_{17}Zn_2]^-$).

This identification of citric acid complexes with zinc ions confirm the strong complexation tendency. Presumably, this complexes are also present in dip-coating solution.

Figure 4.2d shows the mass spectra recorded in cation mode from magnesium nitrate and citric acid dissolved in ethanol for detailed correlation (for details see Figure A.4). The identified complexes corresponding to complex stoichiometries CoL (m/z 310.93 $[C_6H_6CoNO_{10}]^-$, m/z 373.93 $[C_6H_7CoN_2O_{13}]^-$), Co_2L (m/z 430.85 $[C_6H_5Co_2N_2O_{13}]^-$, m/z 493.84 $[C_6H_6Co_2N_3O_{16}]^-$), CoL_2 (m/z 502.96 $[C_{12}H_{14}CoNO_{17}]^-$) and Co_2L_2 (m/z 559.88 $[C_{12}H_{12}Co_2NO_{17}]^-$). These findings confirm the strong complexation tendency of citric acid to cobalt ions and support the assumption of present cobalt citric acid complexes in the coating solution.

In summary, the recorded ESI mass spectra indicate the formation of complexes between the metal ions Mg, Al, Zn and Co with citric acid. This leads to the assumption that complexes of citric acid with metal nitrate are present in the dip coating solution forming the oxide precursor. However, whether the binuclear complex with the stoichmetry M_2L_2 represents the precursor or only a fragment of a larger complex or even a network cannot be distinguished from the present data.

Decomposition Behaviour of Pore Template and Precursor Complexes

The proposed synthesis strategy (see section 4.1) requires the decomposition of the precursor complex into carbonate at temperatures where the template polymer remains sufficiently stable (Figure 4.1, step 3). Moreover, access to the mesoporous carbonate implies that the template removal (Figure 4.1, step 4) occurs prior to carbonate decomposition into the oxide (Figure 4.1, step 5). The thermal stability of template polymer and of different dried precursor complexes was therefore investigated by TG analysis in air with a heating rate of 5 K/min.

The recorded TG curves are presented in Figure 4.3 showing the decompostion behaviour of the template polymer (Figure 4.3a) with that of the citric acid complexes of Mg (Figure 4.3b), Al (Figure 4.3c), Zn (Figure 4.3d) and Co (Figure 4.3e).

TG indicates that the polymer template (Figure 4.3a) starts to decompose at a temperature above 250 °C. However, a rapid mass loss related to combustion of the polymer occurs between 375 - 425 °C. The thermal stability of the polymer is therefore in line with literature reports, where

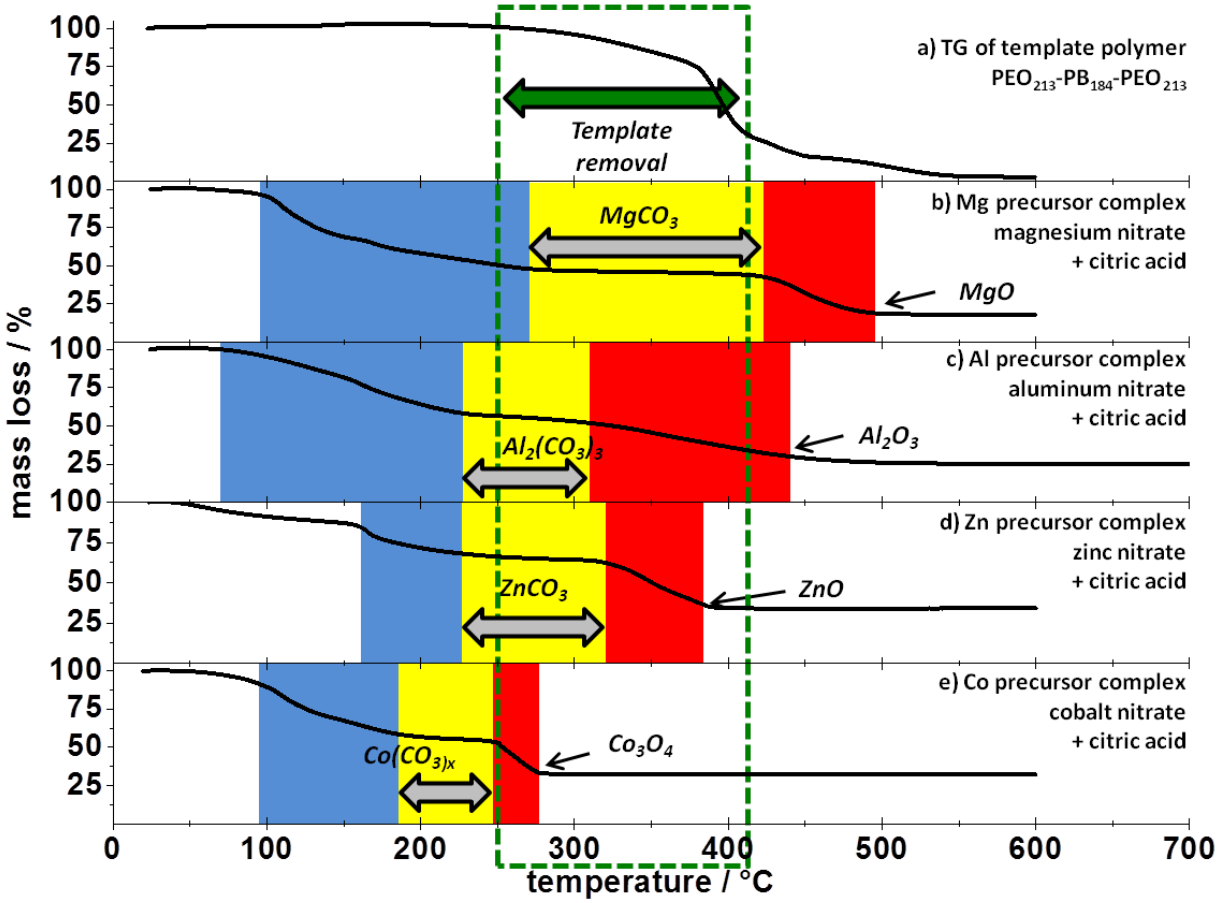

Figure 4.3.: Thermogravimetric analysis recorded for a) the polymer PEO_{213}-PB_{184}-PEO_{213} and (b-e) dried complexes of citric acid with different metal nitrates: b) $Mg(NO_3)_2$ c) $Al(NO_3)_3$ d) $Zn(NO_3)_2$ e) $Co(NO_3)_2$. The colors mark different temperature ranges of thermal modification of template polymer and of the metal complexes. The green frame highlights the temperature range of the decomposition of the template polymer. Colored areas indicate the evolution of the metal complexes: 1. (blue) decomposition of the precursor complex into the corresponding carbonate, 2. (yellow) existence of the metal carbonate and 3. (red) decomposition of the carbonate into the metal oxide. The heating was conducted with a rate of 5 K/min in air

decomposition temperatures between ~200 °C (PEO_{106}-PPO_{70}-PEO_{106} , Pluronic F127)[103] and ~400 °C (PEO_{79}-PHB_{89}, KLE)[104] have been observed.

The TG curves of all studied metal complexes show a similar typical shape (Figure 4.3b/c/d/e). An initial mass loss of about 30 to 50% is followed by a plateau of constant mass and another mass loss. Between 20 and 35% of the initial mass are retained in the final stage.

The TG curve of magnesium complexed with citric acid exhibits a first weight loss between temperatures of about 100 °C and 270 °C forming a stable intermediate. This intermediate is mass stable between 270 °C and 425 °C. The second weight loss occurs between 425 °C and 500 °C, suggesting the decomposition of the stable intermediate into MgO. FTIR analysis of the gas phase recorded at 425 °C detects only carbon dioxide as product of this second decomposition step (Figure A.5). CO_2 evolution can result from two processes, the oxidation of organic residue and the decomposition of magnesium carbonate. The oxidation of organic residues would result in the products water and CO_2. Since, no additional signal corresponding to water was detected, the CO_2 signal must be originated in carbonate decomposition. Hence, deposited films were calcined at 400 °C (i) to obtain the magnesium carbonate and further calcined at 600 °C (ii) yielding magnesium oxide (see section 4.3).

In the TG measurement of aluminium citric acid complex, a first weight loss is observed between temperatures of about 100 °C and 225 °C forming a stable intermediate. This intermediate is mass stable between 225 °C and 310 °C. The second mass loss occur at 310 °C indicating the decomposition of the intermediate into the final aluminum oxide. FTIR analysis of the gas phase recorded at 400 °C shows only signals corresponding to CO_2 indicating decomposition of the intermediate aluminum carbonate intro aluminum oxide. Thus, deposited films were calcined at 300 °C (i) to obtain the aluminum carbonate and further calcined at 900 °C (ii) yielding aluminum oxide.

The TG-measurement of the zinc citric acid complex shows the first significant mass loss between 160 °C and 225 °C (Figure 4.3d). The plateau of constant mass extends up to 320 °C, whereas a constant mass is reached at about 380 °C. The FTIR spectrum recorded at 350 °C (Figure A.7) feature only signals corresponding to CO_2 indicating the decomposition of intermediate zinc carbonate. Hence, deposited films were calcined at 250 °C (i) to obtain the zinc carbonate and further calcined at 400 °C (ii) yielding zinc oxide.

The TG curve obtained from cobalt citric acid complex exhibits the first mass loss between 100 °C to 190 °C into an stable intermediate which decompose at ~245 °C. FTIR analysis of the gas phase recorded at 400 °C (Figure A.8) shows signals corresponding to CO_2 indicating decomposition of the intermediate cobalt carbonate as well as signals representative for C-H vibration suggesting risidues of citric acid. Hence, the decomposition of the intermediate cobalt carbonate occurs prior to the decomposition of the polymer template cobalt carbonate cannot be synthesized in mesoporous form. Deposited films were therefore calcined at (i) 200 °C to stabilize the carbonate and (ii) 300 °C to obtain a mesoporous cobalt oxide.

In summary, the TG-curves of the dried oxide precursor complexes of citric acid and Mg, Al, Zn or Co show similar shapes. Stable intermediated carbonate forms after a first mass loss at relatively low temperature. This intermediate decomposes into the final oxide material. However, the decomposition temperature of the intermediate carbonate varies significantly with the employed metal. $MgCO_3$, $Al_2(CO_3)_3$ and $ZnCO_3$ decompose at temperatures above the template decomposition temperature at ~250 °C. In contrast, $Co(CO_3)_x$ reacts to Co_3O_4 already at ~245 °C. Access to the mesoporous carbonate implies that the template removal must occur prior to the decomposition of the carbonate into the oxide. Therefore, cobalt carbonate can presumably not be obtained in a mesoporous form. However, Mg, Al and Zn should be avaible in the form of mesoporous carbonates with the employed PEO-PB-PEO polymer template.

4.3. Magnesium Carbonate and Magnesium Oxide

MgO-based catalysts are promising candidates for the oxidative coupling of methane (OCM), which has been proposed as a key-technology to overcome the dependency on petroleum of many branches of the chemical industry.[4,3] The OCM reaction is supposed to be a combination of surface and gas phase reaction. Therefore, the activity and selectivity of the reaction should depend on the pore surface to pore volume ratio, which can be controlled by adjusting the pore size. However, the synthesis of direct soft templated magnesium oxide failed so far.

In this section the synthesis and material analysis of micelle templated MgO and $MgCO_3$ films is presented. The applied procedure is a model synthesis for soft-templated MgO powders with tailored pore diameter.

Briefly, magnesium containing films were synthesized by dip-coating. The dip-coating solution was prepared by co-dissolving the joined powders of $Mg(NO_3)_2{\cdot}6H_2O$, citric acid and PEO_{213}-PB_{184}-PEO_{213} polymer template in a 1:1 water-ethanol mixture. The layers were synthesized by dip-coating on a silicon substrate and subsequent calcination. According to thermo gravimetric analysis results (see section 4.2) the calcination temperatures and times are selected to 1 hour at 400 °C (i) to synthesis the magnesium carbonate and 3 hours at 400 °C followed by 1 hour at 600 °C (ii) to obtain mesoporous magnesium oxide.

Figure 4.4 presents for the Mg-based materials templated with PEO_{213}-PB_{184}-PEO_{213} (i) calcined for 1 hour at 400 °C the analysis of $MgCO_3$ by SEM (a), FTIR (b), XRD (c) as well as for the corresponding MgO (ii) calcined for 3 hours at 400 °C followed by 1 hour at 600 °C SEM (d), FTIR (e), XRD (f), TEM (g, h) and SAED (i).

The cross section SEM image (Figure 4.4a) of sample (i) indicates a homogenous film with a film thickness of 252 nm. The film is completely penetrated by mesopores with a slightly elliptically shape of 20 nm x 16 nm in size. The appearance of the walls is smooth and unstructured; no crystallites can be distinguished. FTIR analysis (Figure 4.4b) reveals two characteristic bands indicative of magnesium carbonate, i.e. asymmetric (1420 cm^{-1}) and symmetric (1595 cm^{-1}) stretching vibrations.[86] The weak signal at 500 cm^{-1} can be assigned to Mg-O vibrations indicating a small amount of MgO in the sample calcined for 1 hour at 400 °C. Complementary XRD analysis (figure 4.4c) feature weak reflections at 43° and 63° corresponds well with the (200) and (220) reflections of MgO in periclase structure (PDF-No. 00-045-0946) and is indicative of beginning MgO crystallization. The crystallite size estimated via Scherrer equation amount to 5 nm. X-ray diffractogram does not show any reflections corresponding to $MgCO_3$. Therefore the carbonate is present in X-ray amorphous form. TEM analysis confirms the FTIR and XRD results by showing the pore walls to be mostly amorphous, yet containing few crystallites of MgO as dark spots in HRTEM and bright spots in DFTEM images (Figure A.10a/b), respectively. Kr-physisorption analysis amounts to 63 m^2/g. This surface area indicates open porosity when compared to the surface area reported for open porous films in literature.[5] Thus, after calcination (i) at 400 °C for 1 h the layers are present as mesoporous $MgCO_3$ in amorphous form with few MgO crystallites.

After calcination for 3 hours at 400 °C followed by 1 hour at 600 °C (ii) the FTIR spectrum (Figure 4.4e) show a strong signal at 500 cm^{-1} indicative of MgO, whereas only small bands assigned to carbonate are retained. The X-ray diffractogram of the layered sample (Figure 4.4f) shows, in comparison to calcination (i) sharpened reflections at 43° and 63° correspond well with the (200) and (220) reflections of MgO in periclase structure (PDF-No. 00-045-0946). Crystallite sizes estimated via Scherrer equation amount to 7 nm.

The corresponding top-view SEM image (Figure 4.4d) indicates that films remain homogeneous and macroscopically crack-free. The films are completely penetrated by mesopores ∼18 nm in diameter. The pores are locally ordered and open toward the outer film surface. TEM analysis (Figure 4.4g) confirms the presence of template mesopores throughout the sample volume. High-resolution TEM (Figure 4.4h) indicates crystallites and lattice fringes, which confirms that the

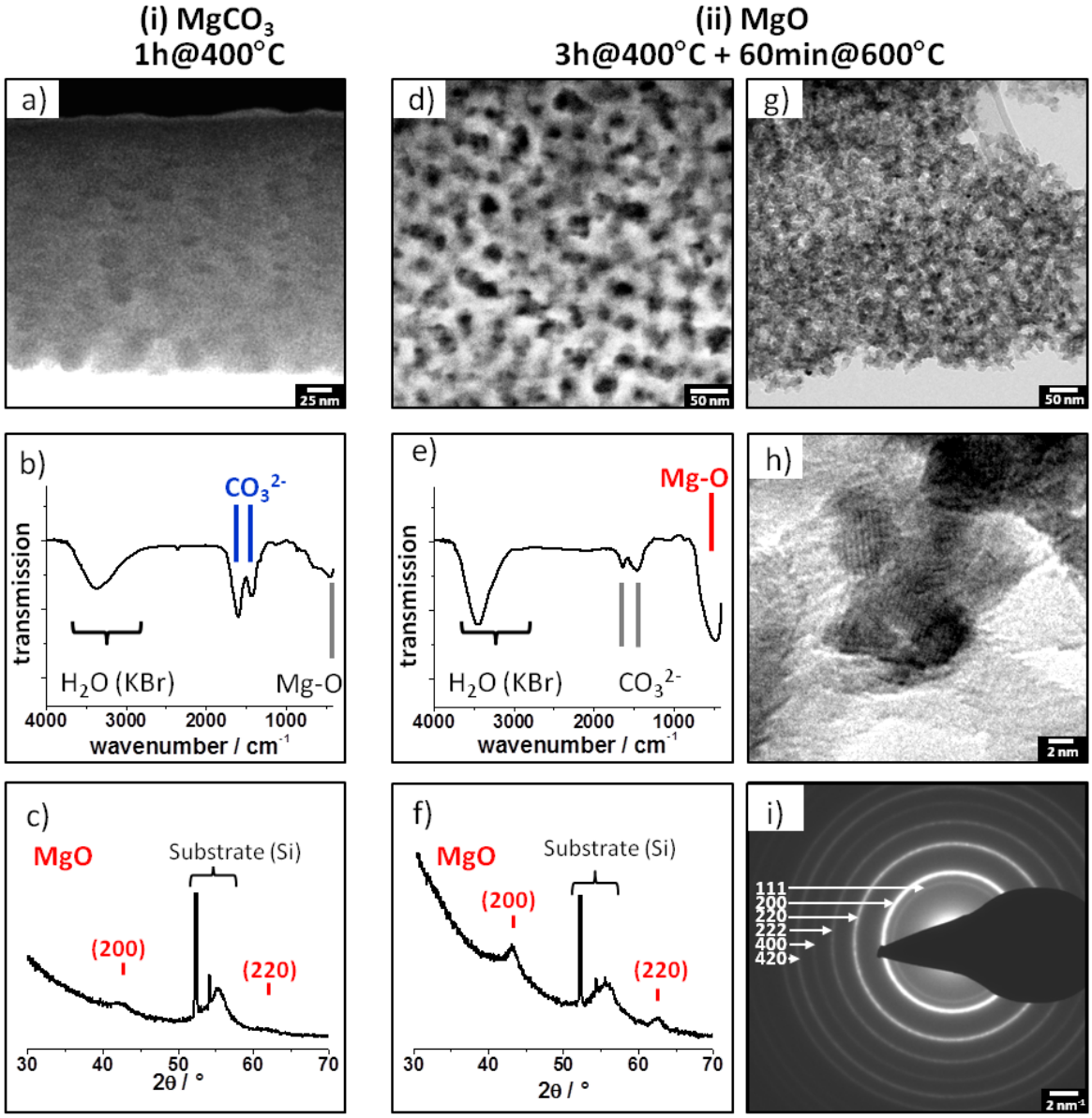

Figure 4.4.: Analysis of (i) mesoporous $MgCO_3$ calcined 1 hour at 400 °C and (ii) of mesoporous MgO calcined for 3 hour at 400 °C followed by 1 hour at 600 °C by SEM (a, d), FTIR (b, e), XRD (c, f), TEM (g, h) and SAED (i). a) cross-section SEM of mesoporous $MgCO_3$ film with inset at higher magnification, b) infrared-spectrum of the precursor complex calcined at 400 °C recorded in transmission, c) gracing incident XRD analysis of amorphous $MgCO_3$ (i). d) SEM top-view image of MgO (ii), e) FTIR spectrum of dried precursor complex calcined by procedures (i)+(ii), f) XRD analysis of MgO (ii) with reflection positions corresponding to MgO in periclase structure (PDF-No. 00-045-0946). Figures g), h) and i) present electron microscopy analysis of (ii) MgO by g) bright-field TEM, h) high-resolution TEM and i) selected-area electron diffraction SAED (indexing: hexagonal zincite structure, PDF-No. 00-045-0946).

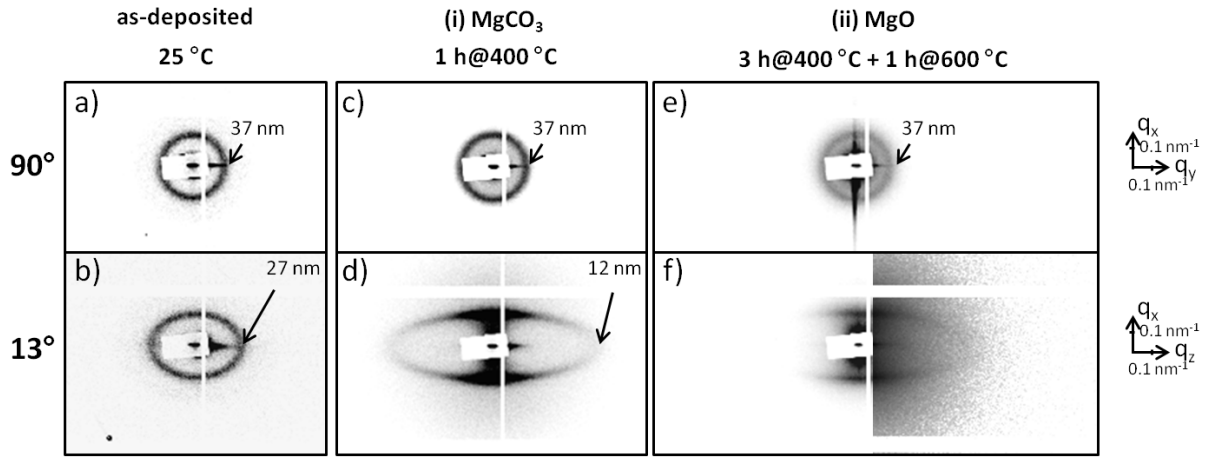

Figure 4.5.: 2D-SAXS pattern of films deposited from solutions with the complex of magnesium nitrate and citric acid as well as micelles of the polymer template PEO_{213}-PB_{184}-PEO_{213} after different thermal treatments. From left to right: (a, b) as-deposited, (c, d) magnesium carbonate (i) calcined for 1 hour at 400 °C and (e, f) magnesium oxide (ii) calcined for 3 hour at 400 °C followed by 1 hour at 600 °C. Samples were analysed by SAXS with two different incident angles of the X-ray beam of 90° (upper panel) and of 13° (lower panel) relative to the substrate surface. Linear intensity scale and inset with logarithmic in f).

pore walls are crystalline. Furthermore, SAED analysis (Figure 4.4i) shows isotropic diffraction rings with ring positions that match the reflections of MgO in periclase structure (PDF-No. 00-045-0946). Kr-physisorption analysis amounts to 151 m^2/g and is therefore approximately 3 times higher compared to $MgCO_3$. Thus, after 3 hours at 400 °C and 1 hour at 600 °C mesoporous MgO is present in nanocrystalline form.

Finally, the evolution of pore morphology upon film deposition and calcination was analysed using 2D-SAXS in transmission mode at an incident angle of 90° (beam perpendicular to the substrate) and of 13°, respectively (Figure 4.5). The diffraction pattern obtained for the as-deposited film at an incident angle of 90° (Figure 4.5a) shows an isotropic ring corresponding to a mesoscopic order of the polymer micelles parallel to the substrate at a d-spacing of 37 nm. Both, isoptropic ring and d-spacing, are preserved upon heat treatment (i) and (ii). The 2D-scattering patterns recorded on all films at an incident angle of 13° (Figure 4, lower panel) contain rings of elliptical shape. The shape results from film shrinkage perpendicular to the substrate and corresponding deformation of the pore system upon drying and calcination. Such shrinkage is typically observed for micelle-templated oxide films and leads to elliptical deformation of the pore shapes. The d-spacing perpendicular to the substrate amounts to 27 nm directly after dip-coating. It decreases to 12 nm upon calcination at 400 °C (i), but remains almost unchanged by subsequent treatment at 600 °C (ii). However, the elliptical shape of the 2D-SAXS pattern after calcination (ii) is no longer closed, which suggests a restructuring of the mesopore network perpendicular to the substrate due to growth of MgO crystallites. However, the SAXS data clearly prove that micelles of the employed block-copolymer structure the deposited mesophase and undergo local ordering. Moreover, the mesostructure is transferred into ordered porosity upon calcination.

In summary, employing the material precursor formed by complexing magnesium nitrate with citric acid allows the synthesis of micelle templated magnesium carbonate and magnesium oxide for the first time. The ordered mesoporous magnesium carbonate appears X-ray amorphous, but yet shows few MgO crystallites. Further calcination fully transforms $MgCO_3$ into nanocrystalline MgO under preservation of the pore structure. The syntheses of $MgCO_3$ and MgO as micelle templated films were not reported so far. Thus, employing the new synthesis concept presented in section 4.1 enables the synthesis of micelle templated $MgCO_3$ and MgO for the first time.

After successfully developing a model synthesis for a soft-templated MgO, the procedure was

transferred to synthesize direct soft templated MgO powders as catalyst for OCM reaction (see section 5).

4.4. Aluminum Carbonate and Aluminum Oxide

Alumininum oxide has been widely applied in catalysis as inert support for active metals, e.g. as washcoat on car catalytic converter[9] or in hydrochlorination of 1,2-dichloropropane.[132] Moreover, porous alumina powder is used as adsorbent in waste water treatment or as membranes in ultrafiltration.[133] Ordered mesoporous Al_2O_3 films usually employ aluminium chloride or aluminium alkoxides (e.g. AlO^iPr,[134] $AlO^{sec}Bu$,[60]) as material precursors. However, using the sol-gel approach with $AlCl_3$ needs long reaction times between 7 - 14 days ageing of the solution prior to coating.[131] Moreover, aluminum alkoxides are difficult to handle due to their hydrolysis sensitivity and need rather strict control over synthetic conditions to yield mesoporous alumina films.[60] Moreover, aluminium carbonate is not accessible by employing chlorides or alkoxides. In this section the synthesis and charcterisation of $Al_2(CO_3)_3$ and Al_2O_3 is presented.

Briefly, mesoporous $Al_2(CO_3)_3$ and Al_2O_3 were synthesized by dip coating and subsequent calcination. The dip-coating solution was prepared by co-dissolving the joined powders of citric acid, $Al(NO_3)_3{\cdot}9H_2O$ and PEO_{213}-PB_{184}-PEO_{213} polymer template in a 1:1 water-ethanol mixture. The layers were synthesized by dip-coating on a silicon substrate and subsequent calcination. According to thermogravimetric analysis results (see section 4.2) the calcination temperatures and times are selected to 1 hour at 300 °C (i) to synthesize the mesoporous aluminium carbonate and thereafter for 30 min at 900 °C (ii) to obtain the mesoporous oxide.

Figure 4.6 presents for the Al-based materials templated with PEO_{213}-PB_{184}-PEO_{213} (i) calcined for 1 hour at 300 °C the analysis of $Al_2(CO_3)_3$ by SEM (a), FTIR (b), XRD (c) as well as for the corresponding Al_2O_3 (ii) calcined with additional 900 °C for 30 min SEM (d), FTIR (e), XRD (f), TEM (g, h) and SAED (i). The cross-section SEM image (see Figure 4.6a) shows the film after calcination at 300 °C (i). The film is fully penetrated by templated mesopores with the typical elliptical shape and a size of about 20 nm in width and 9 nm in height. FTIR analysis (Figure 4.6b) reveals two characteristic bands indicative of aluminium carbonate, i.e. asymmetric (1608 cm^{-1}) and symmetric (1469 cm^{-1}) stretching vibrations.[86] X-ray diffractogram (Figure 4.6b) does not show any signals corresponding to Al containing phases and, therefore, can be considered X-ray amorphous. Kr-physisorption amounts to a BET surface area of 44.8 m^2/g. Hence, thermal treatment (i) of the deposited film forms amorphous mesoporous aluminium carbonate.

The SEM image recorded of the Al-containing film after additional calcination at 900 °C (ii) shows that the film contains templated mesopores of about 22 nm in diameter (Figure 4.6d). TEM analysis confirms that the film is fully mesoporous (Figure 4.6g) and composed of small crystallites of about 6 nm in diameter (Figure 4.6h). The dark-field TEM image (Figure A.9b) shows equally sized bright spots corresponding to wall crystallites. The crystallites have a narrow size distribution with an average size of 6 nm. Two vibrations observed at 538 cm^{-1} and 732 cm^{-1} indicative of Al-O bonds and the absence of carbonate-related vibrations in FTIR-spectra evidence the formation of aluminium oxide (Figure 4.6e).[135,136] XRD analysis detects two broad reflections at 46.0° and 66.6° (Figure 4.6f), which correspond well with the position of (400) and (440) reflections reported for γ-Al_2O_3 (PDF: 00-050-0741). The crystallite size estimated via Scherrer-equation amounts to 5 nm and is in good agreement with the TEM study. Diffraction rings observed in SAED correspond to (311), (400), (511), (440), (444) and (800) reflections of γ-Al_2O_3 (Figure 4.6) and confirm the phase assignment. Kr-BET surface area of the oxide amounts to 286 m^2/g. Hence, calcination (ii) at 900 °C transforms mesoporous aluminium carbonate into crystalline γ-alumina with templated mesopore structure.

Mesoscale order in Al-containing films was analysed after different thermal treatments of deposited films. Figure 4.7 details the evolution of order from deposited micelles (a, b) to (i) porous $Al_2(CO_3)_3$ (c, d) and (ii) Al_2O_3 (e, f) as indicated by 2D-SAXS recorded in transmission at beam

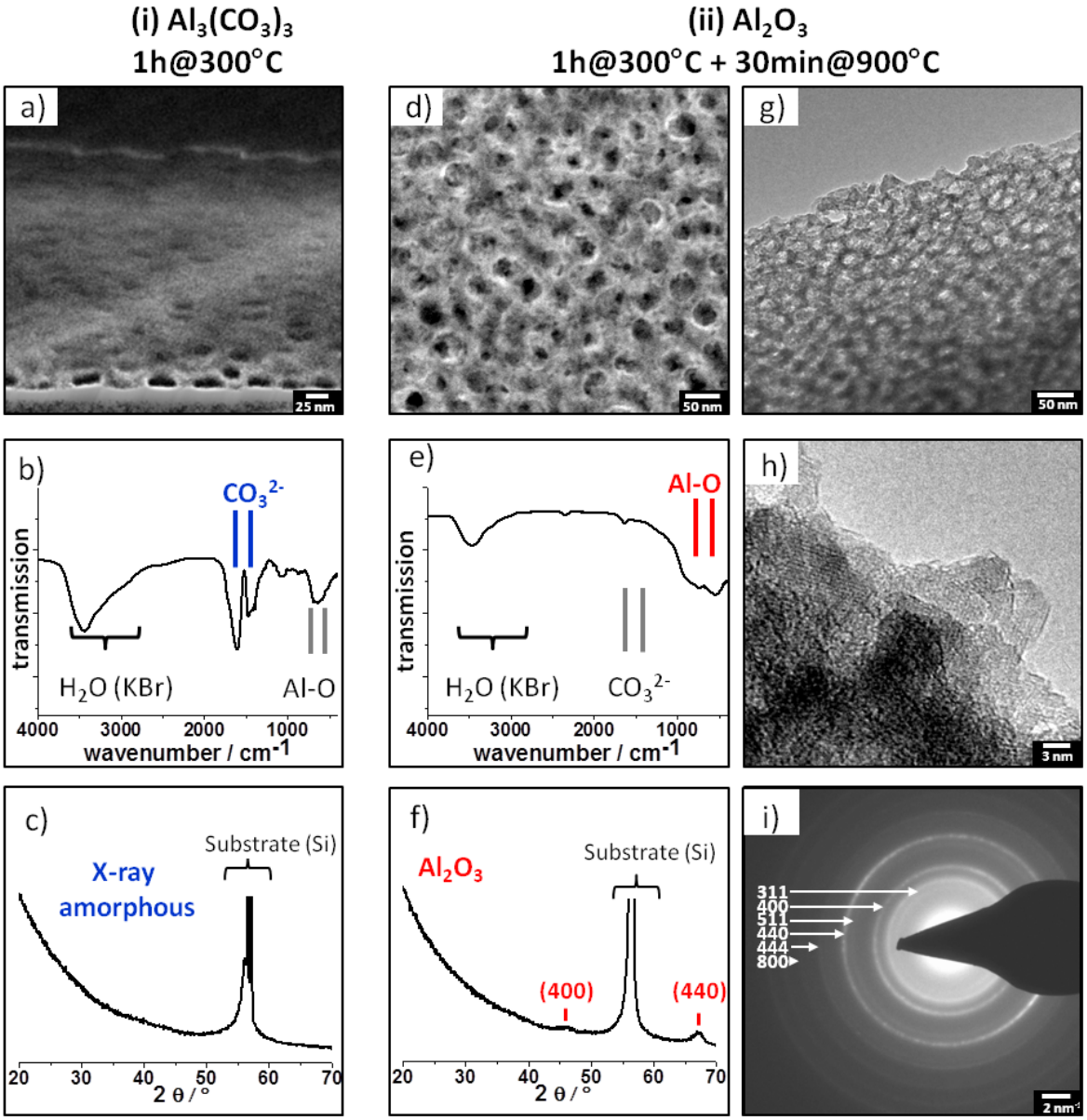

Figure 4.6.: Analysis of (i) mesoporous $Al_2(CO_3)_3$ calcined 1 hour at 300 °C and (ii) of mesoporous Al_2O_3 calcined for 1 hour at 300 °C followed by 30 min at 900 °C by SEM (a, d), FTIR (b, e), XRD (c, f), TEM (g, h) and SAED (i). a) cross-section SEM of mesoporous $Al_2(CO_3)_3$ film b) infrared-spectrum of the precursor complex calcined at 300 °C recorded in transmission, c) gracing incident XRD analysis of amorphous $Al_2(CO_3)_3$ (i). d) SEM top-view image of Al_2O_3 (ii), e) FTIR spectrum of dried precursor complex calcined by procedures (i)+(ii), f) XRD analysis of Al_2O_3 (ii) with reflection positions corresponding to Al_2O_3 in γ-Al_2O_3 structure (PDF-No. 00-050-0741). Figures g), h) and i) present electron microscopy analysis of (ii) Al_2O_3 by g) bright-field TEM, h) high-resolution TEM and i) selected-area electron diffraction SAED (indexing: γ-Al_2O_3 structure, PDF-No. 00-050-0741).

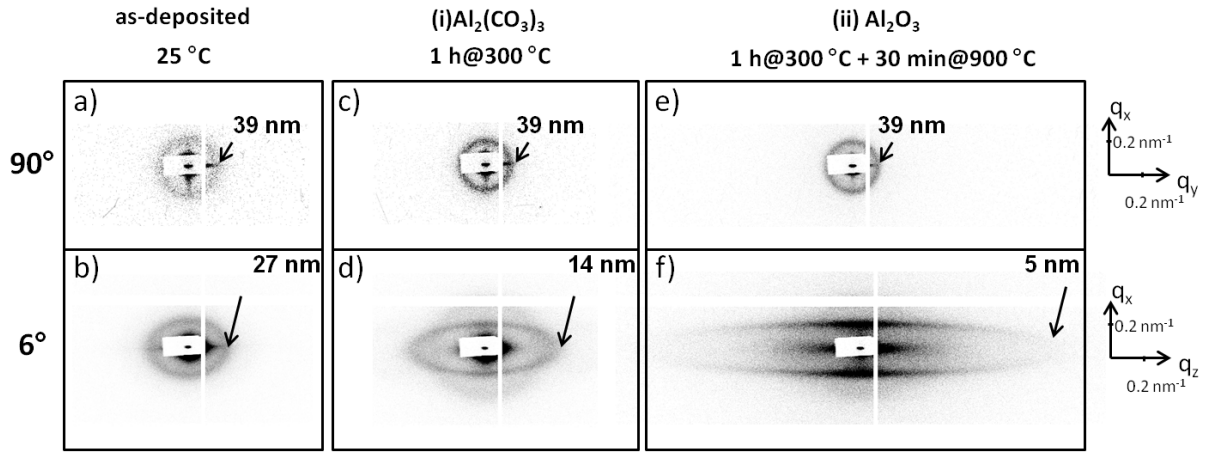

Figure 4.7.: 2D-SAXS pattern of films deposited from solutions with the complex of aluminium nitrate and citric acid as well as micelles of the polymer template PEO_{213}-PB_{184}-PEO_{213} after different thermal treatments. From left to right: (a, b) as-deposited, (c, d) aluminium carbonate (i) calcined for 1 hour at 300 °C and (e, f) aluminium oxide (ii) calcined for 1 hour at 300 °C followed by 30 min at 900 °C. Samples were analysed by SAXS with two different incident angles of the X-ray beam of 90° (upper panel) and of 6° (lower panel) relative to the substrate surface (linear intensity scale for a-f).

incident angles of 90° (a/c/e) and of 6° (b/d/f) relative to the substrate. The 2D-SAXS pattern (a) recorded at 90° for the as-deposited film features an isotropic ring corresponding to a d-spacing of 39 nm. Both, d-spacing and isotropic ring are preserved upon heat treatment at 300 °C (Figure 4.7c) and during further calcination at 900 °C (Figure 4.7e). The SAXS pattern recorded at an incident angle of 6° elliptical shaped rings indicate an elliptical deformation of the pores with a periodical distance perpendicular to the substrate decreases from 27 nm (as-deposited) to 14 nm (carbonate) and 5 nm (oxide) (Figure 4.7b/d/f).

In summary, employing the material precursor formed by complexing aluminium nitrate with citric acid enables the synthesis of micelle templated aluminium carbonate for the first time and an alternative route to ordered mesoporous aluminium oxide layers. The pore structure of aluminium carbonate is preserved upon transformation into the nanocrystalline aluminium oxide at higher temperatures. Further investigations should employ mesoporous Al_2O_3 as support material for a model system to examine the influence of mass transport during catalysis.

4.5. Zinc Carbonate and Zinc Oxide

In terms of applicability and nanostructures ZnO is one of the most versatile material. The industrial and scientific importance is not only obivious as cooper doped catalyst in industrial methanol synthesis,[137] but especially by its unique combination of electronic, optoelectronic and piezoelectric properties.[138] Employing nanostructured ZnO in form of nano rods or wires, the material can act as a piezoelectric power source for self-powered nanodevice[139–141] or even as cancer sensor.[140] Although, zinc oxide is known for versatile nanostructures (e.g. rods, wires, belts, helixes, cages, spheres, spirals),[142] a synthesis of mesoporous ZnO layers with polymer template porosity is not reported so far. Moreover, soft-templated mesoporous zinc carbonate was never reported before. In this section the synthesis and characterisation of mesoporous $ZnCO_3$ and ZnO is presented.

Mesoporous $ZnCO_3$ and ZnO layers were synthesized by dip coating and subsequent calcination. The dip-coating solution was prepared by co-dissolving the joined powders of citric acid, $Zn(NO_3)_2{\cdot}6H_2O$ and PEO_{213}-PB_{184}-PEO_{213} polymer template in a 1:1 Water-Ethanol mixture. The layers were synthesized by dip-coating on a silicon substrate and subsequent calcination.

According to thermo gravimetric analysis results (see section 4.2) the calcination temperatures and times are selected to 1 hour at 250 °C (i) to synthesize the mesoporous zinc carbonate and thereafter for 25 min at 400 °C (ii) to obtain mesoporous oxide.

Figure 4.8 presents for the Zn-based materials templated with PEO_{213}-PB_{184}-PEO_{213} (i) calcined for 1 hour at 250 °C the analysis of $ZnCO_3$ by SEM (a), FTIR (b), XRD (c) as well as for the corresponding ZnO (ii) calcined additionally at 400 °C for 25 min SEM (d), FTIR (e), XRD (f), TEM (g, h) and SAED (i).

The cross section SEM image (Figure 4.8a) of sample (i) indicates a homogenous film with a film thickness of 1100 nm. The film is completely penetrated by mesopores with slightly elliptical shapes 21 nm x 19 nm in size. The appearance of the walls is smooth and unstructured; no crystallites can be distinguished. This is in agreement with the XRD analysis (Figure 4.8c) of the sample which shows only reflections that can be attributed to silicon substrate and no indication of a crystalline Zn-containing phase. FTIR spectra (Figure 4.8b) recorded on corresponding powder samples feature two intense signals corresponding to symmetric (1384 cm^{-1}) and asymmetric (1583 cm^{-1}) vibrations of zinc carbonate.[143] Only negligible contributions at wave numbers indicative of ZnO (e.g. 577 cm^{-1}). Kr-physisorption indicates a BET surface area of 86 m^2/g. Hence, combined analytical data indicate the successful synthesis of micelle-templated zinc carbonate comprising amorphous walls and interconnected accessible mesopores.

After further calcination (ii) at 400 °C for 25 min the FTIR spectrum (Figure 4.8e) shows a strong signal at 577 cm^{-1} indicative of ZnO,[143] whereas only small bands assigned to carbonate are retained. The X-ray diffractogram of the layered sample (Figure 4.8f) features broad reflections at positions of 2θ = 31.7° (100), 34.5° (002), 36.0° (101), 62.9° (103) and 67.8° (112). These reflections can be assigned to ZnO in hexagonal zincite structure (PDF-No. 00-036-1451) with an average crystallite size of 7 nm (Scherrer equation). Hence, calcination at 400 °C transforms the amorphous carbonate into nanocrystalline ZnO. The corresponding top-view SEM image (Figure 4.8d) indicates that films remain homogeneous and macroscopically crack-free. The films are completely penetrated by mesopores with 22 nm in diameter. The pores are locally ordered and open toward the outer film surface. TEM analysis (Figure 4.8g) confirms the presence of templated mesopores throughout the sample volume. High-resolution TEM (Figure 4.8h) indicates crystallites and lattice fringes, which confirm that the pore walls are crystalline. Furthermore, SAED analysis (Figure 4.8i) shows isotropic diffraction rings with ring positions that match the reflections of hexagonal zincite structure (PDF-No. 00-036-1451). In comparison of the bright-field and dark-field TEM image (Figure A.9e and f)) show equally sized bright spots corresponding to wall crystallites. The crystallites have a narrow size distribution with an average size of 7 nm. This is in good aggrement with the XRD results.

Hence, calcination at 400 °C for 25 min transforms the amorphous carbonate into nanocrystalline ZnO with a templated mesoporous structure. However, the Kr-BET surface area of the mesoporous ZnO amounts to 250 m^2/g, which is 3 times higher than that for the corresponding $ZnCO_3$. This increase in surface area can be attributed to additional microporosity present in the nanocrystalline pore walls of ZnO, whereas the pore walls of amorphous $ZnCO_3$ appear to be rather dense.

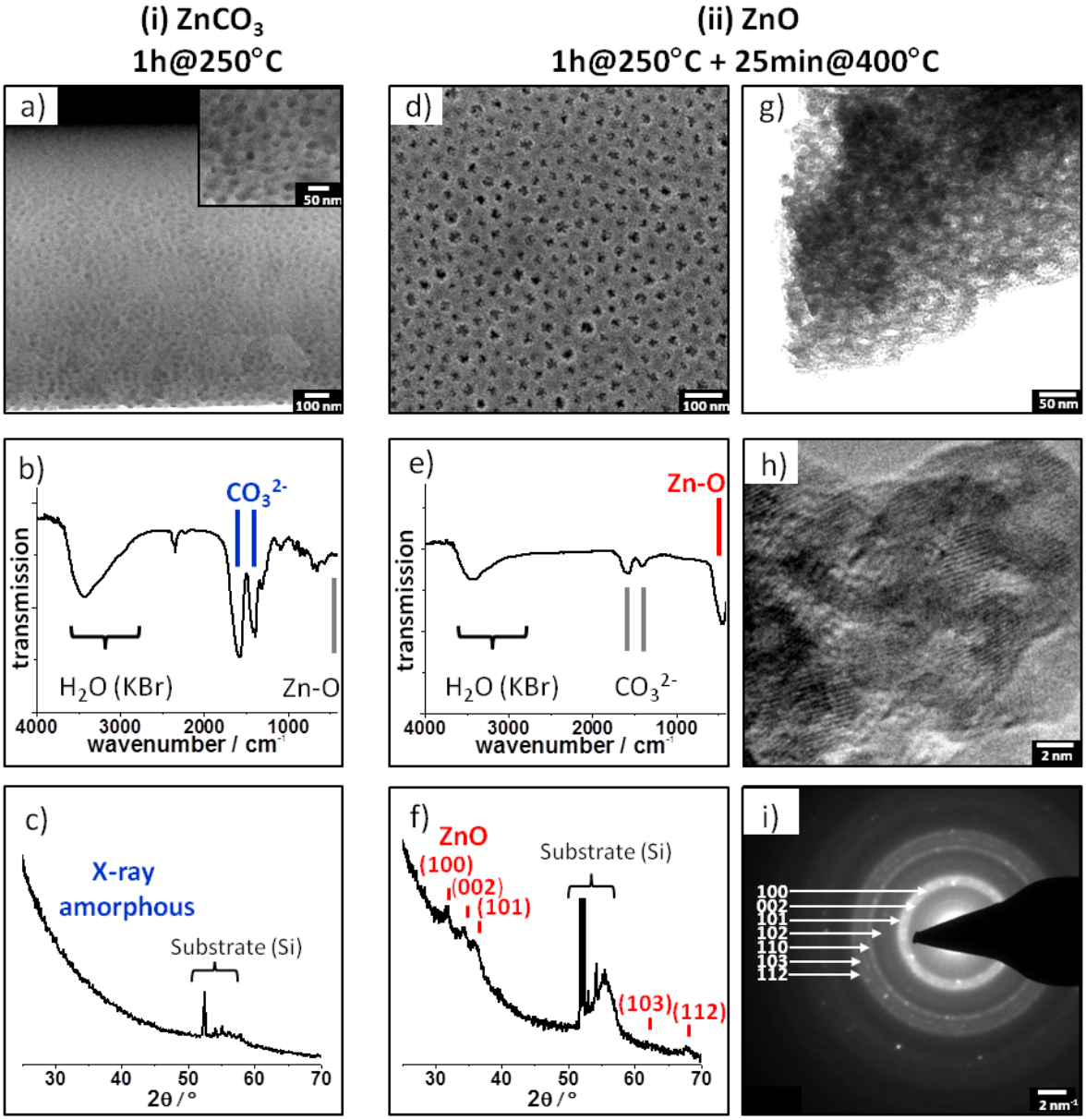

Figure 4.8.: Analysis of (i) mesoporous $ZnCO_3$ calcined 1 hour at 250 °C and (ii) of mesoporous ZnO calcined for 1 hour at 250 °C followed by 25 min at 400 °C by SEM (a, d), FTIR (b, e), XRD (c, f), TEM (g, h) and SAED (i). a) cross-section SEM of mesoporous $ZnCO_3$ film with inset at higher magnification, b) infrared-spectrum of the precursor complex calcined at 250 °C recorded in transmission, c) gracing incident XRD analysis of amorphous $ZnCO_3$ (i). d) SEM top-view image of ZnO (ii), e) FTIR spectrum of dried precursor complex calcined by procedures (i)+(ii), f) XRD analysis of ZnO (ii) with reflection positions corresponding to ZnO in hexagonal zincite structure (PDF-No. 00-036-1451). Figures g), h) and i) present electron microscopy analysis of (ii) ZnO by g) bright-field TEM, h) high-resolution TEM and i) selected-area electron diffraction SAED (indexing: hexagonal zincite structure, PDF-No. 00-036-1451).

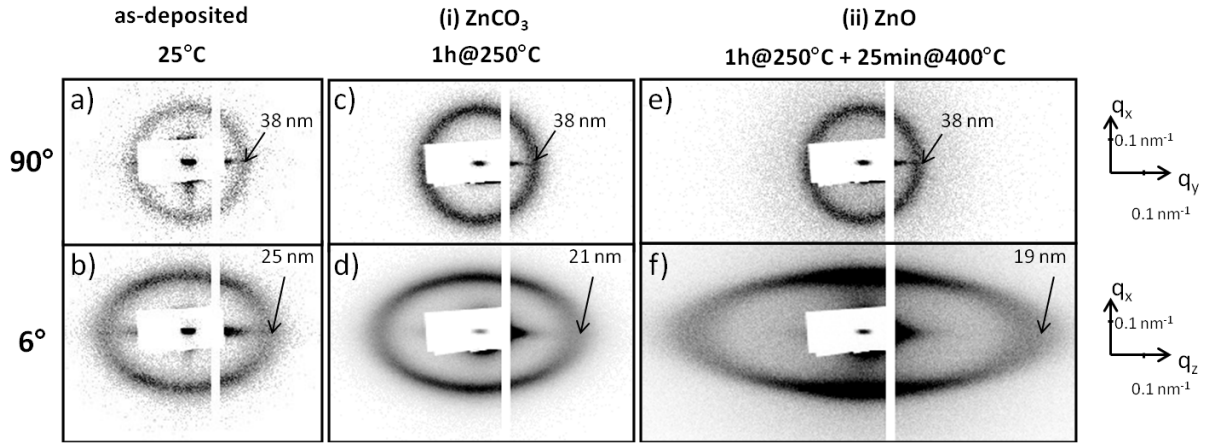

Figure 4.9.: 2D-SAXS pattern of films deposited from solutions with the complex of zinc nitrate and citric acid as well as micelles of the polymer template PEO_{213}-PB_{184}-PEO_{213} after different thermal treatments. From left to right: (a, b) as-deposited, (c, d) zinc carbonate (i) calcined for 1 hour at 250 °C and (e, f) zinc oxide (ii) calcined for 1 hour at 250 °C followed by 25 min at 400 °C. Samples were analysed by SAXS with two different incident angles of the X-ray beam of 90° (upper panel) and of 6° (lower panel) relative to the substrate surface (linear intensity scale).

The evolution of the pore structure was analysed after deposition and after different thermal treatments of deposited films. Mesoscale order in Zn-containing films was analysed after different thermal treatments of deposited films. Figure 4.9 details the evolution of order from deposited micelles (a, b) to (i) porous $ZnCO_3$ (c, d) and (ii) ZnO (e, f) as indicated by 2D-SAXS recorded in transmission at beam incident angles of 90° (a/c/e) and of 6° (b/d/f) relative to the substrate. The 2D-SAXS pattern (a) recorded at 90° for the as-deposited film features an isotropic ring corresponding to a d-spacing of 38 nm. Both, d-spacing and isotropic ring are preserved upon heat treatment at 250 °C (Figure 4.9c) and during further calcination at 400 °C (Figure 4.9e). In contrast, all 2D-SAXS patterns recorded at low incident angle of 6° (Figure 4.9b, d, f) show diffraction rings with elliptical shape. Such diffraction patterns have been reported also for conventional EISA-based syntheses, where the pore axis that is oriented perpendicular to the substrate progressively shrinks during thermal treatments. This deformation is caused by a loss of film volume resulting in homogeneous anisotropic film shrinkage upon drying as well as calcination. Hence, the d-spacing perpendicular to the substrate decreases in the studied Zn-containing films from 25 nm (as deposited) to 21 nm (carbonate i) and 19 nm (oxide ii) (Figure 4.9b/d/f). However, the d-spacing parallel to the substrate of 38 nm remains unchanged (Figure 4.9a/c/e). This observation confirms that film shrinkage is anisotropic and restricted to the direction perpendicular to the substrate. Moreover, the observed ellipsoidal 2D-SAXS patterns (Figure 4.9b/d/f) indicate also a certain degree of lattice distortions in the cubic mesostructure. Thus, SAXS analysis confirms that the deposited micelles and precursor complex form a locally ordered mesophase, and that corresponding pore order is preserved also during carbonate formation, template removal and transition into mesoporous zinc oxide.

In summary, employing the material precursor formed by complexing zinc nitrate with citric acid allows the synthesis of micelle templated zinc carbonate and zinc oxide for the first time. The ordered mesoporous zinc carbonate appears X-ray amorphous and shows a periodical order of elliptical shaped pores. The pore structure is preserved upon transformation into the nanocrystalline zinc oxide at higher temperatures. Further characterisation of mesoporous ZnO should include testing of the conductivity and optical properties to investigate the applicability as transparent electrode for photo catalysis or in photo voltaic devices.

4.6. Cobalt Carbonate and Cobalt Oxide

Nanostructured cobalt-based oxides are promising materials for electrodes in super-capacitors[34,35] and in lithium-ion batteries[144,145] with superior charging rates.[146] Moreover, they represent very active catalysts for the oxygen evolution reaction in electrochemical water splitting[147] and the oxygen reduction reaction in fuel cells.[148]

However, micelle-templated synthesis of Co_3O_4 has not been reported so far. In this section the synthesis and characterisation of $Co(CO_3)_x$ films and mesoporous Co_3O_4 is presented.

Briefly, cobalt containing films were synthesized by dip coating. The dip-coating solution was prepared by co-dissolving the joined powders of $Co(NO_3)_2{\cdot}6H_2O$, citric acid and PEO_{213}-PB_{184}-PEO_{213} polymer template in a 1:1 water-ethanol mixture. The layers were synthesized by dip-coating on a silicon substrate and subsequent calcination. According to thermo gravimetric analysis results (see section 4.2) the calcination temperatures and times are selected to 1 hour at 200 °C (i) to synthesize the cobalt carbonate and thereafter 20 min at 300 °C (ii) to obtain mesoporous cobalt oxide.

Figure 4.10 presents for the Co-based materials templated with PEO_{213}-PB_{184}-PEO_{213} (i) calcined for 1 hour at 200 °C the analysis of $Co(CO_3)_x$ by SEM (a), FTIR (b), XRD (c) as well as for the corresponding Co_3O_4 (ii) calcined with additional 300 °C for 20 min SEM (d), FTIR (e), XRD (f), TEM (g, h) and SAED (i).

FTIR analysis of the film calcined at 200 °C (Figure 4.10b) shows asymmetric (1585 cm^{-1}) and symmetric (1392 cm^{-1}) stretching vibrations that can be assigned to carbonate.[149] The formed film is amorphous according to XRD (Figure 4.10c). Unfortunately, electron microscopy imaging of the film (Figure 4.10)a) failed due to its instability in the electron beam. Moreover, the film's surface area was too low to be detected by Kr-physisorption analysis. Both observations suggest that the polymer template is still present in the film. Hence, micelle-structured cobalt carbonate is formed during calcination at 200 °C, yet its pore structure is blocked by the remaining template micelles. This effect is in complete agreement with the TG analysis of precursor complex and template (see section 4.2) and demonstrates a limitation of the proposed synthesis strategy in its present form.

Nevertheless, analysis of the film calcined in addition at (ii) 300 °C indicates that the mesoporous oxide can still be formed. Top-view SEM images of the film show spherical pores of about 22 nm in diameter (Figure 4.10d). TEM analysis confirms that the film is fully porous (Figure 4.10g). High-resolution TEM (Figure 4.10h) indicates crystallites and lattice fringes, which confirms that the pore walls are crystalline. Dark-field TEM image (Figure A.9) shows bright spots corresponding to nanocrystallites with a narrow size distribution around 6 nm. FTIR spectra (Figure 4.10e) contain strong bands indicative of cobalt oxide formation, i.e. Co-O vibrations at 663 cm^{-1} and 570 cm^{-1},[150] whereas only small signals for carbonates remained (Figure 4.10e). The corresponding XRD pattern (Figure 4.10f) reveals numerous reflections that match with the reported phase of crystalline Co_3O_4 in spinel structure with $2\theta = 31.1°$ (220), 36.9° (311), 44.8° (400), 55.7° (422), 59.3° (511), 65.3° (440)) (PDF 00-042-1467). The crystallite size estimated via Scherrer-equation (311) amounts to 7 nm. SAED analysis (Figure 4.10i) evidences numerous diffractions rings that confirm the samples crystallinity as well as the assignment of the crystalline spinel phase. The samples surface area amounts to about 257 m^2/g (Kr-physisorption). Hence, calcination (ii) of the micelle-structured (non-porous) cobalt carbonate at 300 °C forms a nanocrystalline Co_3O_4 film with spinel structure and the desired open templated porosity.

The mesoscale order in Co-containing films was analysed after deposition and after different thermal treatments of deposited films. Figure 4.11 details the evolution of order from as-deposited films (a, b) to (i) $Co(CO_3)_x$ (c, d) and (ii) Co_3O_4 (e, f) as indicated by 2D-SAXS recorded in transmission at beam incident angles of 90° (a/c/e) and of 6° (b/d/f) relative to the substrate. The 2D-SAXS patterns of the as-deposited film feature an isotropic ring in 90° and an elliptical shaped ring in 6° configuration corresponding to periodical order of 37 nm parallel to the substrate

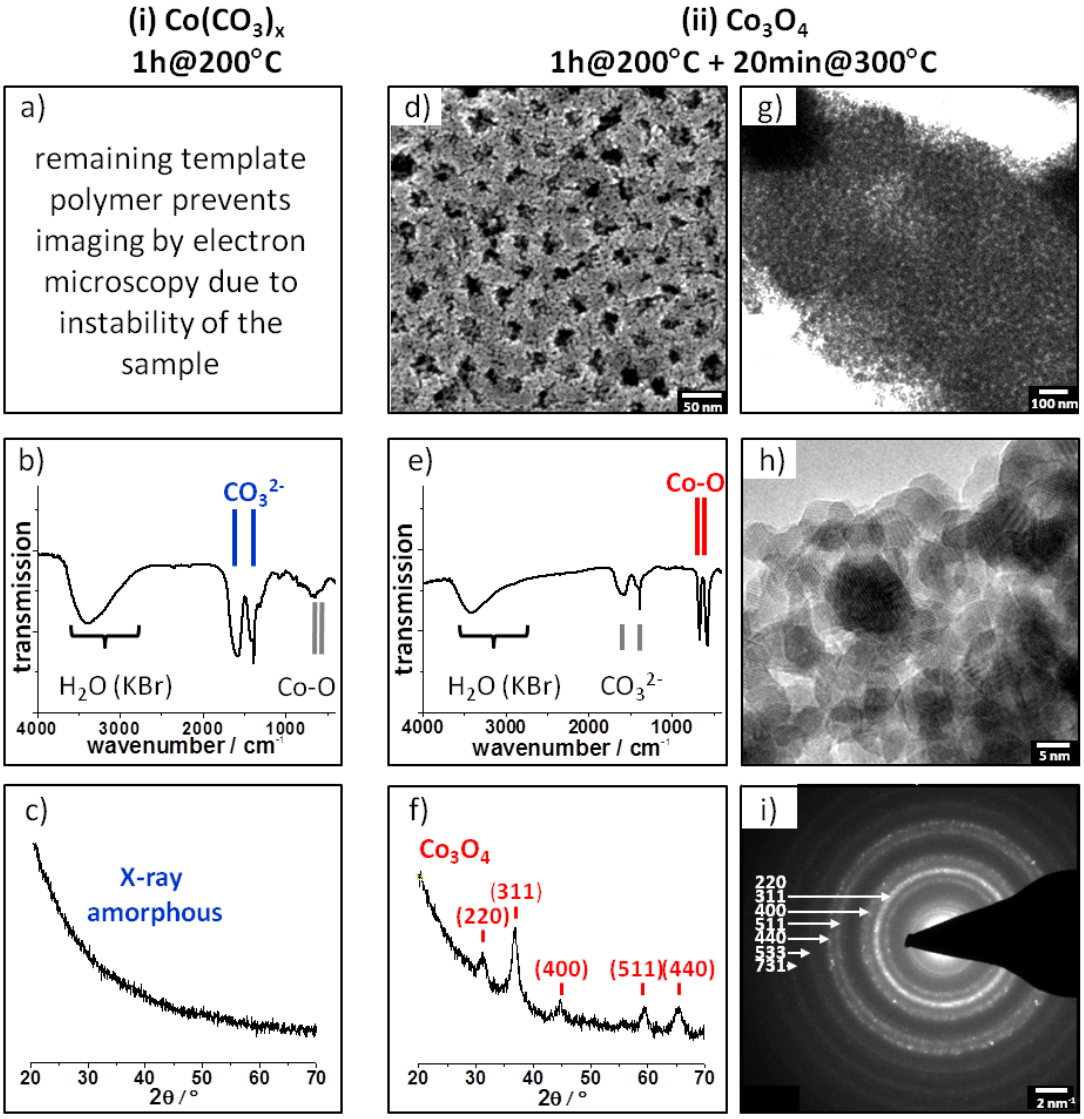

Figure 4.10.: Analysis of (i) micelle structured $Co(CO_3)_x$ calcined 1 hour at 200 °C and (ii) of mesoporous Co_3O_4 calcined for 1 hour at 200 °C followed by 20 min at 300 °C by SEM (a, d), FTIR (b, e), XRD (c, f), TEM (g, h) and SAED (i). a) SEM of $Co(CO_3)_x$ film fail because of instability in electron beam b) infrared-spectrum of the precursor complex calcined at 200°C recorded in transmission, c) gracing incident XRD analysis of amorphous $Co(CO_3)_x$ (i). d) SEM top-view image of Co_3O_4 (ii), e) FTIR spectrum of dried precursor complex calcined by procedure (ii), f) XRD analysis of Co_3O_4 (ii) with reflection positions corresponding to Co_3O_4 in spinel structure (PDF-No. 00-042-1467). Figures g), h) and i) present electron microscopy analysis of Co_3O_4 (ii) by g) bright-field TEM, h) high-resolution TEM and i) selected-area electron diffraction SAED (indexing: spinel Co_3O_4 , PDF-No. 00-042-1467).

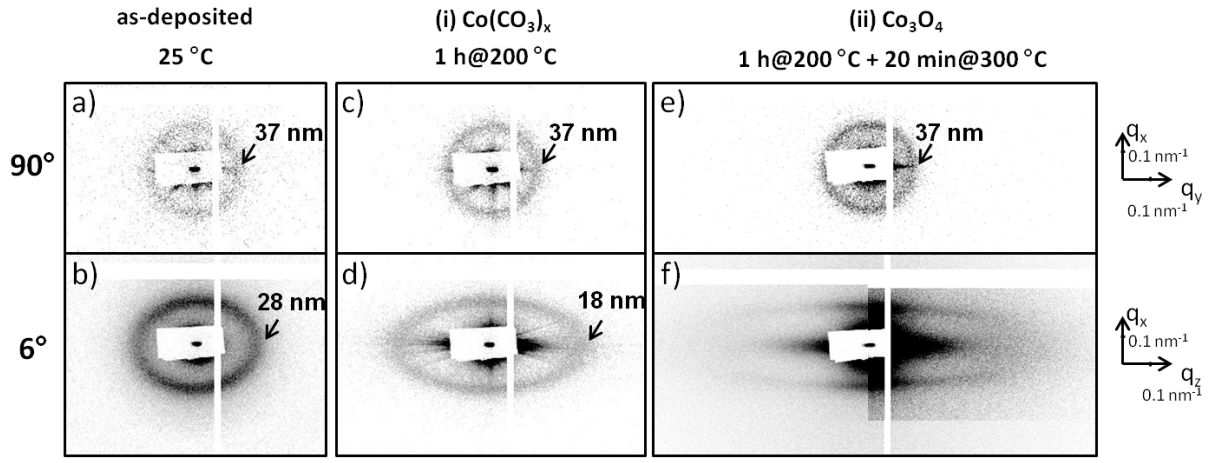

Figure 4.11.: 2D-SAXS pattern of films deposited from solutions with the complex of cobalt nitrate and citric acid as well as micelles of the polymer template PEO_{213}-PB_{184}-PEO_{213} after different thermal treatments. From left to right: (a, b) as-deposited, (c, d) cobalt carbonate (i) calcined for 1 hour at 200 °C and (e, f) cobalt oxide (ii) calcined for 1 hour at 200 °C followed by 20 min at 300 °C. Samples were analysed by SAXS with two different incident angles of the X-ray beam of 90° (upper panel) and of 6° (lower panel) relative to the substrate surface. Linear intensity scale and inset with logarithmic (f).

and 28 nm perpendicular to the substrate, respectively. Thus, the polymer micelles mesoscopically structure the deposited film.

SAXS analysis reveals a diffraction ring for the sample calcined for 1 hour at 200 °C (Figure 4.11c and d) with a d-spacing of 37 nm parallel and 18 nm perpendicular to the substrate, both indicate the presence of an ordered mesostructure. Although, the d-spacing of 37 nm parallel to the substrate (Figure 4.11e) is preserved upon heat treatment at 300 °C (i) as indicated by the isotropical ring, the 2D-SAXS pattern recorded at 6° incident angle (Figure 4.11f) the elliptical shape is no longer closed, which suggests a restructuring of the mesopore network perpendicular to the substrate due to growth of Co_3O_4 crystallites.

In this section the synthesis of micelle structured $Co(CO_3)_x$ and Co_3O_4 layers was demonstrated. Unfortunately, the cobalt carbonate is not accessible in mesoporous form because the decomposition of the carbonate occurs at lower temperatures as the template decomposition. However, cobalt carbonate with open mesoporosity should become accessible when the PEO-PB-PEO template is removed by alternative (nonthermal) methods or when alternative templates with lower decomposition temperature are employed. However, the synthesis of mesoporous cobalt oxide with nanocrystalline walls and templated mesopores was successful. Hence, applying citric acid complexed cobalt nitrate as material precursor enables the synthesis of templated mesoporous Co_3O_4 for the first time. Further investigations should include the electrocatalytic testing of Co_3O_4 in oxygen evolving reaction in comparison with a not templated sample to investigate the influence on the activity and overpotenital. A variation of the pore size can give insights in mass transport properties of the different pore systems.

4.7. Variation of the Template

The major advantage of EISA based templating techniques is a facile control of pore size, shape and wall thickness by employing template polymers with different physicochemical properties, molar weights or concentrations.[77,66] The following paragraph will demonstrate that the synthesis strategy employing an intermediate carbonate is versatile as the commonly applied EISA approaches by synthesizing micelle templated ZnO with different sized pores by employing PEO-PB-PEO polymer templates in different molecular sizes (PEO_{65}-PB_{59}-PEO_{65}, PEO_{104}-PB_{92}-PEO_{104} and

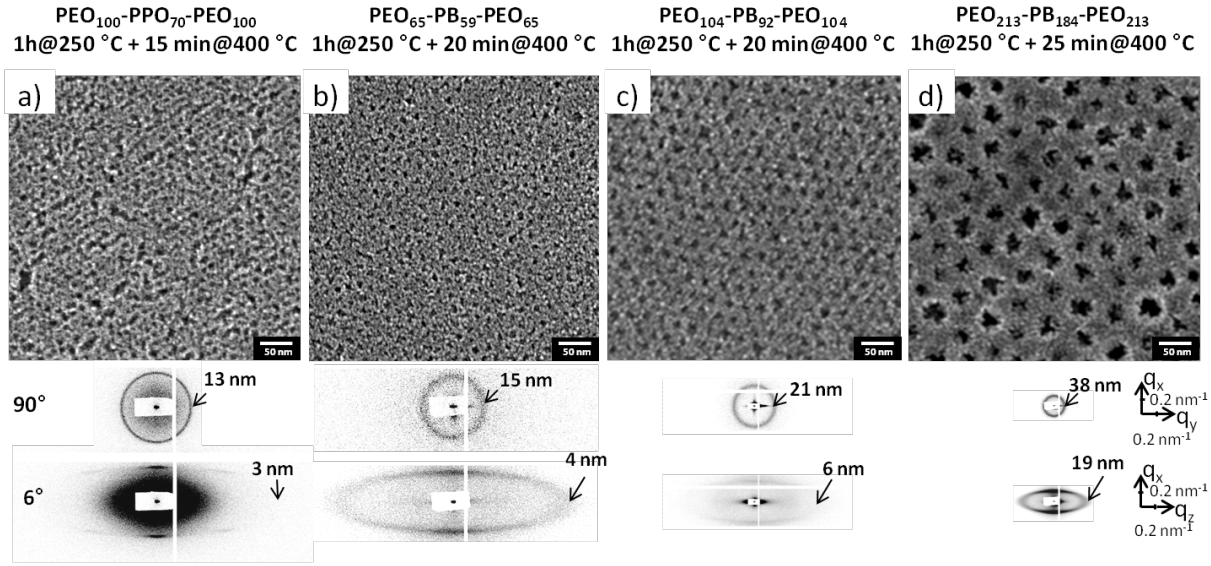

Figure 4.12.: SEM top-view images and corresponding SAXS measurments obtained in 90° and 6° configuration of ZnO templated with a) PEO_{100}-PPO_{70}-PEO_{100}, b) PEO_{65}-PB_{59}-PEO_{65}, c) PEO_{104}-PB_{92}-PEO_{104} and d) PEO_{213}-PB_{184}-PEO_{213}.

PEO_{213}-PB_{184}-PEO_{213}) as well as the commercially available triblock-copolymer Pluronic F127 with the structure PEO_{100}-PPO_{70}-PEO_{100}. Moreover, this chapter will demonstrate the flexibility of the synthesis strategy by synthesizing ZnO with two pore sizes by dual templating with the smallest PEO_{65}-PB_{59}-PEO_{65} and largest PEO_{213}-PB_{184}-PEO_{213}. Mesoporous ZnO was synthesized by calcination of the intermediate carbonate with adjusted time at 400 °C for optimized crystallite sizes for the different pore sizes.

Figure 4.12 shows SEM top-view images of ZnO films templated with a) PEO_{100}-PPO_{70}-PEO_{100}, b) PEO_{65}-PB_{59}-PEO_{65}, c) PEO_{104}-PB_{92}-PEO_{104} and d) PEO_{213}-PB_{184}-PEO_{213} accompanied by their corresponding 2D-SAXS patterns recorded in transmission at beam incident angles of 90° and 6° with respect to the substrate.

Figure 4.12 panel a) shows SEM top-view image of a ZnO film templated with PEO_{100}-PPO_{70}-PEO_{100} (Pluronic F127) and calcined for 1 hour at 250 °C followed by 15 min at 400 °C indicating nanocrystalline pore walls and spherical pores with a mean pore diameter of 6 nm. The SAXS measurement recorded in 90° transmission mode shows a diffraction ring corresponding to a periodical distance of 13 nm. The SAXS pattern obtained at 6° incident angle of the beam shows individual spots distributed on an ellipse indicating a high degree of pore ordering. The observed diffraction pattern indicates the formation of a body-centered-cubic mesophase[59] with a periodical order of 3 nm perpendicular to the substrate. Ortel et al. reported slightly higher pore diameters of 9 - 11 nm and d-spacings of 13 - 15 nm parallel to the substrate for TiO_2 films templated with F127.[66]

Figure 4.12 panel b) shows SEM top-view image of a ZnO film templated with PEO_{65}-PB_{59}-PEO_{65} polymer and calcined for 1 hour at 250 °C followed by 20 min at 400 °C indicating nanocrystalline pore walls and spherical pores with a pore diameter of 8 nm. The 2D-SAXS pattern recorded in 90° transmission mode shows an isotropic ring corresponding to a periodical distance of 15 nm parallel to the substrate. The ellipsoidal shaped SAXS pattern recorded at 6° incident angle indicating a d-spacing perpendicular to the substrate to 4 nm. Pore size and order is in good agreement with the literature value of 8 nm pore diameter , although the periodical distance obtained in 90° configuration is slightly smaller elucidated for TiO_2 templated with the same polymer (12 nm).[66]

Figure 4.12 panel c) shows SEM top-view images of a ZnO films templated with PEO_{104}-PB_{92}-

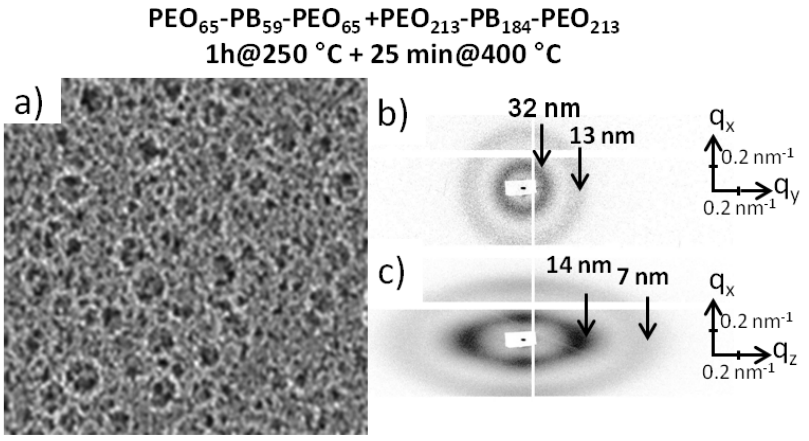

Figure 4.13.: ZnO with bimodal pore sizes templated with a combination of PEO_{65}-PB_{59}-PEO_{65} and PEO_{213}-PB_{184}-PEO_{213} (mass ratio 2:1) showing a) SEM top-view images as well as corresponding SAXS measurments obtained in b) 90° and c) 6° configuration of the incident beam relative to the substrate

PEO_{104} polymer and calcined for 1 hour at 250 °C followed by 20 min at 400 °C indicating spherical pores with a diameter of 15 nm. The SAXS measurement recorded in 90° transmission mode shows a diffraction ring corresponding to a periodical distance of 21 nm. The elliptical shape of the 2D-SAXS pattern obtained at 6° incident angle is no longer closed, which suggests a restructuring of the mesopore network perpendicular to the substrate. Ortel et al. reported slightly smaller values with a pore diameter of 12 nm and d-spacing of 16 nm parallel for TiO_2 films templated with PEO_{104}-PB_{92}-PEO_{104}.[66]

Figure 4.12 panel d) shows SEM top-view image of a ZnO film templated with EO_{213}-PB_{184}-PEO_{213} polymer and calcined for 1 hour at 250 °C followed by 25 min at 400 °C indicating nanocrystalline pore walls and spherical pores with a pore diameter of 22 nm. The 2D-SAXS pattern recorded at 90° configuration shows an isotropic ring corresponding to a periodical distance of 38 nm parallel to the substrate. The ellipsoidal shaped SAXS pattern recorded at 6° incident angle indicates a d-spacing of 19 nm perpendicular to the substrate . Pore size and ordering behaviour is in good agreement with the literature value of 21.1 nm pore diameter, although the periodical distance is smaller for TiO_2 templated with the same polymer (28.1 nm).[66]

However, the pore size can be controlled by the template size between 6 - 22 nm. The d-spacing of the pores changes in the same regime. In addition, the synthesis strategy is also applicable to commercial block-copolymers and is not limited to templates with a high hydrophilic-hydrophobic contrast like PEO-PB-PEO. The pore order in the resulting films depends on the hydrophilic-hydrophobic-contrast and the applied synthesis procedure and is not determined by the type of oxide precursor.

Moreover, combining PEO_{65}-PB_{59}-PEO_{65} and PEO_{213}-PB_{184}-PEO_{213} in a mass ratio of 2:1 in one deposition solution enables dual templating of ZnO.

Figure 4.13 shows a top-view SEM image of a ZnO film with bimodale pore size with pore diameters of 9 and 22 nm. While the smaller pores are well ordered, the larger 22 nm pores seem to be randomly distributed. This is confirmed by SAXS measurements (see Figure 4.13b) showing 2 isotropical rings recorded in 90° configuration. The larger ring corresponds to a d-spacing of 13 nm originated from the 9 nm pores. In contrast, the smaller diffraction ring corresponds to the average distance of the 22 nm pores and corresponds to a value of 32 nm. The SAXS pattern recorded in 6° transmission mode (see Figure 4.13c) shows two elliptical shaped rings. The larger ring corresponds to the d-spacing of 7 nm and the smaller ring to a periodical distance of 14 nm perpendicular to the substrate indicate a shrinkage of the mesostructure.

In comparison to the film templated only with PEO_{65}-PB_{59}-PEO_{65} the shrinkage of the bimodal ZnO is drastically reduced from 74% shrinkage in the monomodal film to only 46% shrinkage in

the bimodal film. In contrast, the pores templated with PEO_{213}-PB_{184}-PEO_{213} show a stronger shrinkage of bimodal ZnO (56%) compared to the monomodal sample (50%). Hence, the volume loss during calcination of the film is mostly compensated by shrinkage of the larger pores.

In summary, the pore size of ZnO can be controlled by employing different sized templates. The pore sizes in ZnO can be varied in the range between 6 - 22 nm. The presented synthesis concept is not limited to polymer templates with high hydrophilic-hydrophobic contrast, but also applicable to the commercially available Pluronic F127 polymer. Moreover, also dual templated ZnO layers are accessible by employing different sized templates in the same dipcoating solution. Hence, the new synthesis concept is as versatile as common EISA approaches.

4.8. Discussion

In this thesis a new approach for the synthesis of micelle-templated oxides and carbonates of magnesium, zinc, cobalt and aluminium is presented. The method employs an unique precursor to overcome limitations of classical EISA-based syntheses, i.e. complexes formed from citric acid and metal nitrates (see section 2.3.2). 5 criteria must be fulfilled for a successful synthesis of micelle templated metal carbonates and oxides using this precursor.

At first, the citric acid and the metal nitrate have to form a stable and soluble chemical complex in solution (criterion **1**). The ability of citric acid to form complexes with the nitrates of Mg, Al, Zn and Co was, therefore, investigated by electron spray ionisation mass spectrometry (ESI-MS) of the complex solutions. The recorded mass spectra evidence the presence of the metal complexes with citric acid in different metal (M) to ligand (L) stoichiometries (ML, M_2L, ML_2, M_2L_2). A fixed stoichiometry cannot be clearly distinguished from the present data. Possibly, the material precursor is not present as a defined molecule, but in form of a network formed by metal nitrates cross linked by citric acid. The present data evidence clearly the interaction between metal ions and ligand.

Detailed knowledge about the ratio of metal ion to ligand as well as the structural appearance of the complex could be analysed by single crystal X-ray diffraction. Unfortunately, all attempts to grow single crystals failed so far. However, the tendency of excessive crystallisation of salt-type precursors (see section 2.3.2) during drying often prevents the formation of the required structured mesophase. Therefore, the synthesis of mesoporous oxide fails when salt precursors are employed. The suppressed crystallisation of the the citric acid complexes with metal nitrate prevent the loss of the mesostructure. Hence, this advantageous property of the precursor complexe enables the formation of a micelle structured mesophase (criterion **2**) upon film coating and drying. SAXS measurements evidence a periodical order of micelles in as-deposited films prepared with the Mg, Al, Zn and Co containing precursors. The difference of d-spacings parallel (37 - 39 nm) and perpendicular (25 - 28 nm) to the substrate is negligible. However, the periodical distance is significantly increased compared to TiO_2 templated with PEO_{213}-PB_{184}-PEO_{213} polymer.[66] The 2D-scattering patterns recorded on all films at low incident angles (Mg:13°; Al, Zn, Co: 6°) contain rings of elliptical shape. The shape results from film shrinkage perpendicular to the substrate and implies deformation of the pore system upon drying and calcination. Such shrinkage is typically observed for micelle-templated oxide films and leads to elliptical deformation of the pore shapes.[77] However, the precursor complexes reliably self-assemble with amiphiphilic copolymers to a structured mesophase.

After the formation of the structured mesophase, the precursor must transform into a structural stable metal carbonate (criterion **3**). The temperatures for this transformation were deduced from thermogravimetric analysis (TG) of the dried precursors. The TG-curves recorded from Mg, Al, Zn and Co containing precursors indicate a starting transformation of the precursor into carbonate at temperatures between 80 - 160 °C. Although, the principle shapes of the TG-curves are similar, the thermal stability and the decomposition temperature of carbonates vary depending on the metals. In comparison of the employed metal nitrates, magnesium forms the most thermal

stable carbonate (T = 425 °C) followed by Al (T = 320 °C) and Zn (T = 310 °C). Cobalt carbonate decomposes at the lowest temperature (T = 245 °C). This temperature is lower than the decomposition temperature of the polymer template (T = 250 °C). Therefore, the template cannot be thermally removed from cobalt carbonate without decomposition of the carbonate. Hence, mesoporous cobalt carbonate is not accessible in mesoporous form applying this synthesis strategy. However, cobalt carbonate with open mesoporosity should become accessible when the PEO-PB-PEO template is removed by alternative methods (e.g. plasma treatment) or when templates with lower decomposition temperature are employed, alternatively.

In the case of Mg, Al and Zn the template can be removed while the carbonates are stable. Therefore, magnesium, aluminium and zinc precursors can be transformed into mesoporous carbonates without mesopore collapse (criterion **4**) as evidenced by SAXS measurements. FTIR measurements exhibit two strong signals corresponding to carbonate vibrations. The BET surface of the mesoporous carbonates area amount to 44 to 86 m^2/g. This value is slightly smaller than the surface area typically observed for micelle templated oxides ($\sim$100 - 250 m^2/g).[5] The reason for this is most likely the absence of microporosity. SEM images of Mg, Al and Zn carbonates indicate the smooth and unstructured appearance of the pore walls. The XRD measurements reveal the carbonates are obtained in amorphous form. The amorphous nature of the materials exhibits a great advantage compared to other EISA-based synthesis strategies, because the mesopores structure cannot be lost by extended growth of crystallites by sintering. Therefore, the film can be calcined for a long time at a specific temperature to remove the template completely.

In the next step the carbonate films can be transformed into the related mesoporous metal oxide films under the release of CO_2 (criterion **5**). XRD and SAED measurments indicate the Mg, Al, Zn and Co oxide are obtained as crystalline MgO in periclase structure, γ-Al_2O_3, hexagonal ZnO in zincite structure and Co_3O_4 in spinel structure. Therefore, the synthesis concept is not limited by the type of oxide crystal structure the carbonate is converted in.

The calcination time was chosen to be short to prevent collapse of the pore structure by sintering and to obtain nano crystallites with an average size between 5 - 7 nm (Scherrer equation). Hence, the mesoporous oxide layers consist of nanocrystalline walls.

The SAXS measurements confirm the preservation of the mesopore order for all oxide films, although magnesium and cobalt derived films show a restructuring of the pore network. The Kr-BET surface area amounts to values between 250 and 286 m^2/g and is, therefore, 3 to 5 times higher compared to the corresponding carbonates. This increase is originated most likely in microporosity of the oxide films.

In summary, employing this new strategy enables the synthesis of mesoporous carbonates of Mg, Al and Zn as well as nanocrystalline templated MgO, Al_2O_3, ZnO and Co_3O_4 for the first time. Besides the now available new application derivable from this materials, especially templated MgO can be used as model system in OCM catalysis to analyse the influence of the pore diameter on the C_2-selectivity.

5. MgO and Li@MgO Catalysts for Oxidative Coupling of Methane

One aim of this thesis is the elucidation of the role of the pore system in OCM catalysis. Section 4.3 presented a new synthesis approach for the preparation of MgO films with micelle-templated porosity. In this chapter the synthesis approach is transferred to obtain MgO powders with templated mesoporosity.

Section 5.1 presents the synthesis and chracterisation of the obtained MgO based powders. The catalytic data are decribed in section 5.2. Section 5.3 presents the material characterisation after catalysis. Finally, the results are discussed in section 5.4.

5.1. Synthesis and Characterisation

In this section, the synthesis and material characterisation of micelle structured MgO and Li@MgO powders are described. The employed procedure to synthesize the powders is based on the developed synthesis route to obtain ordered mesoporous MgO films presented in section 4.3.

The synthesis of MgO and Li@MgO powders is described in detail in section 3.3.1. Briefly, micelle-templated MgO was obtained by addition of $Mg(NO_3)_2{\cdot}6\ H_2O$ and citric acid to PEO_{213}-PB_{184}-PEO_{213} dissolved in ethanol followed by drying and calcination. Magnesium oxide with a lithium content of 0.1%wt was obtained by adding $LiNO_3$ to the solution. The resulting solution was dried on a plain ceramic dish at 50 °C under an air stream. The obtained transparent gel was heated with 5 K/min to 480 °C and kept there for 3 hours followed by an additional hour at 500 °C. For comparison, the untemplated MgO and Li@MgO was prepared without PEO_{213}-PB_{184}-PEO_{213} applying the same procedure as described before.

The resulting powders were analysed by SEM, XRD, SAXS and N_2-physisorption to obtain information about morphology, crystallinity, pore order and pore size distribution of the catalyst material. The lithium content of Li@MgO was additionally determined by ICP-OES.

Figure 5.1 presents a) SEM, b) XRD and c) SAXS of the templated magnesium oxide powders. Figure 5.1d compares the BJH derived pore size distributions of the templated and untemplated MgO powders. In addition, SEM images and XRD analysis of MgO and Li@MgO prepared with and without polymer template PEO_{213}-PB_{184}-PEO_{213}, respectively, are shown in Figure A.11.

The SEM image (Figure 5.1a) of the MgO shows dark spots corresponding to spherical pores with a size between 20 - 50 nm without apparent pore order. In comparison, the micelle-templated MgO films (see Figure 4.4d) obtained with the same polymer exhibit pores with a size of 20 nm and, therefore, are smaller than the pores obtained in the MgO powders. Whether the large pores are originated from templating or from gas evolution during calcination cannot be decided from the SEM image. The surface of the MgO powder consists of nanocrystallites.

XRD (Figure 5.1b) confirms the presence of crystalline MgO by showing diffraction signals at $2\theta = 36.8°$ (111), 42.8° (200), 62.2° (220), 74.7° (311) and 78.7° (222) corresponding only to MgO in periclase structure (PDF: 00-045-0946). The Scherrer equation indicates an average crystallite size of 17.0 nm for MgO. In comparison to the MgO films (see Figure 4.4f) with 5 nm crystallite size, the MgO powder has a significantly larger crystallite size.

The SAXS measurement (Figure 5.1c) does not show any diffraction signals indicating a lack of a periodicity in the pore structure. However, the BJH pore size distribution derived from N_2-physisorption (see Figure 5.1d) on the templated MgO powders shows 2 local maxima indicating

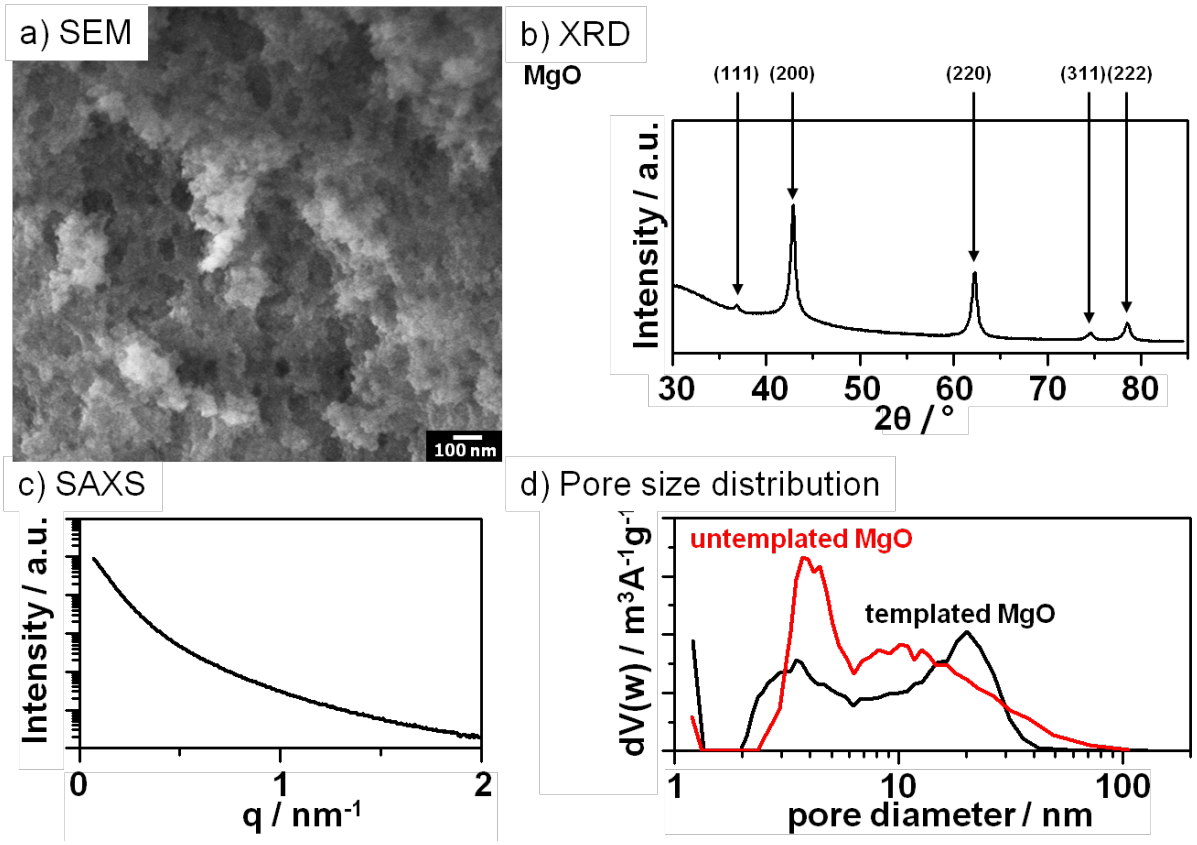

Figure 5.1.: Characterisation of MgO powder templated with PEO_{213}-PB_{184}-PEO_{213} obtained after heating with 5 K/min to 480 °C for 3 hours followed by 500 °C for 1 hour a) SEM b) XRD with reflection positions corresponding to MgO in periclase structure (PDF: 00-045-0946) c) SAXS; d) BJH- pore size distribution of the templated and untemplated MgO

the existence of mesopores. The local maximum at 20 nm corresponds well to the pore size obtained from SEM analysis in MgO films (see Figure 4.4d). In contrast, there is no maximum at 20 nm in the pore size distribution obtained from the MgO powder prepared without polymer template. Therefore, the maximum at pore diameters of 20 nm in the MgO powder prepared with PEO_{213}-PB_{184}-PEO_{213} probably originates from templating. In addition, the pore size distribution exhibits pores up to a size of 50 nm. This agrees well with the SEM results. The second local maximum at a pore diameter of 4 nm exists in the pore size distribution of powders synthesized with and without template indicates an intrinsic porosity probably generated by gaseous decomposition products during calcination. The BET surface area of the micelle-templated MgO powder amounts to 118 m^2/g.

In contrast to the BET surface area obtained for templated MgO powder, Li@MgO prepared with PEO_{213}-PB_{184}-PEO_{213} (133 m^2/g) as well as MgO (135 m^2/g) and Li@MgO (130 m^2/g) prepared without template show slightly higher surface area. However, the differences of surface area are not significant for the comparison of the OCM performance.

The SEM images of all MgO-based powders are shown in Figure A.11a-d. In contrast to the SEM results for micelle-templated MgO, the Li@MgO powders prepared with polymer template do not indicate the existence of templated porosity. In agreement with the micelle-templated MgO powder described above, all MgO-based powders consist of nanocrystallites.

This is in agreement with XRD analysis. The XRD patterns of all MgO-based powders are presented in Figure A.11a-d. All diffractograms show diffraction signals at $2\theta = 36.8°$ (111), 42.8° (200), 62.2° (220), 74.7° (311) and 78.7° (222) corresponding to MgO in periclase structure (PDF: 00-045-0946). The crystallite sizes obtained by applying Scherrer equation are 17 nm and 15 nm for MgO and Li@MgO prepared with polymer template, respectively. In contrast, the MgO and Li@MgO powders prepared without polymer template show smaller crystallite sizes of 12 nm and 10 nm, respectively. The developed synthesis strategy results in nanocrystalline material, although the crystallite sizes are significantly larger compared to MgO films (see Figure 4.4f). No additional Bragg reflexes where observed even for the Li@MgO powders. This indicates that no phase separation in a MgO and a second lithium containing phase (e.g. LiO) occurred during synthesis of Li@MgO powders.

The compositions of the MgO powders prepared with lithium were additionally analysed by ICP-OES. The lithium content for the Li@MgO prepared with PEO_{213}-PB_{184}-PEO_{213} polymer amounts to 0.099%wt and 0.110%wt for the sample prepared without template. Hence, the targeted concentration of 0.1%wt was obtained with good precision.

In summary, nanocrystalline MgO-based powders were prepared with and without polymer template as well as with and without lithium doping. Physisorption experiments indicate a templated pore structure in the sample prepared with polymer template, although SAXS suggested that pores are not well ordered in the powder samples. Hence, the transfer of the synthesis procedure of micelle-templated MgO from film to powder was only partially successful.

5.2. Catalytic Testing

The OCM performance of templated and untemplated MgO as well as Li@MgO was tested in parallel in a multi-channel fixed bed-reactor to ensure comparable conditions for each catalyst. The catalysts were tested between 500 and 800 °C every 50 K at constant flow of a CH_4/air feed (6:15 volume ratio) to gain information about the temperature dependency of the reaction.

Figure 5.2 presents the catalysis results of the MgO and Li@MgO, each prepared with and without PEO_{213}-PB_{184}-PEO_{213} polymer template showing the methane conversion (blue squares) and C_2-selectivity (violet squares) versus time-on-stream.

In general, all four catalysts are active and selective in OCM. The methane conversion as well as C_2-selectivity increases with increasing temperature. MgO and Li@MgO prepared with and without polymer template exhibite decreasing methane conversion with time-on-stream. This

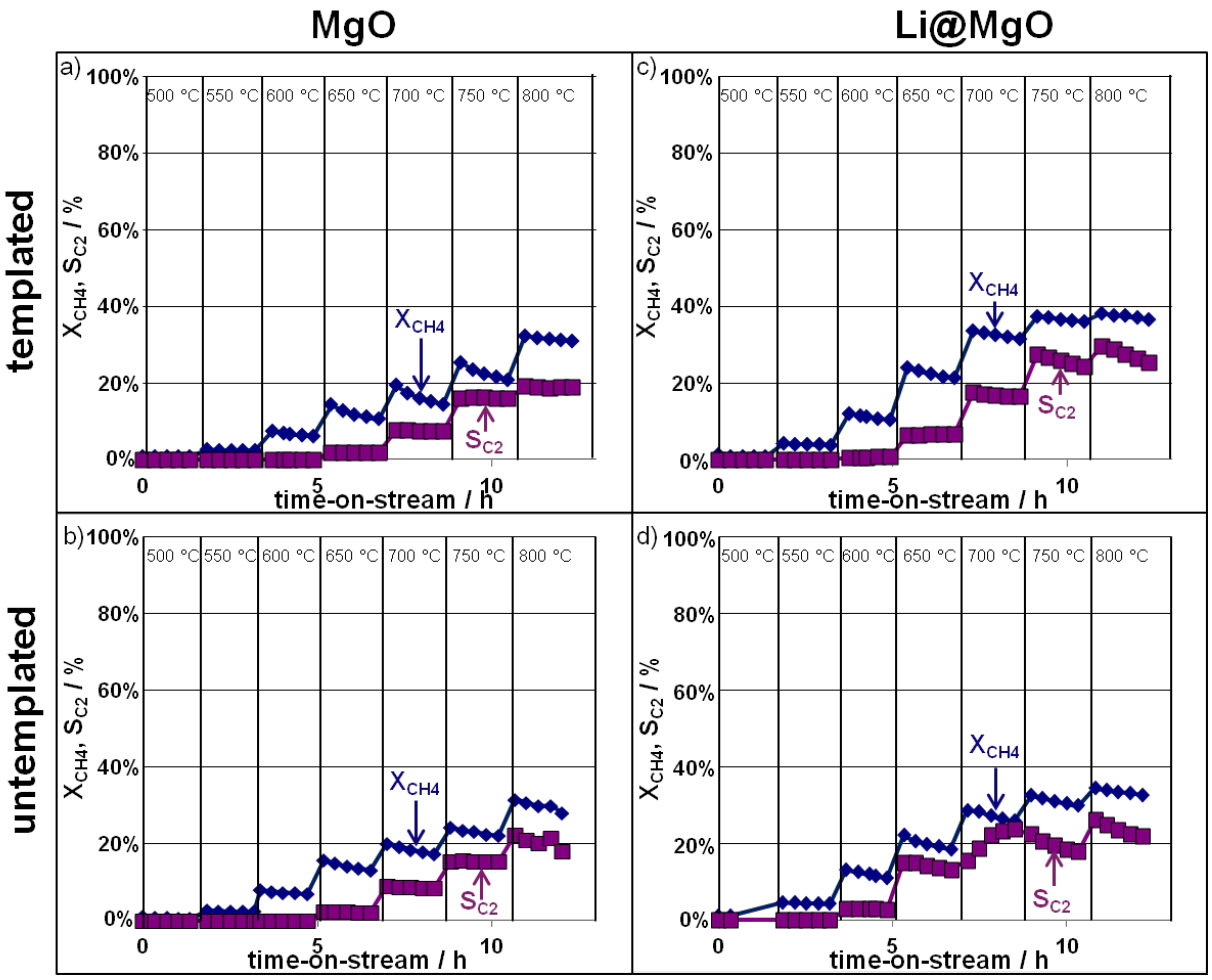

Figure 5.2.: Methane conversion X_{CH4} (blue squares) and C_2-selectivity (violet squares) versus time on stream of MgO prepared a) with and b) without PEO_{213}-PB_{184}-PEO_{213} as well as Li@MgO prepared c) with and d) without PEO_{213}-PB_{184}-PEO_{213}

deactivation is most likely caused by structural reconstruction of the catalyst morphology as reported for MgO-based catalyst prepared with different methods.[151] However, the MgO catalysts show constant C_2-selectivity at each temperature. Exemplarily, the MgO catalysts at 750 °C show C_2-selectivities of 17% (templated) and 15% (untemplated). In contrast, a decreasing selectivity towards ethane and ethylene is observed for Li@MgO catalysts at T > 750 °C.

In comparison of the OCM activity, both Li@MgO reveal a higher methane conversion than MgO catalyst. The initial conversion of the templated catalysts, for example, at 775 °C are 26% (MgO) and 37% (Li@MgO). The higher activity of MgO prepared with lithium is in good agreement with the literature.[151] Comparing the influence of templating, the MgO and Li@MgO prepared with PEO_{213}-PB_{184}-PEO_{213} exhibit slightly higher X_{CH4} (38% for Li@MgO at 750 °C) than to the untemplated MgO-based powders (32% for Li@MgO at 750 °C). However, the effect of templating is not significant.

The C_2-selectivity for all catalysts increases with increasing temperature. However, the lithium doped MgO powders are more selective towards C_2-products compared to pure MgO catalysts. The templated Li@MgO shows at 750 °C an initial selectivity of 29%. In contrast, for the templated MgO a lower selectivity of 17% is observed. The effect of the dopand indicates that lithium contributes to the OCM performance of the catalyst. Higher selectivities of MgO catalyst prepared with lithium is in agreement with the literature.[151,4] In addition, a significant influence of templating on the C_2-selectivity cannot be observed. Therefore, an influence of the pore system

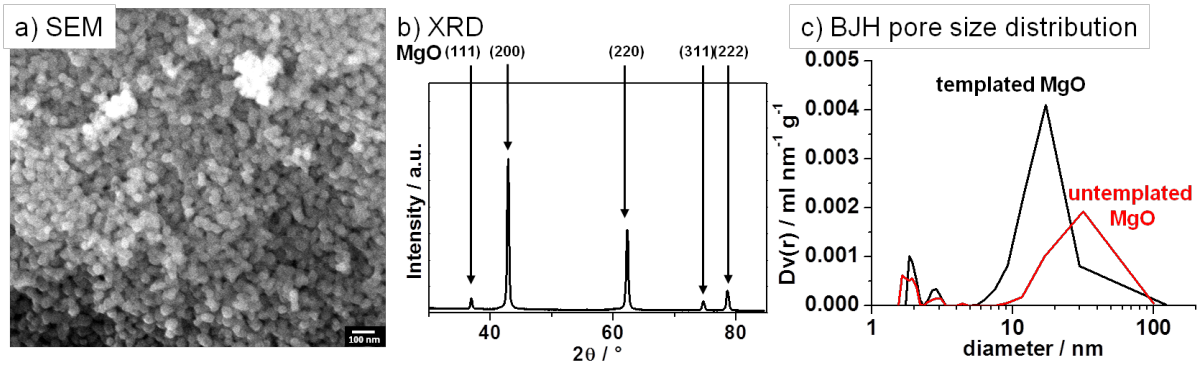

Figure 5.3.: Characterisation of MgO powder templated with PEO_{213}-PB_{184}-PEO_{213} after OCM catalysis a) SEM b) XRD with reflection positions corresponding to MgO in periclase structure (PDF: 00-045-0946) c) BJH- pore size distribution of the templated and untemplated MgO

is not detectable in this study.

All MgO-based catalysts show slowly decreasing methane conversion with time-on-stream at $>$ 600 °C. This deactivation progresses even faster with increasing temperature. An influence of templating on the deactivation cannot be observed. However, the deactivation is depending on the lithium content. Both Li@MgO catalysts exhibit decreasing S_{C2} at 750 °C and 800 °C. This deactivation at higher temperatures cannot be observed for undoped MgO catalysts. The MgO powders show constant selectivity at each temperature. Hence, the deactivation of MgO prepared with lithium indicates an additional deactivation mechanism initiated probably by the loss of lithium. Lithium loss was also reported by Arndt et al. for Li@MgO OCM catalyst independent of the preparation method.[151]

In summary, MgO and Li@MgO prepared with and without pore template are active and selective in OCM. The Lithium containing catalysts show higher conversion and higher selectivities at a given temperature. Templated catalyst show slightly higher methane conversion than the untemplated powder. However, a clear influence of templating in C_2-selectivity cannot be deduced.

5.3. Characterisation after OCM

The MgO and Li@MgO catalysts were analysed by SEM, XRD and N_2-physisorption after 12 hours OCM up to 800 °C (last data point in Figure 5.2).

Figure 5.3 presents a) a SEM image and b) a XRD pattern of templated MgO as well as c) BJH pore size distribution of the MgO prepared with and without polymer template. The SEM image 5.3a) of the templated MgO shows large and round crystallites with an average size of 48 nm. The image doesn't evidence any remaining pores in the material indicating a loss of templated porosity due to sintering of the crystallites.

The X-ray diffractogram (Figure 5.3b) shows narrow reflections with diffraction signals at 2θ = 36.9 (111), 42.9 (200), 62.2 (220), 74.6 (311) and 78.5 (222) corresponding to MgO in periclase structure (PDF: 00-045-0946). The Scherrer equation results in an average crystallite size of 44.0 nm for MgO powders indicating a strong sintering during OCM compared to the crystallite size of the pristine catalyst with 14.8 nm. The crystallite size is in good agreement with the SEM results.

The N_2-BET surface area of the templated MgO powder decreases significantly from 117.6 m^2/g to 65.9 m^2/g during OCM testing. The loss of surface area is most likely originated in the loss of microporosity due to sintering during OCM.

This assumption is supported by the results of the BJH pore size distribution presented in Figure 5.3c. While the pore size distribution of the pristine MgO catalysts prepared with and without template exhibits pores with diameters $<$ 8 nm, after 12 h of OCM testing only pores with

diameter > 8 nm remain in a significant amount. This change in the pore size distribution indicates a loss of micropores and small mesopores during OCM testing. The pore size distribution of the templated MgO still indicates the maximum amount of pores at a diameter of 20 nm. However, the broad distribution peak indicates also pore sizes up to 100 nm. The untemplated MgO after OCM shows a broad pore size distribution between 10 and 100 nm with a maximum at 31 nm. Most likely the measured pores are present in the form of inter-crystallite volume between the grown MgO crystallites.

This change in the pore size distribution is also reflected in the decreased BET surface area of the untemplated MgO powder. During OCM the surface area of the untemplated MgO is diminished from 135 m^2/g to 31 m^2/g. This trend of decreasing surface area can also be observed for Li@MgO catalysts. After catalytic testing the Li@MgO catalysts prepared with and without polymer template have surface areas of 29 m^2/g and 15 m^2/g, respectively. This loss indicates a strong sintering of all MgO-based catalysts during OCM testing.

Figure A.12 presents the SEM and XRD results for the templated catalysts a) MgO and b) Li@MgO as well as the untemplated catalysts c) MgO and d) Li@MgO after catalysis. In comparison to the SEM images recorded for the fresh prepared catalysts (see Figure A.11) all four SEM images recorded after OCM testing feature round crystallites with drastically increased size. The average crystallite size obtained from the SEM image amounts to 48 nm for the templated and 42 nm for the untemplated MgO. The SEM crystallite size for Li@MgO is even larger with diameters of 71 nm (templated) and 61 nm (untemplated). Hence, all catalysts show a severe increase in crystallite sizes after OCM. In addition, the Li@MgO catalyst exhibits an even stronger crystallite growth compared to MgO. This indicates an influence of the lithium content on the sintering behaviour at higher temperatures.

The increase of crystallite size for all catalysts as well as stronger sintering for lithium containing MgO-based powders can also be confirmed by XRD (see Figure A.12). In general, the diffraction signals for all catalysts correspond to MgO in periclase structure (PDF: 00-045-0946). The crystallite size obtained from Scherrer equation results for MgO to 44 nm (templated) and 37 nm (untemplated) as well as for Li@MgO to 51 nm (templated) and 47 nm (untemplated). Therefore, XRD results confirm the strong crystallite growth of all MgO-based catalysts during OCM.

The XRD results agree with SEM findings that the lithium containing catalyst show significant stronger growth of the crystallites than MgO without Li. Hence, lithium in MgO influences the sintering process. Arndt et al.[151] suggested an alternative sintering mechanism induced by loss of lithium. Therefore, the amount of Li after catalysis was analysed by ICP-OES. The quantification of lithium results for the templated as well as the untemplated Li@MgO samples to 0.02%wt. Hence, the doped catalysts lose about 80% of the initial lithium content during the catalytic testing. Thus, this is in good agreement with the literature[151] and the loss of lithium is likely to be the reason for the extended crystallite growth during OCM testing. In addition, XRD reveals no crystalline phase corresponding to a lithium containing phase.

In summary, the MgO catalysts show a strong increase in crystallite size during the OCM reaction for 12 h up to 800 °C. These crystallite growth results in a drastically decreased surface area and a loss of pore structure in the catalyst. Moreover, both Li@MgO catalysts lose significant amounts of the lithium dopand.

5.4. Discussion

Aim of this part of the thesis was to synthesize of MgO and Li@MgO with and without templated mesoporosity and to test catalysts on their OCM performance.

The synthesis of MgO films with controlled mesoporosity was successfully transferred to obtain MgO powders. The templating of the MgO powders was only partly successful (see section 5.1). However, all obtained catalysts were active and selective during OCM testing.

Lithium as dopand in MgO was reported to have major influence on the OCM performance and the [Li^+O^-]-species were considered as active centre for the methane activation in MgO-based OCM catalysts.[4,151] The increase of OCM performance by the addition of lithium to MgO is also confirmed by the data presented in this thesis. The Li@MgO catalyst showed higher methane conversion as well as higher selectivity towards C_2-products compared to the MgO prepared without additional lithium. The higher activity was also reported by the groups of Lunsford and Arndt.[4,151] Lunsford et al. reported at 700 °C a methane conversion of 40% and a C_2-selectivity of 45%. In comparison to Lunsford, Li@MgO prepared with polymer template in this thesis exhibits at 700 °C lower activity with a conversion of 34% and a selectivity of 19% (see section 5.2).

However, the group of Lunsford did not reporte any OCM activity for pure MgO.[4] This lack of OCM performance is not in agreement with the presented data in this thesis (see Figure 5.2). The pure MgO catalysts are active and selective in OCM reaction, although the catalytic performance is lower. The OCM activity of MgO as well as its lower C_2-selectivity compared to the Li@MgO is in good agreement with the results reported by Arndt et al.[151] Hence, lithium doping increase the OCM performance of MgO-based catalyst but is not necessary to obtain an active OCM catalyst.

In comparison of templated and untemplated catalyst, the MgO-based powders prepared with polymer template show a slightly higher methane conversion. However, this higher activity is not significant. Moreover, an influence of templating on the C_2-selectivity was not observed. In general, an influence of porosity can hardly be extracted from the present data due to excessive restructuring of the catalyst during OCM testing.

The characterisation of the MgO-based catalysts after OCM testing (see section 5.3) reveals the strong increase of the crystallite size. The MgO prepared with lithium shows an even stronger crystallite growth compared to pure MgO. This strong sintering tendency is accompanied by a loss of surface area and, therefore, can be associated with the loss of OCM performance at time-on-stream. This interpretation is in agreement with the reported results of the group of Arndt, who also observed a loss surface area accompanied by a loss of OCM performance.[151] In addition, Lunsford et al. did not mentioned any performance loss over longer time-on-stream after an initial decrease of OCM activity.

In summary, the synthesized MgO and Li@MgO catalysts prepared with and without polymer template are all active in OCM reaction. However, the obtained catalysts are not structurally stable during OCM testing and lose porosity by excessive sintering. Therefore, an extraction of an influence of the pore size on the C_2-selectivity cannot be extracted from the present data. However, one possibility to investigate an influence of the initial pore size could be achieved by fast heating to 750 °C with a high heating rate and measuring the OCM performance in the first 10 min. The extrapolation of the obtained data to t=0 could reveal a pore size influence.

In addition, another possibility to investigate the influence is to synthesize a structurally stable catalyst with controlled porosity and to test it in OCM. The next section presents the synthesis and OCM testing of a more stable W-Mn/SiO_2 catalyst with templated mesoporosity.

6. W-Mn/SiO_2 Catalyst for Oxidative Coupling of Methane

The material W-Mn/SiO_2 is known for its long time stability in OCM reactions and shows, compared to MgO-based ctalyst, a high C_2-selectivity.[30,12]

In this chapter a synthesis procedure is presented that yields W-Mn/SiO_2 with template controlled pore size. The characterisation of the freshly prepared material is discussed in section 6.1. The catalytic results of OCM testing are presented in section 6.2. The reproducibility of the synthesis and the OCM testing is analysed in section 6.3. In section 6.4 the influence of the pore size on the C_2-selectivity is discussed. Thereafter, the used catalyst is characterized in section 6.5 concerning morphological and compositional changes occuring during the catalytic testing. Finally, the results are discussed in section 6.6.

6.1. Synthesis and Characterisation

For the synthesis of W-Mn/SiO_2 OCM catalysts with controlled pore size a new synthesis procedure was developed in this thesis. The procedure is based on the SBA-synthesis for mesoporous silica reported by Zhao et al.[49,57] The pore size in the silica matrix is controlled by amphiphilic block-copolymers as templates. A set of silica based catalyst with different pore sizes is obtained by employing templates with different molecular weights (Pluronics Brij56, F108, F127 or P123) in the synthesis. The range of accessible pore sizes was further increased by swelling of the template.[49,57] The swelling of the micelles is accomplished by introducing the swelling agent trimethylbenzene into the hydrophobic core of P123 micelles. The enlargement of the micelles results in an increase of the pore diameter in the silica matrix. The SBA-synthesis was modified based on the sol-gel synthesis of W-Mn/SiO_2 OCM catalysts reported by Wang et al.[28] to introduce the OCM active elements tungsten and manganese.

Briefly, after dissolving the respective template polymer (Pluronics F127, Brij56, F108 or P123) at 60 °C in aqueous HCl the separately dissolved $Mn(NO_3)_2{\cdot}4H_2O$ and $Na_2WO_4{\cdot}2H_2O$ is added at once with a time delay of 30 s. The concentrations of the manganese and tungstate source are chosen to result in a content of 2%wt Mn and 5%wt Na_2WO_4 with respect to silica. The resulting solution is cooled down to 35 °C (22 °C when F127 was employed) and in the case of larger mesopores a certain amount of swelling agent trimethylbenzene was added. Then $Si(OEt)_4$ is added and stirred for 21 h at 35 °C (22 °C for F127) followed by a heat up to 80 °C without stirring. The final catalyst is obtained after filtration, drying at room temperature and calcination for 6 h at 500 °C reached by a heating ramp of 1 K/min. The catalyst powder is obtained as a yellowish solid. A more detailed synthesis description is given in section 3.3.2.

The final catalyst were characterized by N_2-physisorption in order to obtain its analysis BET surface area and pore size distribution employing NLDFT-Model as well as SAXS to gain imformation about the pore structure. The morphology of the powders were investigated by scanning electron microscopy. The crystalline phases were analysed by X-ray diffraction.

The following section presents the detailed analysis of the W-Mn/SiO_2 catalysts synthesized by employing Brij56, F108, F127 and P123 as structure directing agents.

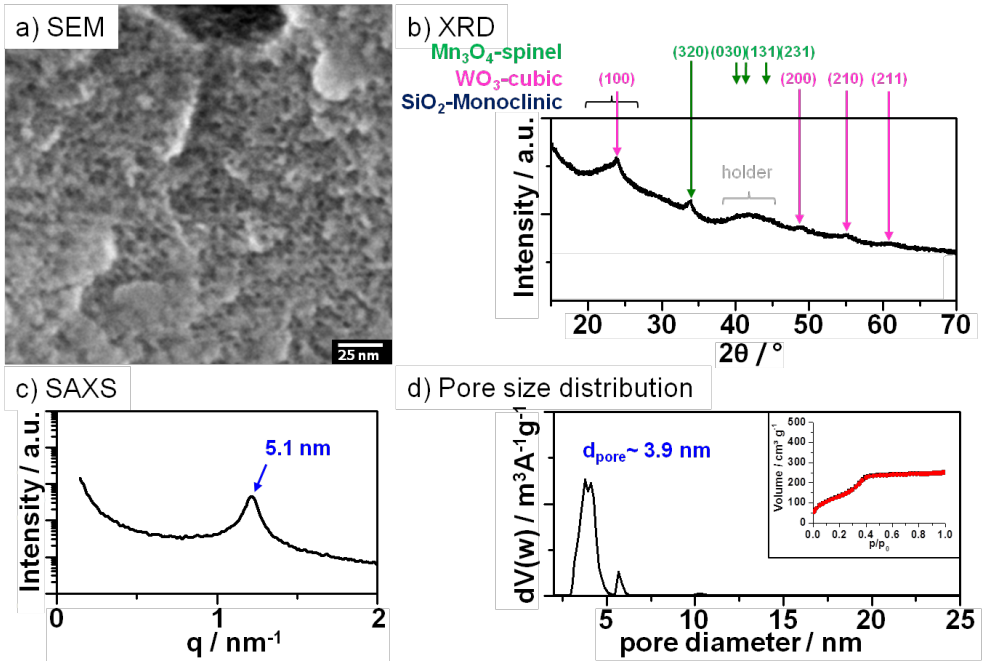

Figure 6.1.: Analysis of W-Mn/SiO_2 templated with Brij56 a) SEM, b) XRD, c) SAXS and d) NLDFT-pore size distribution (Quantachrom NLDFT-Modell: N2 at 77K on silica (cylindr./sphere. pore NLDFT ads. Modell) with inset showing N_2-adsorption (black) and desorption (red) isotherm

W-Mn/SiO_2 templated with Brij56

Figure 6.1 shows a) SEM, b) XRD, c) SAXS and d) pore size distribution derived from N_2-physisorption (with adsorption and desorption isotherms as inset) measurements recorded from the Brij56 templated catalyst.

The XRD analysis (see Figure 6.1b) reveals a combination of three crystalline phases. A broad and weak reflection at $2\theta = 24.0°$ can be assigned to monoclinic SiO_2 (PDF: 00-039-1425). The broad shape and unresolved peaks suggesting SiO_2 is present mainly in amorphous form. In addition, the XRD features signals at $2\theta = 23.8°, 48.9°, 55.1°, 61.2°$ corresponding well to cubic WO_3 (PDF: 00-041-0905). The Scherrer equation results in a crystallite size of 6 nm for tungsten oxide. The XRD shows additional diffraction signal at $2\theta = 33.8°, 41.7°, 44.2°, 46.9°$ corresponding well to spinel type Mn_3O_4 (PDF: 01-086-2337). The crystallite size of Mn_3O_4 estimated by Scherrer equation amounts to 6 nm. Hence, the developed synthesis procedure employing Brij56 as structure directing agent results in amorphous silica with nanocrystalline WO_3 and Mn_3O_4.

The SEM (see Figure 6.1a) features locally ordered spherical pores with an average diameter of 2.9 nm and the pore walls appear smooth and unstructured. This observation is in good agreement with the amorphous appearance of silica in the XRD.

The adsorption and desorption isotherms (see Figure 6.2d inset) show a strong increase of adsorbed gas volume at low relative pressures ($p/p_0 < 0.1$) indicating a significant amount of intrinsic microporosity. The weak hysteresis loop between $0.3 < p/p_0 < 0.4$ can be classified as H1-type and is typically observed for Brij56 templated SBA-11 with cubic pore structure.[49] However, the N_2-BET surface area amounts only to 522 m^2/g compared to 1070 m^2/g obtained by Zhao et al.[49] The main peak of the NLDFT pore size distribution (see Figure 6.1d) indicates a narrow range of mesopores between 2.9 and 5.2 nm with a maximum at 3.9 nm. This value is slightly larger compared to the SEM results and is in good agreement with the literature.[49] The SAXS analysis features a signal corresponding to a periodical distance of 5.1 nm indicating an ordered pore structure.

Thus, the developed synthesis route employing Brij56 as structure directing agent yields a W-

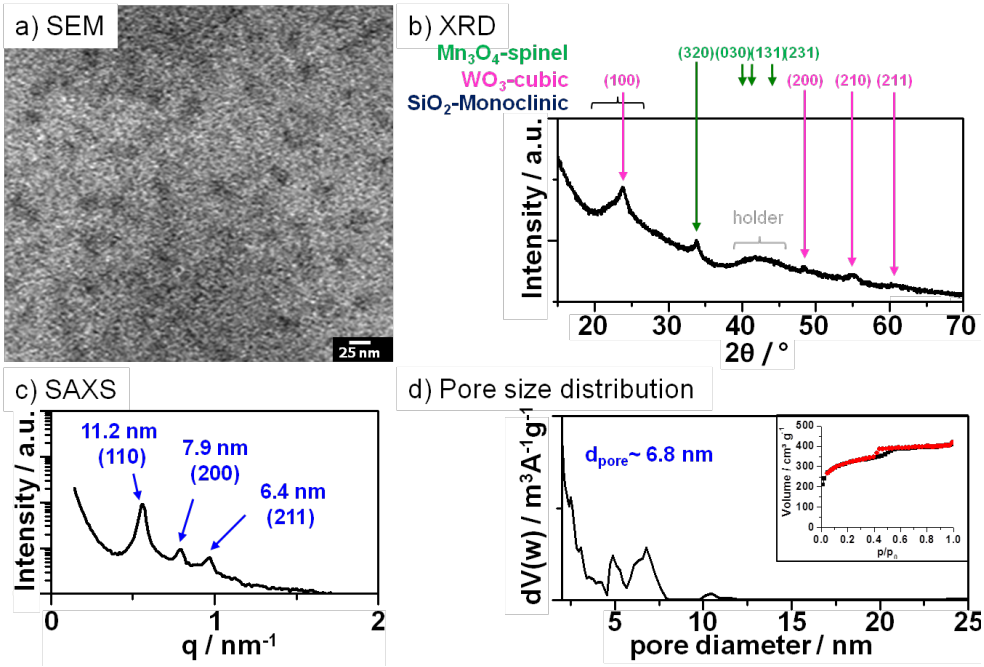

Figure 6.2.: Analysis of W-Mn/SiO_2 templated with F108 a) SEM, b) XRD c) SAXS and d) NLDFT-pore size distribution (Quantachrom NLDFT-Modell: N2 at 77K on silica (cylindr./sphere. pore NLDFT ads. Modell) with inset showing N_2-adsorption (black) and desorption (red) isotherm

Mn/SiO_2 material with template structured mesoporosity with incorporated tungsten oxide and manganese oxide.

W-Mn/SiO_2 templated with F108

Figure 6.2 shows a) SEM, b) XRD, c) SAXS and d) pore size distribution derived from N_2-physisorption (with adsorption and desorption isotherms as inset) measurements recorded from the F108 templated W-Mn/SiO_2 catalyst.

The SEM image (see Figure 6.2a) shows spherical pores with a diameter of 14 nm. The pores are significantly larger compared to the reported pore sizes of 4 nm in silica prepared with F108.[152] Whether the pores are originated from templating cannot be distinguished from the present data.

The PSD (see Figure 6.2d) of the material prepared with F108 as structure directing agent features 3 local maxima corresponding to pore sizes of 6.8 nm, 5.0 nm and 2.0 nm. The peak at 2 nm can be understood as an artefact of intrinsic microporosity. The maxima at 6.8 nm and 5.0 nm can be originated from F108 templated pores. The pore sizes are slightly larger compared to the literature value obtained from F108 templated SBA-16[152] with a pore diameter of 4 nm. The difference of pore diameters between the pure SBA-silica and W-Mn/SiO_2 catalyst prepared with F108 can originate from the additional tungsten and manganese species in the synthesis.

The adsorption and desorption isotherms (see Figure 6.2d inset) show a strong increase of adsorbed gas volume at low relative pressure ($p/p_0 < 0.1$) indicating a significant amount of intrinsic microporosity. The physisorption isotherms feature a hysteresis loop between $0.4 < p/p_0 < 0.6$. The form of the hysteresis loop can be categorised as H2-type (IUPAC) indicating a cubic pore structure. The shape of the isotherm is in good agreement with the literature.[152] However, the BET surface area amounts only to 358 m^2/g. Jin et al. reported significantly larger surface areas between 594 - 860 m^2/g.[152]

The SAXS measurement (see Figure 6.2c) features three Bragg reflection corresponding to d-spacings of 11.2 nm (110), 7.9 nm (200), 6.4 nm (211) indicating a cubic pore system with lattice constant of 15.8 nm.[153] Therefore, the SAXS and physisorption measurements suggesting the

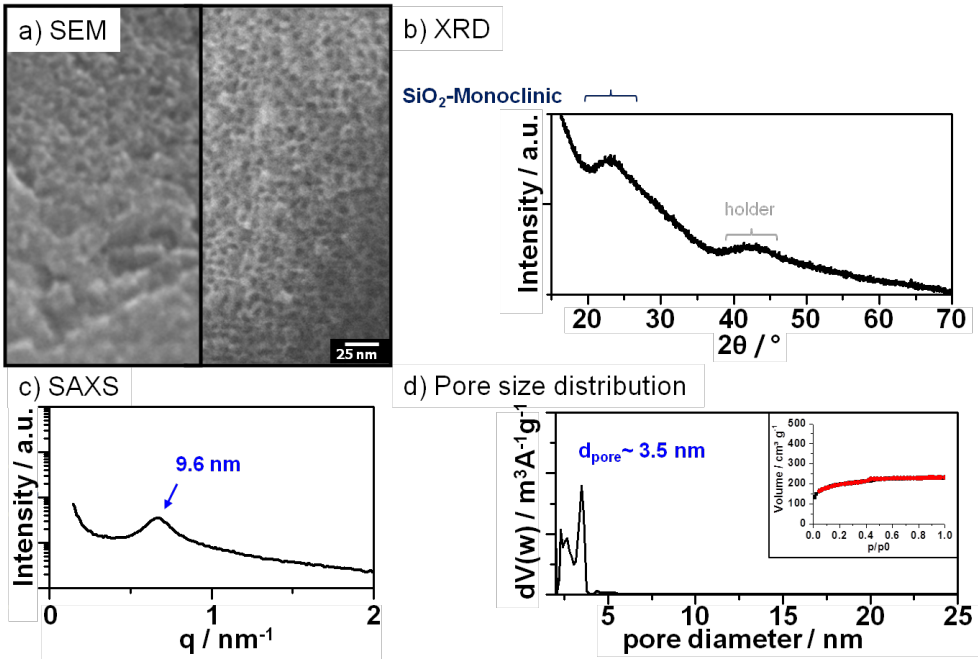

Figure 6.3.: Analysis of W-Mn/SiO_2 templated with F127 a) SEM, b) XRD, c) SAXS and d) NLDFT-pore size distribution (Quantachrom NLDFT-Modell: N2 at 77K on silica (cylindr./sphere. pore NLDFT ads. Modell) with inset showing N_2-adsorption (black) and desorption (red) isotherm

existence of a cubic pore structure in the W-Mn/SiO_2 prepared with F108. Hence, Pluronic F108 enables introducing controlled porosity into W-Mn/SiO_2 powder.

The XRD analysis (see Figure 6.2b) shows a broad and weak reflection at $2\theta = 24.0°$ indicating the presence of monoclinic SiO_2 (PDF: 00-039-1425) mainly in amorphous form. Further, the XRD features distinct signals at $2\theta = 23.8°, 48.9°, 55.1°, 61.2°$ corresponding well to cubic WO_3 (PDF: 00-041-0905). In addition, signals at $\theta = 33.8°, 41.7°, 44.2°, 46.9°$ corresponding well to spinel type Mn_3O_4 (PDF: 01-086-2337). The Scherrer equation results in crystallite sizes of 3 nm for tungsten oxide and 6 nm for manganese oxide.

Thus, the W-Mn/SiO_2 catalyst exhibits ordered pores templated by F108. Nanocrystalline WO_3 and Mn_3O_4 are present in the amorphous SiO_2 matrix.

W-Mn/SiO_2 templated with F127

Figure 6.3 shows a) SEM, b) XRD, c) SAXS and d) pore size distribution derived from N_2-physisorption (with adsorption and desorption isotherms as inset) measurements recorded from the F127 templated W-Mn/SiO_2 catalyst.

The SEM image of the catalyst (see Figure 6.3a, right panel) shows spherical pores with pore diameter of 4.0 nm. The pores are open towards the catalyst surface. In contrast, the second SEM image (see Figure 6.3a, left panel) does not show any pores indicating that the catalyst is not fully templated.

However, the pore size distribution (see Figure 6.3d) shows one strong maximum and a weak signal corresponding to a pore diameter of 3.5 nm and 2 nm, respectively. The diameter of the strong signal at a diameter of 3.5 nm is in good agreement with the SEM results. However, Zhao et al. reported pore diameters of 5.4 nm for SBA-16 templated with F127.[49]

The adsorption and desorption isotherms (see Figure 6.3d inset) show a strong increase of adsorbed gas volume at low relative pressure ($p/p_0 < 0.1$) indicating a significant amount of intrinsic microporosity. The physisorption isotherms feature a weak hysteresis loop between $0.4 < p/p_0 < 0.5$. The form of the hysteresis loop can be categorised as H2-type (IUPAC)

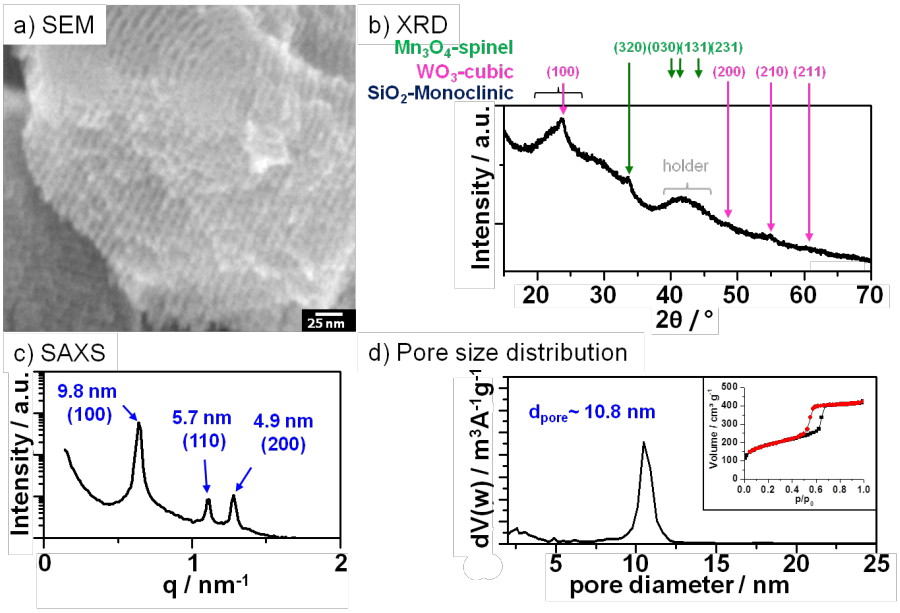

Figure 6.4.: Analysis of W-Mn/SiO_2 templated with P123 a) SEM, b) XRD, c) SAXS and d) NLDFT-pore size distribution (Quantachrom NLDFT-Modell: N2 at 77K on silica (cylindr./sphere. pore NLDFT ads. Modell) with inset showing N_2-adsorption (black) and desorption (red) isotherm

indicating a cubic pore structure. The N_2-BET surface area amounts to 662 m^2/g. This surface area is slightly smaller compared to the reported value of 740 m^2/g obtained for SBA-16 templated with F127.[49]

The SAXS measurement (see Figure 6.3c) shows one broad diffraction signal corresponding to a periodical distance of 9.6 nm indicating a local ordered pore system. The existence of pore order is in good agreement with the SEM results.

The XRD analysis feature only one broad diffraction signal at $2\theta = 24.0°$ indicating the presence of monoclinic SiO_2 (PDF: 00-039-1425). No signals corresponding to manganese or tungsten containing phases can be distinguished. Hence, manganese or tungsten containing species are not present in crystalline form. Thus, W-Mn/SiO_2 catalyst is only partially templated with F127. A crystalline phase containing manganese or tungsten cannot be detected. The OCM results of these catalysts have to be discussed with respect to this contradictory material characterisation.

W-Mn/SiO_2 templated with P123

Figure 6.4 shows a) SEM, b) XRD, c) SAXS and d) pore size distribution derived from N_2-physisorption (with adsorption and desorption isotherms as inset) measurements recorded from the W-Mn/SiO_2 catalyst prepared with P123.

The SEM image (see Figure 6.4a) of the material synthesized by employing triblock-copolymer Pluronic P123 shows cylindrical shaped pores with an average diameter of 4.3 nm. Pore diameter and pore structure are in good agreement to the SEM results of the pure silica SBA-15 with 4.7 nm reported by Zhao et al.[49]

The pore size distribution derived from physisorption measurements (see Figure 6.4d) features a narrow peak with maximum corresponding to a pore diameter of 10.8 nm. Therefore, the PSD pore diameter is larger compared to the reported value of 4.7 nm obtained from pure silica SBA-15,[49] but significantly larger compared to the pore diameter obtained by SEM of the W-Mn/SiO_2 catalyst. The adsorption and desorption isotherms (see Figure 6.4d inset) show a strong increase of adsorbed gas volume at low relative pressure ($p/p_0 < 0.1$) indicating a significant amount of intrinsic microporosity. The isotherms feature a strong H1-type hysteresis loop between $0.5 < p/p_0 < 0.7$ indicative for cylindrical pores. The pore shape matches the SEM results. The

BET surface area amounts to 640 m^2/g. Therefore, the surface area is in the same order of magnitude compared to the reported value for pure SBA-15 of 690 m^2/g.[49]

The SAXS analysis (see Figure 6.4c) shows three Bragg reflections corresponding to d-spacings of 9.8 nm (100), 5.7 nm (110), 4.9 nm (200) indicating a hexagonal pore system with a lattice constant of 11.3 nm. The periodical distances and the pore system agree well with the physisorption and SEM results as well as with the reported results for SBA-15.[49]

The XRD analysis (see Figure 6.4b) shows a broad and weak reflection at $2\theta = 24.0°$ indicating the existence of monoclinic SiO_2 (PDF: 00-039-1425). Therefore, silica is present in amorphous form. In addition, the diffractogram features the signals at $2\theta = 23.8°$, 48.9°, 55.1°, 61.2° corresponding well to cubic WO_3 (PDF: 00-041-0905). The Scherrer equation results in a crystallite size of 5 nm for tungsten oxide. The XRD shows additional diffraction signals at $2\theta = 33.8°$, 41.7°, 44.2°, 46.9° corresponding well to spinel type Mn_3O_4 (PDF: 01-086-2337). The crystallite size of Mn_3O_4 estimated by Scherrer equation amounts to 5 nm.

Hence, the developed synthesis procedure employing P123 as structure directing agent results in amorphous silica with a hexagonal pore system and a narrow pore size distribution. WO_3 and Mn_3O_4 are present in nanocrystalline form in the silica matrix.

In summary, the physical characterisation evidences that the W-Mn/SiO_2 materials are mesostructured by the polymer templates Pluronic (F127, Brij56, F108, P123) and the developed synthesis route giving access to potential catalysts with templated pores from 3.5 nm to 10.8 nm with comparable element composition.

To further extend the range of available pore sizes in the W-Mn/SiO_2 material the templating P123 micelles were enlarged by the addition of 0.25 ml, 0.5 ml and 0.75 ml of the swelling agent trimethylbenzene (TMB) during the synthesis. Synthesis procedure as well as swelling agent were adapted from Zhao et al.[49,57]

W-Mn/SiO_2 templated with P123 and 0.25 ml TMB

Figure 6.5 shows a) SEM, b) XRD, c) SAXS and d) pore size distribution derived from N_2-physisorption (with adsorption and desorption isotherms as inset) measurements recorded from the W-Mn/SiO_2 catalyst prepared with P123 and 0.25 ml trimethylbenzene.

The SEM image (see Figure 6.5a) of the material prepared with Pluronic P123 and 0.25 ml TMB shows cylindrically shaped pores with an average diameter of 6.1 nm. This pore diameter is lower compared to the values obtained by Zhao et al. for pure SBA-15 prepared with the same amount of TMB (∼11 nm observed by TEM).[57]

The XRD analysis (see Figure 6.5b) features only one broad diffraction signal at $2\theta = 24.0°$ indicating the presence of monoclinic SiO_2 (PDF: 00-039-1425). No signals corresponding to manganese or tungsten containing phase can be distinguished. Hence, manganese or tungsten containing species are not present in crystalline form.

The adsorption and desorption isotherms (see Figure 6.5d inset) show a strong increase of adsorbed gas volume at low relative pressure ($p/p_0 < 0.1$) indicating a significant amount of intrinsic microporosity. The isotherms feature a distinct H1-type hysteresis loop between $0.65 < p/p_0 < 0.8$ indicative for cylindrical pores. The shape of the isotherm and the hysteresis loop are in good agreement with the literature obtained from SBA-15 prepared with TMB as swelling agent.[49] The BET surface area amounts to 755 m^2/g. The pore size distribution (see Figure 6.5d) derived from physisorption shows a strong maximum at a pore diameter of 11.7 nm and weak shoulder at 13 nm. These pore diameters are significantly higher compared to the pore size obtained from SEM, but in good agreement with the literature value obtained from SBA-15 prepared with 0.25 ml TMB.[57]

SAXS analysis (see Figure 6.5c) shows three Bragg reflections corresponding to d-spacings of 10.3 nm (100), 5.9 nm (110) and 5.1 nm (200) indicating a hexagonal pore system with a lattice

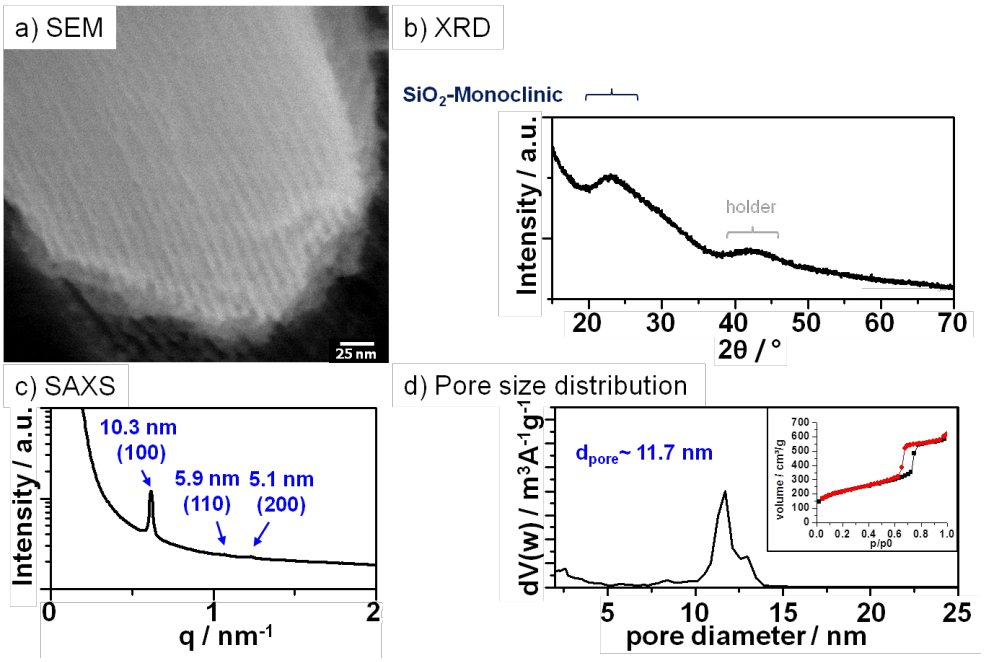

Figure 6.5.: Analysis of W-Mn/SiO_2 prepared with P123 and 0.25 ml trimethylbenzene a) SEM, b) XRD, c) SAXS and d) NLDFT-pore size distribution (Quantachrom NLDFT-Modell: N2 at 77K on silica (cylindr./sphere. pore NLDFT ads. Modell) with inset showing N_2-adsorption (black) and desorption (red) isotherm

constant of 11.8 nm. The pore structure is in good agreement with the physisorption and SEM results as well as with the reported results for SBA-15 prepared with TMB as swelling agent.[57]

Thus, the W-Mn/SiO_2 catalyst prepared with P123 and 0.25 ml trimethylbenzene is structured with ordered cylindrical pores.

W-Mn/SiO_2 templated with P123 and 0.5 ml TMB

Figure 6.6 shows a) SEM, b) XRD, c) SAXS and d) pore size distribution derived from N_2-physisorption (with adsorption and desorption isotherms as inset) measurements recorded from the W-Mn/SiO_2 catalyst prepared with P123 and 0.5 ml trimethylbenzene.

The SEM image (see Figure 6.6a) of the material prepared with Pluronic P123 and 0.5 ml TMB shows cylindrical shaped pores with an average diameter of 7.1 nm. The pore diameter is lower compared to the values obtained from SBA-15 prepared with 0.5 ml TMB (~12.5 nm observed by TEM).[57]

The XRD analysis (see Figure 6.6b) features only one broad diffraction signal at $2\theta = 24.0°$ indicating the presence of monoclinic SiO_2 (PDF: 00-039-1425). No signals corresponding to manganese or tungsten containing phase can be distinguished. Hence, manganese or tungsten containing species are not present in crystalline form.

The adsorption and desorption isotherms (see Figure 6.6d inset) show a strong increase of adsorbed gas volume at low relative pressure ($p/p_0 < 0.1$) indicating a significant amount of intrinsic microporosity. The isotherms feature a hysteresis loop between $0.48 < p/p_0 < 1.0$. The overall shape of the loop cannot be categorised according to IUPAC classification. However, the loop appears to be a superposition of a H1-type ($0.48 < p/p_0 < 0.8$) and a H2-type ($0.8 < p/p_0 < 1.0$) hysteresis loop indicating a mixture of cylindrical and larger spherical pores, respectively. However, the NLDFT pore size distribution features only one major signal with a maximum corresponding to pore diameters of 13 nm. These pore diameter is significantly higher compared to the pore size obtained from SEM, but agrees well with the literature value obtained from SBA-15 prepared with

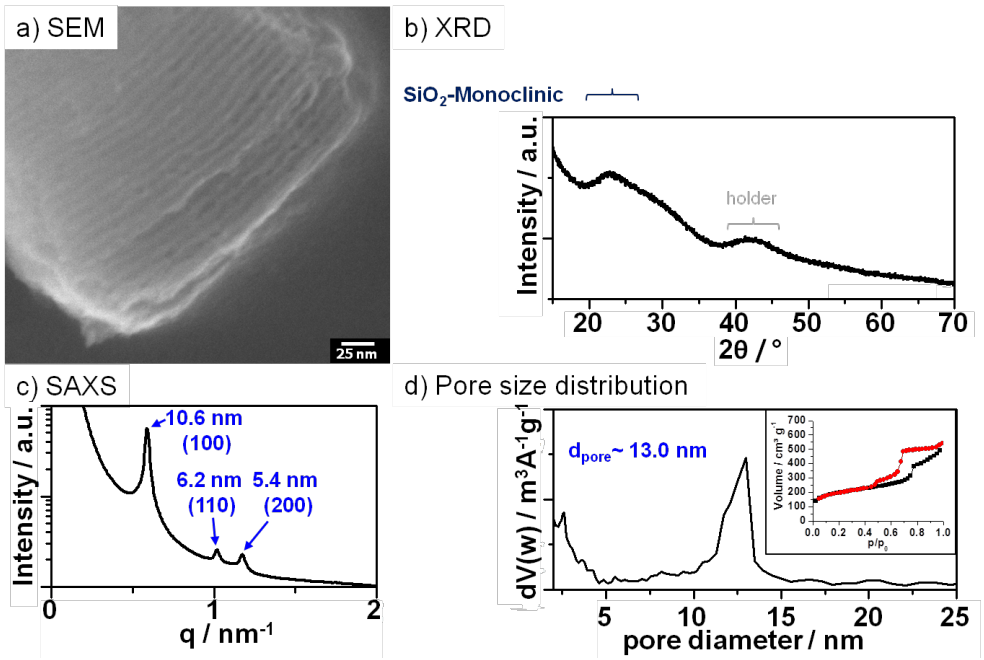

Figure 6.6.: Analysis of W-Mn/SiO_2 prepared with P123 and 0.5 ml trimethylbenzene a) SEM, b) XRD, c) SAXS and d) NLDFT-pore size distribution (Quantachrom NLDFT-Modell: N2 at 77K on silica (cylindr./sphere. pore NLDFT ads. Modell) with inset showing N_2-adsorption (black) and desorption (red) isotherm

0.5 ml TMB.[57] The BET surface area amounts 682 m^2/g which is significantly lower compared to the literature values obtained from SBA-15 prepared with swelling agent TMB.

SAXS analysis (see Figure 6.6c) shows three Bragg reflections corresponding to d-spacings of 10.6 nm (100), 6.2 nm (110) and 5.4 nm (200) indicating a hexagonal pore system with a lattice constant of 12.5 nm. The pore structure is in good agreement with the physisorption and SEM results as well as with the reported results for SBA-15 prepared with TMB as swelling agent.[57]

Thus, the W-Mn/SiO_2 catalyst prepared with P123 and 0.5 ml trimethylbenzene is structured with ordered cylindrical pores.

W-Mn/SiO_2 templated with P123 and 0.75 ml TMB

Figure 6.7 shows a) SEM, b) XRD, c) SAXS and d) pore size distribution derived from N_2-physisorption (with adsorption and desorption isotherms as inset) measurements recorded from the W-Mn/SiO_2 catalyst prepared with P123 and 0.75 ml trimethylbenzene.

The SEM image (see Figure 6.7a) recorded from W-Mn/SiO_2 catalyst prepared with 0.75 ml TMB shows a weakly structured surface. Only a few spherical pores with a diameter of about 18 nm can be distinguished. The diameter is slightly higher compared to the reported pore size of ~15 nm for pure SBA-15 prepared with 0.75 ml TMB.

The pore size distribution (see Figure 6.7d) does not show any pronounced peak indicating a broad distribution of pore sizes. The adsorption and desorption isotherms (see Figure 6.7d inset) show a strong increase of adsorbed gas volume at low relative pressure ($p/p_0 < 0.1$) indicating a significant amount of intrinsic microporosity. The isotherm features a hysteresis loop between $0.48 < p/p_0 < 0.9$. This loop can be classified as H1-type hysteresis and is indicative for a cubic pore structure. Further, the existence of the hysteresis loop evidences the existence of accessible mesopores. In addition, the BET surface area amounts to 604 m^2/g.

The SAXS analysis (see Figure 6.7c) features one weak signal corresponding to a periodical pore distance of 12 nm. The peak indicates the existence of locally ordered porosity in the material.

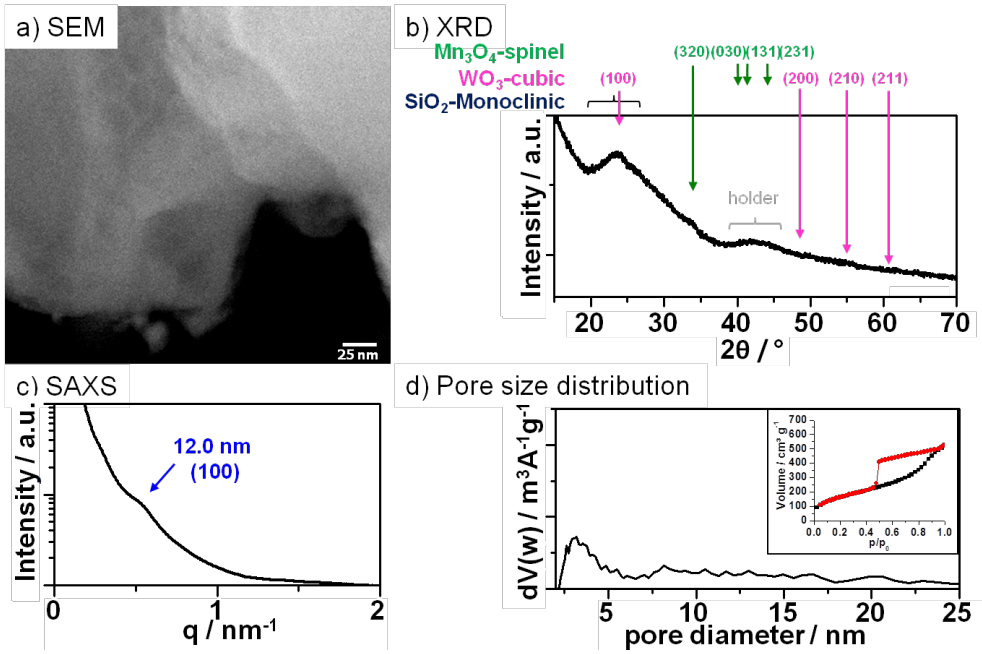

Figure 6.7.: Analysis of W-Mn/SiO_2 prepared with P123 and 0.75 ml trimethylbenzene a) SEM, b) XRD, c) SAXS and d) NLDFT-pore size distribution (Quantachrom NLDFT-Modell: N2 at 77K on silica (cylindr./sphere. pore NLDFT ads. Modell) with inset showing N_2-adsorption (black) and desorption (red) isotherm

The XRD analysis (see Figure 6.7b) shows a broad and weak reflection at $2\theta = 24.0°$ indicating the existence of monoclinic SiO_2 (PDF: 00-039-1425). Therefore, silica is present in amorphous form. In addition, the diffractogram features the signals at $2\theta = 23.8°$, 48.9°, 55.1°, 61.2° corresponding well to cubic WO_3 (PDF: 00-041-0905). The XRD shows additional diffraction signal at $2\theta = 33.8°$, 41.7°, 44.2°, 46.9° corresponding well to spinel type Mn_3O_4 (PDF: 01-086-2337). The reflexes of manganese and tungsten oxide are too weak to apply the Scherrer equation.

Thus, the W-Mn/SiO_2 catalyst prepared with P123 and 0.75 ml trimethylbenzene yields a material with a broad pore size distribution and may be not fully templated. The OCM results of these catalysts should be discussed with caution.

In summary, the developed synthesis strategy yields W-Mn/SiO_2 powders with templated mesopores and partly nanocrystalline Mn_3O_4 and WO_3. The pore diameter increases with increasing molecular weight of the templating polymer. Therefore, the pore diameters are varied between 3.5 to 10.8 (PSD) by employing different sized templates. Hence, the pore templating enables a systematic pore size variation in one OCM catalyst. The variation of the pore sizes in dependence of the template is in good agreement with the literature, although the concrete pore diameter diverge. Only the templating with F127 yields pores with drastically reduced diameter compared to the literature. The pore structure is mainly defined by the chemical and physical properties of the template. Templating with Brij56, F108 and F127 yields W-Mn/SiO_2 catalyst with a cubic pore structure. Templating with P123 results in cylindrical shaped pores with hexagonal pore structure.

However, employing P123 with the swelling agent TMB can change the pore structure. A hexagonal pore structure is obtained for volumes up to 0.25 ml TMB. In contrast, physisorption isotherms recorded from the material prepared with P123 and 0.5 ml TMB suggesting a mixture of hexagonal and cubic pore structure. The W-Mn/SiO_2 catalyst obtained by templating with P123 and 0.75 ml TMB exhibits poorly ordered spherical pores. However, the pore diameter increases systematically with increasing amount of swelling agent. Hence, the range of pore sizes could be further extended by swelling of the templating P123 micelles with trimethylbenzene up to 18 nm.

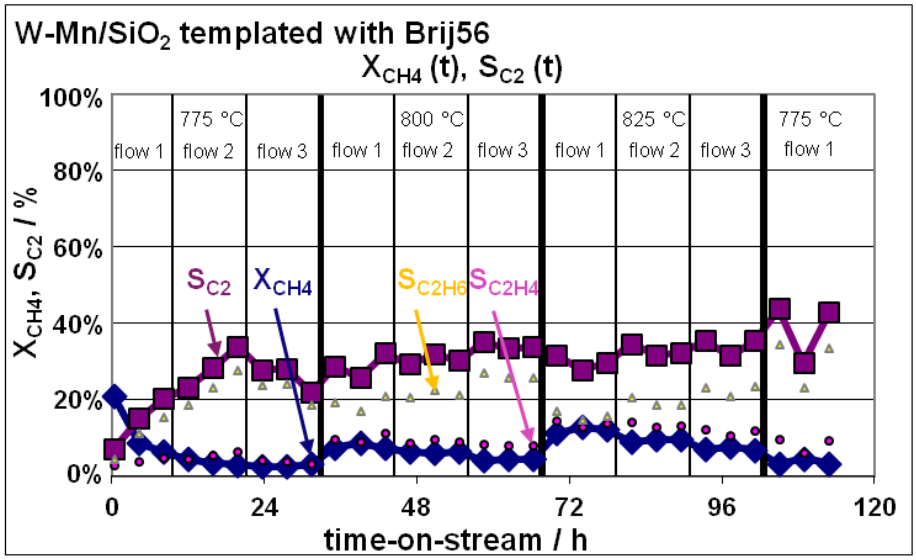

Figure 6.8.: Methane conversion X_{CH4} (blue squares) and selectivity (S_{C2} violet squares, S_{C2H6} yellow triangles, S_{C2H4} pink circles) versus time-on-stream of the W-Mn/SiO_2 catalyst prepared with Brij56 recorded at 775 °C, 800 °C and 825 °C with three flow rates (flow 1 < flow 2 < flow 3) at each temperature

In addition, the N_2-BET surface area of the materials is not correlated to the pore sizes and is most likely determined by microporosity.

The crystalline composition analysed by XRD exhibits SiO_2 for all prepared catalyst. The broad shape and unresolved peaks suggesting SiO_2 is present mainly in amorphous form. Additional reflexes corresponding to nanocrystalline Mn_3O_4 and WO_3 are present in the diffractogram recorded from catalysts prepared with Brij56, F108, P123 as well as P123 + 0.75 ml TMB. The small crystallite size allows the crystallite to be present in the pore walls of the mesoporous silica. However, the catalyst prepared with F127 as well as P123 with 0.25 ml TMB and P123 with 0.5 ml TMB does not feature signals corresponding to crystalline tungsten or manganese containing phases.

6.2. Catalytic Testing

The catalytic testing was performed in parallel in a multi-channel fixed bed-reactor to ensure comparable conditions for each catalyst. The catalysts were tested at three temperatures (775 °C, 800 °C, 825 °C) to gain information about the temperature dependence of the reaction. At each temperature the performance was analysed with three different gas flows rates (flow 1 < flow 2 < flow 3) to vary the contact time, but with a constant gas feed composition of 6:15 CH_4:air (volume ratio). The variation of the contact time leads to different methane conversion allowing the comparison of the catalysts selectivities at the same conversion and temperature, even if the overall performance varies between the catalysts. After catalytic testing at 825 °C at all three flow rates, the reactor was cooled down to 775 °C with flow rate 1 and the OCM was tested again at flow rate 1 to gain information about overall catalyst stability after 120 h.

Figure 6.8 presents the catalysis results of the Brij56 structured W-Mn/SiO_2 on the OCM reaction showing the methane conversion (blue squares) and selectivity (S_{C2} violet squares, S_{C2H6} yellow triangles, S_{C2H4} pink circles) versus time-on-stream.

The methane conversion shows a strong initial loss from the first to the second point from 21% to 9% indicating either a restructuring of the pore system or change in the phase composition of the catalyst. After the initial activity drop, the catalyst stabilises and the methane conversion varies between 13.0% to 2.5% depending on the applied conditions.

In general, the conversion increases with higher temperatures. At the lowest flow rate 1 and 775 °C the methane conversion is between 7 and 9%. At 800 °C and 825 °C at flow rate 1 the methane conversion is increased to 8 - 9% and 11 - 12%, respectively. This increase of the conversion results from increasing reaction kinetics caused by higher temperatures.

In contrast to the temperature dependence, higher gas flow rates result in decreasing methane conversion, for instance X_{CH4} decreases at 800 °C from 8% (flow 1) to 6% (flow 2) to 4% (flow 3). Higher flow rates result in shorter contact times. Methane has less time at the catalyst to be converted into C_2 or CO_x.

After 101 h time-on-stream the reactor is cooled down to starting conditions (775 °C with flow rate 1) and the catalyst shows a slightly lower methane conversion (X_{CH4} = 4 - 5%) compared to the initial starting conditions (X_{CH4} = 7 - 9%) indicating a loss of activity due to either a restructuring of the pore system or change in the phase composition of the catalyst.

Both ethane and ethylene are observed as selective reaction products. In general, the ethane selectivity is higher compared to ethylene. The S_{C2H6} increases with higher flow rates, for example the ethane selectivity increases from 21% (flow rate 2) to 26% (flow rate 3) at 800 °C. However, the S_{C2H6} decreases with higher temperature, for example from 26% at 800 °C and flow rate 2 to 24% at 825 °C and the same flow rate.

In contrast to the behaviour of S_{C2H6}, the ethylene selectivity decreases with higher flow rates, for example from 9.5% (flow rate 2) to 8% (flow rate 3) at 800 °C. The S_{C2H4} increase slightly with increasing temperature rates, for example from 9.5% at 800 °C and flow rate 2 to 14% at 825% and the flow rate 2.

Hence, ethane and ethylene selectivity show opposing temperature and flow rate dependency. These dependencies suggest C_2H_4 to be the secondary product of the OCM, resulting from the dehydrogenation of C_2H_6. A lower flow rate and, therefore, shorter contact times decrease the time for the dehydrogenation reaction, too. Therefore, an increase of ethane is detected while ethylene concentration is reduced. At lower flow rates but higher temperature the subsequent dehydrogenation reaction occurs more often and the ethylene selectivity increases. This finding is in good agreement with reaction sequence described in literature.[3,10]

The selectivity S_{C2} is the result of the summation of ethane and ethylene selectivity and is a measure for the overall methane coupling ability of a catalyst at a given temperature and flow rate. The C_2-selectivity increases slightly with higher temperatures, for example from 30% (800 °C) to 32% (825 °C) at flow rate 2. In addition, the C_2-selectivity increases with higher flow rate (smaller contact times), for example from 30% (flow rate 2) to 34% (flow rate 3) at 800 °C. This increase of C_2-selectivity increases with higher flow rate (smaller contact times), because the time at the catalyst for subsequent oxidation of ethane and ethylene to CO_x is shorter, suggesting the overoxidation products to be mainly formed by oxidation of C_2-products. This is in good agreement with the literature.[10]

In summary, employing the W-Mn/SiO_2 catalysts prepared with Brij56 in OCM reaction yields the C_2-products C_2H_6 and C_2H_4 accompanied by unconverted methane and the overoxidation products CO and CO_2. The amount of C_3-products (for example propane, propylene) was below the detection limit of the gas chromatograph. Hence, the micelle templated W-Mn/SiO_2 catalysts are active in the reaction of methane towards C_2-products (ethene, ethylen).

Figure 6.9 presents the catalysis results of W-Mn/SiO_2 prepared with a) F108, b) F127, c) P123, d) P123 + 0.25 ml TMB, e) P123 + 0.5 ml TMB and f) P123 + 0.75 ml TMB on the OCM reaction showing the methane conversion X_{CH4} (blue squares) and selectivity (C_2 violet squares, C_2H_6 yellow triangles, C_2H_4 pink circles) versus time-on-stream.

The catalysts show the same temperature and flow rate dependency compared to the described W-Mn/SiO_2 catalyst prepared with Brij56. After a strong initial loss of methane conversion the deactivation trend slows down but remains apparent with time-on-stream. This initial loss of activity suggests either a restructuring of the pore system or a change in the phase composition of the catalyst.

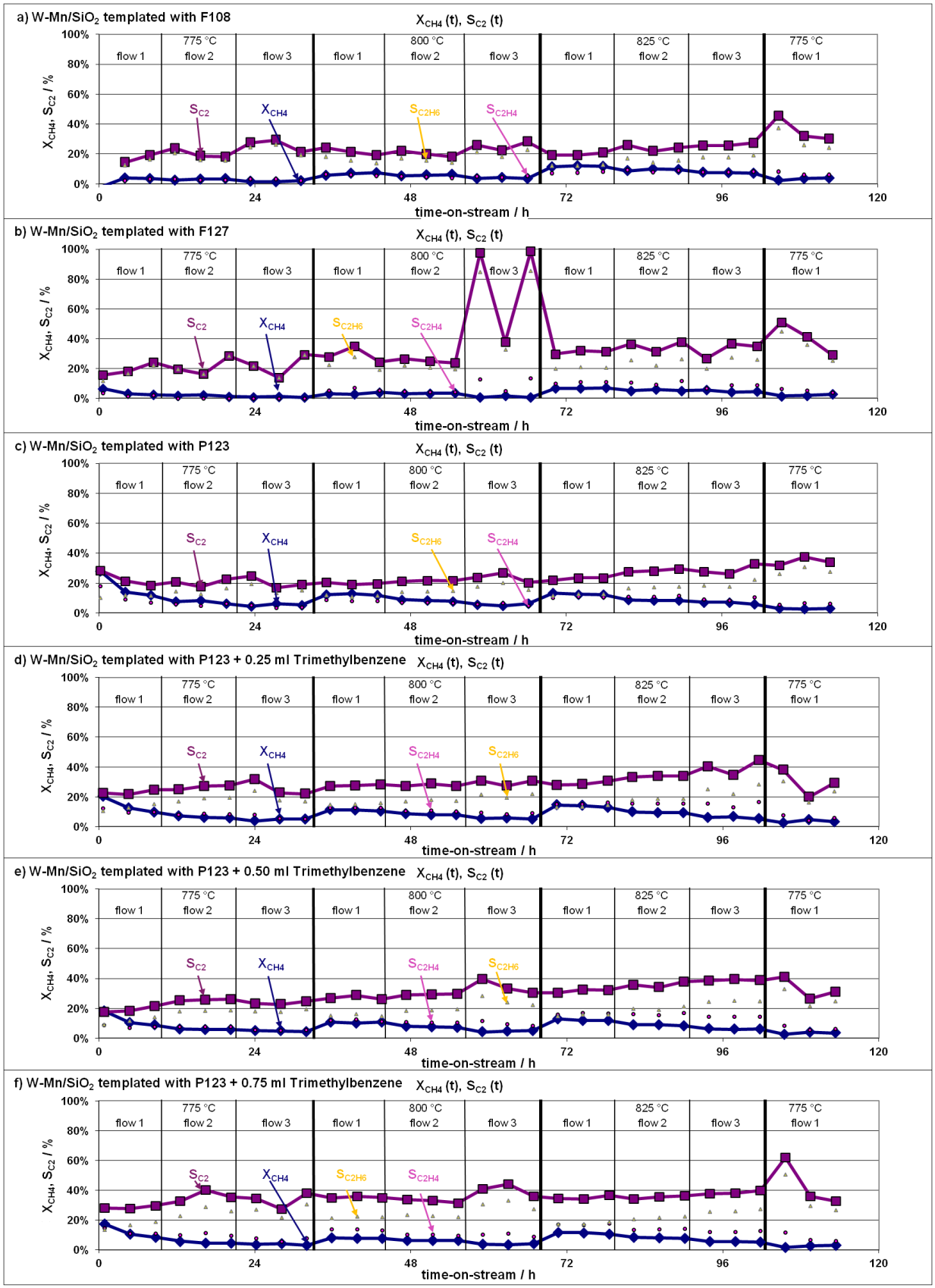

Figure 6.9.: Conversion X_{CH4} (blue squares) and selectivity (C_2 in violet squares, C_2H_6 yellow triangles, C_2H_4 pink circles) OCM results of W-Mn-SiO_2 catalyst templated with a) F108, b) F127, c) P123, d) P123 + 0.25 ml TMB, e) P123 + 0.5 ml TMB and f) P123 + 0.75 ml TMB

The methane conversion increases with higher temperatures for all examined catalysts. This increase of methane conversion can be explained by increasing reaction kinetics caused by higher temperatures.

In contrast to the temperature dependency, the conversion decreases at higher gas flow rates. The decrease of the flow rate increases the contact time of the gas feed at the catalyst. Therefore, more methane can be converted to C_2-products or to undesired CO_x at the same temperature. Therefore, the highest methane conversion for each catalyst is achieved at 825 °C and flow rate 1. At this conditions the catalysts prepared with Brij56 and with P123 and 0.25 ml TMB yielded the highest conversion of 12%. The lowest conversion of 8% is yielded from the W-Mn/SiO_2 structured with F127 at 825 °C and flow rate 1 . The catalysts templated with F108, P123, P123 + 0.5 and 0.75 show the same conversion of about 11%. In general, the low methane conversions of all catalysts indicate the moderate activity of all prepared catalysts.

Furthermore, both ethane and ethylene are observed as selective reaction products for all catalysts. The trends for the tested catalyst of S_{C2H6} and S_{C2H4} are similar to the catalytic results of the catalyst prepared with Brij56. The selectivity towards ethane is higher compared to the ethylene selectivity. S_{C2H6} increases for all catalyst with increasing temperature but decreases with higher flow rates. The highest ethane selectivity of 30% is observed for W-Mn/SiO_2 structured with P123 and 0.75 TMB at 775 °C and flow rate 3. The lowest selectivity of 14% at this condition is measured for the catalyst prepared with F127. The further catalysts show S_{C2H6} between 14% and 29%.

In contrast to the trend of the ethane selectivity, S_{C2H4} decreases with increasing temperature and increases with higher flow rates. The catalyst prepared with P123 and 0.75 ml TMB yields the highest ethylene selectivity with a value of 18% at 825 °C and flow rate 1. The lowest S_{C2H4} of 9% is observed for the catalyst prepared with F108 at the same conditions. The opposing temperature and flow rate dependencies of ethane and ethylene selectivity suggest that C_2H_4 results from the dehydrogenation of C_2H_6 supporting the mechanisms explained in the case of the catalyst prepared with Brij56.

The overall C_2-selectivity follows the trends described on the example of the Brij56 structured W-Mn/SiO_2: S_{C2} increases with higher temperatures and higher flow rates. The C_2-selectivity varies for each catalyst in the range between 12% and 40%. However, the data scatter significantly. In addition, some outliers (for example the catalyst prepared with F127 at 800 °C and flow rate 3) result from insufficient quantification of CO_x and, therefore, underestimation of CO_x selectivities. This leads to unrealistic high C_2-selectivities. Furthermore, a fair comparison of selectivity data is only permitted at the same conversion and temperature. A detailed correlation and discussion of the C_2-selectivities versus the pore diameter of the catalyst is given in section 6.4.

6.3. Reproducibility of Synthesis and Catalysis

The reproducibility of synthesis and catalytic testing is important to gain valid information on how the pore size influences the C_2-selectivity of OCM. The complex synthesis and long and harsh catalysis conditions can scatter the evaluated data significantly. Therefore, the synthesis was repeated applying the previously developed procedure to obtain an additional set of W-Mn/SiO_2 templated with either with F127, Brij56, F108 or P123. These catalysts were tested simultaneously in the same multi-channel fixed bed-reactor applying the same conditions for the OCM test as for the other catalysts to estimate the error bar of combined synthesis and catalysis.

Figure 6.10 presents exemplarily the OCM results of the original Brij56 structured material (a) and of the reproduced catalyst (b). Both catalysts show a similar behaviour in OCM reaction. Both catalysts suffer an initial loss of activity, but stabilise between 3% to 5% methane conversion. Also the reproduced catalyst increases its activity with higher temperatures at similar flow rates compared to the original Brij56 catalyst. Applying a higher flow rate and, therefore, reducing the contact time leads to decreasing methane conversion. After 101 h the starting conditions

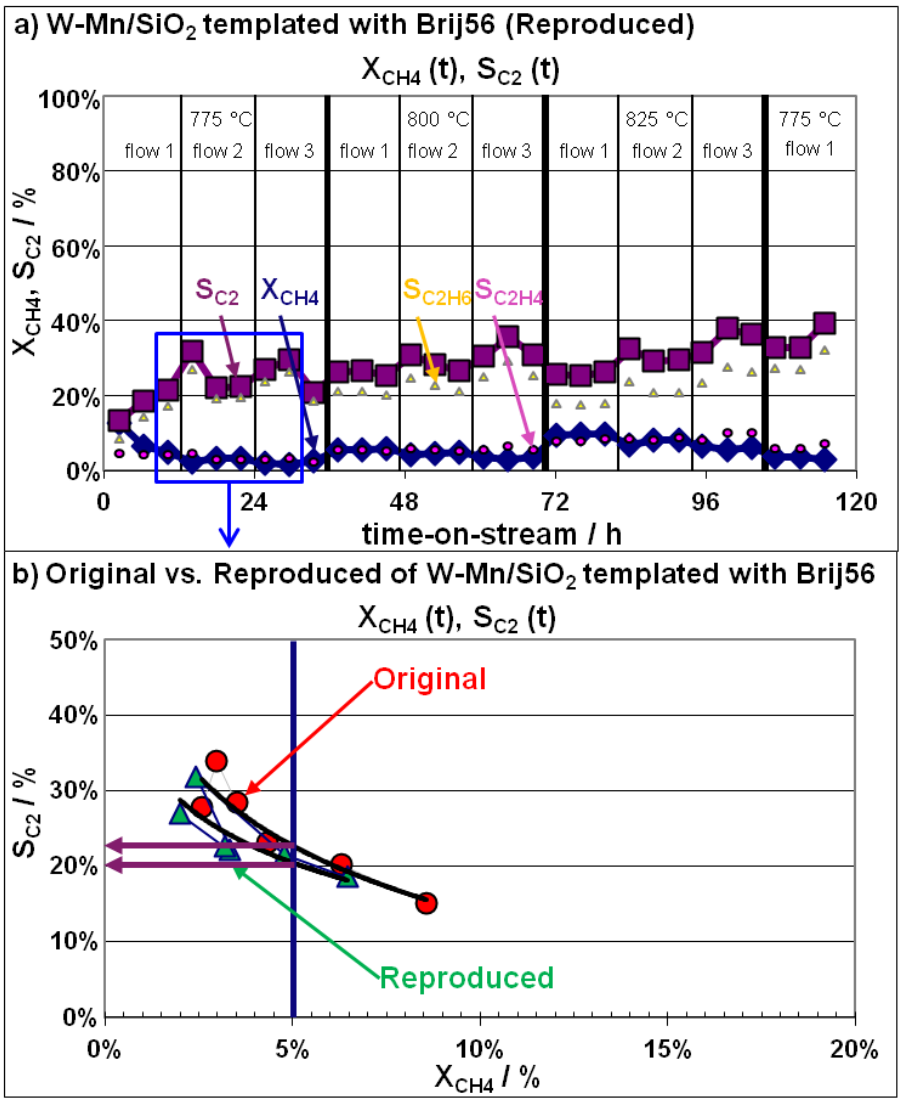

Figure 6.10.: a) methane conversion X_{CH4} (blue squares) and selectivity (S_{C2} violet squares, S_{C2H6} yellow triangles, S_{C2H4} pink circles) versus time-on-stream of the reproduced W-Mn/SiO_2 catalyst prepared with Brij56 recorded at 775 °C, 800 °C and 825 °C with three flow rates (flow 1 < flow 2 < flow 3) at each temperature; the blue frame highlights the data used for the evalution of the reproducibility; b) C_2-selectivity S_{C2} versus methane conversion X_{CH4} for the original (red) and the reproduced (green) catalyst, the violet arrows highlighting the resulting C_2-selectivity obtained at $X_{CH4} = 5\%$ (blue line).

are applied and both catalysts are still active but with a slight loss of activity from about 6% (initially) to 4% (end of test run).

The S_{C2H6} and S_{C2H4} trends of the reproduced catalyst are similar to the catalytic results of the catalyst prepared with Brij56 (see section 6.2). The selectivity towards ethane is in the range of 15% to 30%. The ethylene selectivity is observed in the range of 3% to 10%. Hence, the selectivity towards ethane is higher compared to the ethylene selectivity for both catalysts. However, the reproduced catalyst shows slightly lower ethylene selectivity (6% flow rate 2 at 800 °C) compared to the original catalyst prepared with Brij56 (9% flow rate 2 at 800 °C).

The C_2-selectivity of the reproduced catalyst follows the same trends identified for the original catalyst. The C_2-selectivity increases with higher gas flow rates as well as with higher temperature and is in the range of 15% to 36% for both catalysts.

The quantitative comparison of selectivities should only occur at the same conversion levels. Figure 6.10c) illustrates how the selectivities are extracted from the catalytic data for the comparison of different catalysts in the following section and in this section. The figure plots for both catalysts S_{C2} versus X_{CH4} at 775 °C and gas composition. The variation in methane conversion results from the variation of the flow rate within the first 28 h of the experiment. For each catalyst a logarithmic fit of the curve S vs. X is shown. In the following section, S_{C2} will be compared at X = 5% at 775 °C and 800 °C, respectively.

The comparison of the C_2-selectivities of the original and reproduced catalyst results in S = 22% and S = 20% results, respectively. Hence, the selectivities at the compared conversion level are similar and the combined synthesis and catalysis error bar is only about 2%. Thus, the synthesis and catalysis is reasonable reproducible.

6.4. Correlation between C_2-Selectivity and Pore Diameter

In this section the correlation between C_2-selectivity and pore diameter of the W-Mn/SiO_2 OCM catalyst is analysized. The selectivities of different catalysts can only be fairly compared at the same methan conversion and temperature. Moreover, the C_2-selectivities are only comparable at low methane conversions, because at low conversion the concentration of C_2-products is low and, therefore, sequential overoxidation reactions can be neglected.

The S_{C2} values for each catalyst at 775 °C and 800 °C, respectively, were extracted from the OCM data presented in section 6.2. The C_2-selectivities for each catalyst were plotted against the methane conversion. Thereafter, the selectivity was determined by interpolation to a methane conversion of 5%. The resulting selectivities are correlated with the initial pore diameters given in Figure 6.11. The pore diameters were extracted from the maximum of the NLDFT pore size distribution presented in section 6.1. As an exception, the pore diameter of the catalyst prepared with P123 and 0.75 ml TMB was determined by SEM due to contradictory results of the pore size distribution.

Figure 6.11 presents the C_2-selectivity at a conversion of 5% versus the initial pore size obtained from physisorption of the catalyst structured with F127, Brij56, F108, P123 (original synthesis and reproduced material) as well as the materials obtained by addition of swelling agent in different amounts to P123 at a) 775 °C and b) 800 °C.

The C_2-selectivity at 775 °C (see Figure 6.11a) increases with increasing initial pore diameter from 17% at d_{pore}=3.5 nm to 34% at d_{pore}=18 nm indicating a linear correlation. The trend appears rather robust also when single catalysts e.g. W-Mn/SiO_2 catalyst prepared with F127 or with P123 and 0.75 ml TMB are removed from the plot.

The increase of pore diameter at constant total pore volume of the porous material leads to smaller pore wall area. Considering the wall of the catalyst to be the reactive centre of the oxidation to CO_x a smaller pore surface should lead to a reduced amount of overoxidation products and therefore a higher selectivity towards C_2-products. Hence, the linear correlation between pore diameter and C_2-selectivity supports the assumption of overoxidation at the catalyst surface.

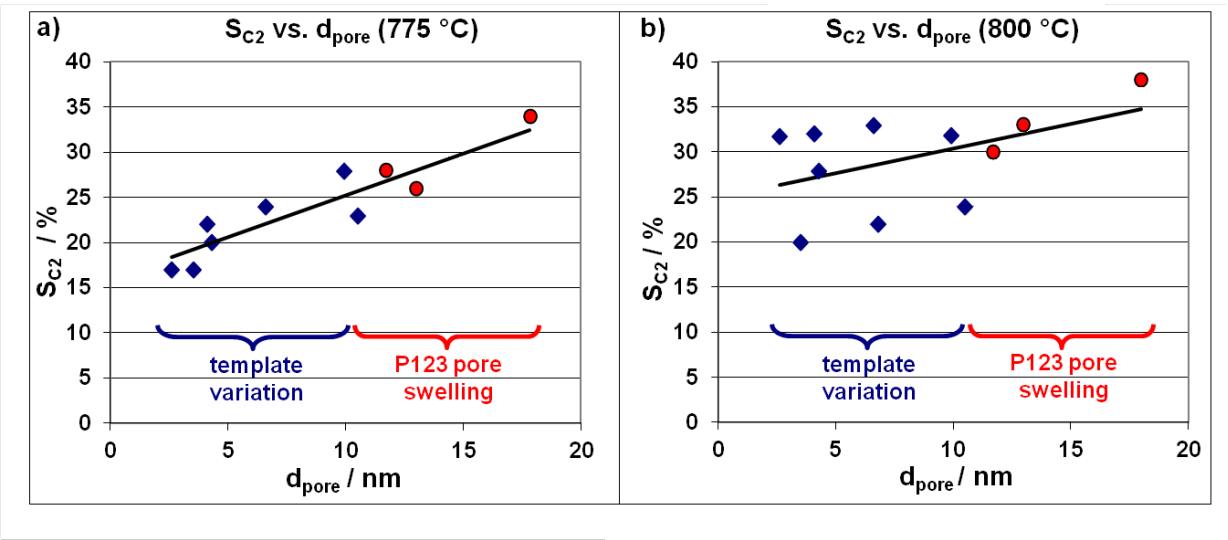

Figure 6.11.: C_2-selectivity at 5% methane conversion in OCM reaction versus the inital pore size of W-Mn/SiO_2 catalyst at a) 775 °C and b) 800 °C

Moreover, these results suggest that the formation of ethane and ethylene occurs by combination of methyl radicals in the gas phase and therefore support the findings in literature.[12]

The C_2-selectivities at 800 °C and 5% methane conversion (see Figure 6.11b) show a slight increase with increasing pore diameter. The smallest pore diameter of 3.5 nm yields a S_{C2} of 32%, while the largest pore diameter of 18 nm yields a selectivity of 37%. However, the data scatter strongly and the trend nearly disappears when the largest or the smallest C_2-selectivity are removed. Therefore, the trend observed at 800 °C is not as robust as the linear correlation obtained at 775 °C.

One possible explanation for the blurring of trend at higher temperature could be the morphological restructuring of the catalysts during the course of OCM. When the OCM data at 800 °C were collected, the catalysts remained under OCM conditions for signigicant longer time (up to 70 h) compared to 775 °C. Therefore, the the restructuring of the catalyst could be further progressed and the influence of the initial pore diameters on the C_2-selectivity less observable. In the next section the morphology and phase composition of the W-Mn/SiO_2 catalyst after 120 h of OCM up to 825 °C is described.

6.5. Catalyst Characterisation after OCM

The catalytic data obtained during 120 h of OCM reaction at temperatures up to 825 °C show an initial loss of activity. This loss suggests restructuring of the catalyst morphology or a change in the composition of the catalyst. Therefore, a structural and compositional analysis of the catalyst after the OCM reaction was performed after separating the catalysts from the SiC powder that was used to cover the catalyst bed in the reactor.

W-Mn/SiO_2 templated with Brij56

Figure 6.12 presents a) SEM image, b) XRD, c) SAXS, d) NLDFT-pore size distribution (with an inset showing N_2-adsorption and desorption isotherms) of the catalyst structured with Brij56 after 120 h of OCM reaction up to 825 °C (note: corresponding data of the freshly prepared catalyst are shown in Figure 6.1).

The SEM image recorded after catalysis (see Figure 6.12a) shows nano crystallites on the surface of the catalyst. No pores are visible. In contrast, the N_2-physisorption experiments indicate a

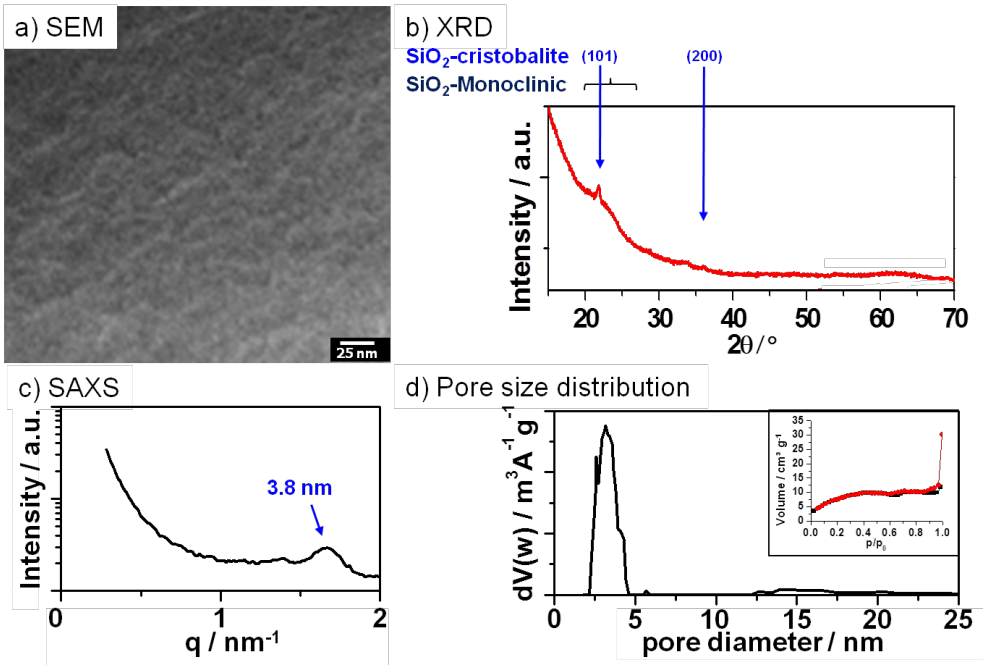

Figure 6.12.: Characterisation of W-Mn/SiO_2 prepared with Brij56 after catalysis by a) SEM, b) XRD, c) SAXS, d) NLDFT-pore size distribution (Quantachrom NLDFT-Modell: N2 at 77K on silica (cylindr./sphere. pore NLDFT ads. Modell) with an inset showing N_2-adsorption (black) and desorption (red) isotherms

narrow pore size distribution (see Figure 6.12d) around 3.2 nm pore diameter. The pore size is slightly smaller compared to the diameter observed for the pristine catalyst (3.9 nm). However, the adsorption and desorption isotherms (see Figure 6.12d inset) show a weak increase of adsorbed gas volume at low relative pressures ($p/p_0 < 0.1$) compared to the freshly prepared catalyst indicating a loss microporosity during OCM. The loss of microporosity is also indicated by the drastically diminished BET surface area from 522 m^2/g of the fresh catalyst to 30 m^2/g after OCM. A small hysteresis loop in the physisorption isotherms between $p/p_0 = 0.6$ and 0.7 indicates the existence of mesopores.

SAXS investigations (see Figure 6.12c) of the used catalyst shows a broad diffraction signal at a value corresponding to a d-spacing of 3.8 nm. Compared to the pristine catalyst with a d-spacing of 5.1 nm the periodical order is smaller indicating contraction of the catalyst pore system. Hence, the pore system, or at least parts of it, is still intact but smaller in size by an isotropic shrinkage of the catalyst.

The composition of the crystalline components were analysed by XRD (see Figure 6.12b) and shows no evidence of tungsten (e.g. cubic WO_3) or manganese (spinel type Mn_3O_4) containing phases which were found beforehand in the pristine catalyst. In contrast, WO_3, Na_2WO_4, NaWSi, $MnWO_4$ and Mn_2O_3 were often reported as crystalline phases in the W-Mn/SiO_2-type catalyst after OCM.[11,12] However, Simon et al. suggested partial melting of the catalyst as origin of the loss of crystallinity during OCM.[30]

In contrast, besides the broad reflex at $2\theta = 24.0°$ corresponding to monoclinic SiO_2 (PDF: 00-039-1425) additional diffraction peaks were found at $2\theta = 21.8°$ and 33.7° indicating the formation of tetragonal α-cristobalite (PDF: 00-039-1425) during catalysis. Cristobalite and quartz are reported to be typical crystalline phases observed at silica based catalyst after OCM testing at temperatures between 750 °C and 850 °C.[12]

Thus, the initial loss in OCM activity can be assumed to result from changes in the phase composition of the catalyst during the first hours of OCM testing. The pore system suffers an isotropic shrinkage but appears to be stable over the course of 120 h up to 825 °C under OCM conditions.

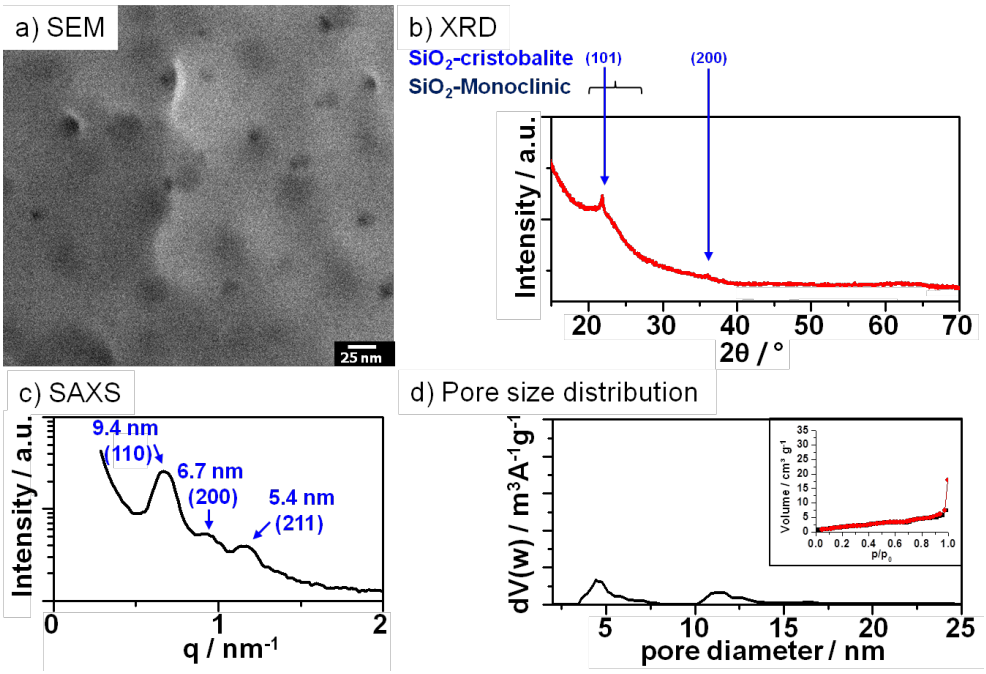

Figure 6.13.: Characterisation of W-Mn/SiO_2 prepared with F108 after catalysis by a) SEM, b) XRD, c) SAXS and d) NLDFT-pore size distribution (Quantachrom NLDFT-Modell: N2 at 77K on silica (cylindr./sphere. pore NLDFT ads. Modell) with an inset showing N_2-adsorption (black) and desorption (red) isotherms

W-Mn/SiO_2 templated with F108

Figure 6.13 presents a) SEM image, b) XRD, c) SAXS and d) NLDFT-pore size distribution (with an inset showing N_2-adsorption and desorption isotherms) of the catalyst structured with F108 after 120 h of OCM reaction up to 825 °C (note: corresponding data for the freshly prepared catalyst is shown in Figure 6.2). The SEM image of the catalyst prepared with F108 (see Figure 6.13a) features round pores in the size range of 10 to 45 nm. Some of the pores seem to be beneath the surface and are blocked towards the surface. The catalyst surface appears unstructured and no crystallites can be observed. The SAXS measurement (see Figure 6.13c) of the used catalyst shows three broad Bragg reflections corresponding to periodical order of 9.4 nm (110), 6.7 nm (200) and 5.4 nm (211) indicating an intact cubic pore system. In comparison with the pristine catalyst, the lattice constant is diminished to 13.4 nm (pristine 15.8 nm). Hence, the pore system or at least parts of it is still intact but reduced in size. The pore size derived from the NLDFT pore size distribution (see Figure 6.13d) is decreased from a pore diameter of 6.8 nm (pristine) to 4.4 nm (used catalyst). An additional local maximum at pore diameters of about 11 nm is shown in the PSD. This additional signal may be an artefact of the calculation on the basis of the physisorption isotherms (see Figure 6.13d inset). The adsorption and desorption isotherms show a very weak increase of gas volume at low relative pressures indicating a strong loss of microporsity during the OCM. No clear hysteresis loop can be observed and the BET surface area is drastically diminished from 358 m^2/g (fresh catalyst) to 8 m^2/g after catalysis. The significant loss of surface area, the smooth appearance of the catalyst measured by SEM and the existence of pore order indicated by SAXS suggest that the pore system is not accessible to the N_2 probe gas. The X-ray diffractogram (see Figure 6.13b) features a broad peak at $2\theta = 24°$ corresponding to monoclinic SiO_2 (PDF: 00-039-1425). Additional peaks at $2\theta = 21.8°$ and 33.7° indicate the formation of tetragonal α-cristobalite (PDF: 00-039-1425) during catalysis. No diffraction signals corresponding to manganese or tungsten containing phases can be detected.

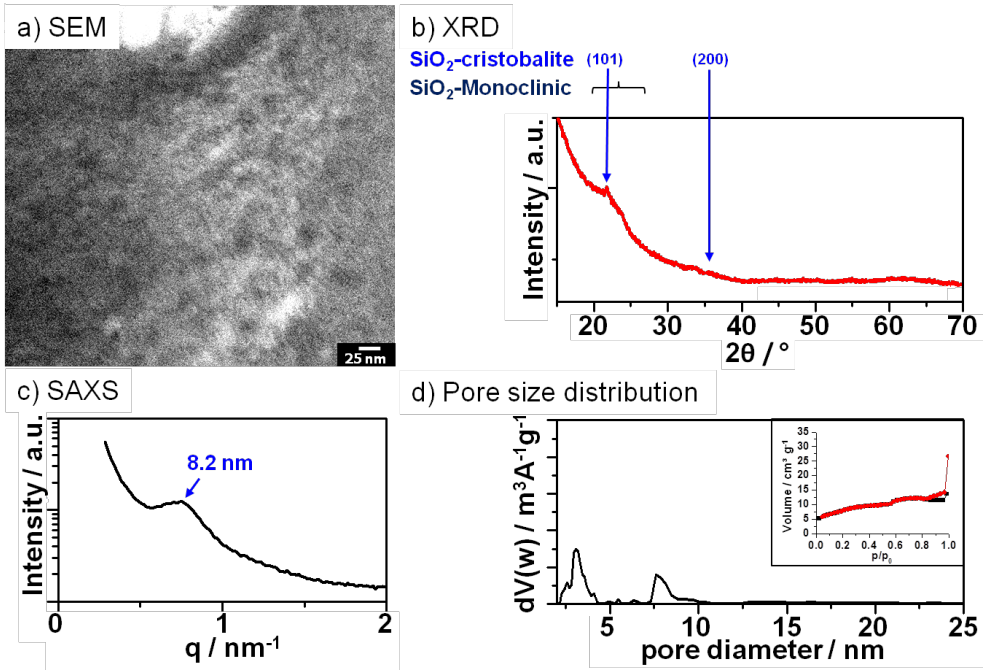

Figure 6.14.: Characterisation of W-Mn/SiO_2 prepared with F127 after catalysis by a) SEM, b) XRD, c) SAXS and d) NLDFT-pore size distribution (Quantachrom NLDFT-Modell: N2 at 77K on silica (cylindr./sphere. pore NLDFT ads. Modell) with an inset showing N_2-adsorption (black) and desorption (red) isotherms

W-Mn/SiO_2 templated with F127

Figure 6.14 presents a) SEM image, b) XRD, c) SAXS and d) NLDFT-pore size distribution (with an inset showing N_2-adsorption and desorption isotherms) of the catalyst structured with F127 after 120 h of OCM reaction up to 825 °C (note: corresponding data for the freshly prepared catalyst are shown in Figure 6.3). The SEM image (see Figure 6.14a) of the catalyst structured with F127 cannot be imaged clearly due to drifts and charging of the sample. However, the SAXS measurements (see Figure 6.14c) showing one broad Bragg reflex corresponding to a d-spacing of 8.2 nm indicating a periodical order of the pore system, suggesting a shrinkage of the pristine material during catalysis. The NLDFT pore size distribution (see Figure 6.14d) shows a maximum corresponding to a pore diameter of 3.1 nm suggesting shrinkage of the pore structure of the pristine mateiral. An additional local maximum is to be seen at a diameter of 5.5 nm. The physisorption isotherms feature a weak increase at low relative pressures indicative for a low amount of microporosity. No clear hysteresis loop is observed. The BET surface area amounts to 28 m^2/g indicating a strong loss of surface area during OCM. The X-ray diffractogram (see Figure 6.14b) features a broad peak at $2\theta = 24°$ corresponding to monoclinic SiO_2 (PDF: 00-039-1425). Additional peaks at $2\theta = 21.8°$ and 33.7° indicate the formation of tetragonal α-cristobalite (PDF: 00-039-1425) during catalysis. No diffraction signals corresponds to manganese or tungsten containing phases.

W-Mn/SiO_2 templated with P123

Figure 6.15 presents a) SEM image, b) XRD, c) SAXS and d) NLDFT-pore size distribution (with an inset showing N_2-adsorption and desorption isotherms) of the catalyst structured with P123 after 120 h of OCM reaction up to 825 °C (note: corresponding data for the freshly prepared catalyst are shown in Figure 6.4). The SEM image (see Figure 6.15a) shows no clear evidence of the pore structure. However, the anisotropic structure of the catalyst surface appears to result from collapsed cylindrical pores. The SAXS measurement (see Figure 6.15c) recorded

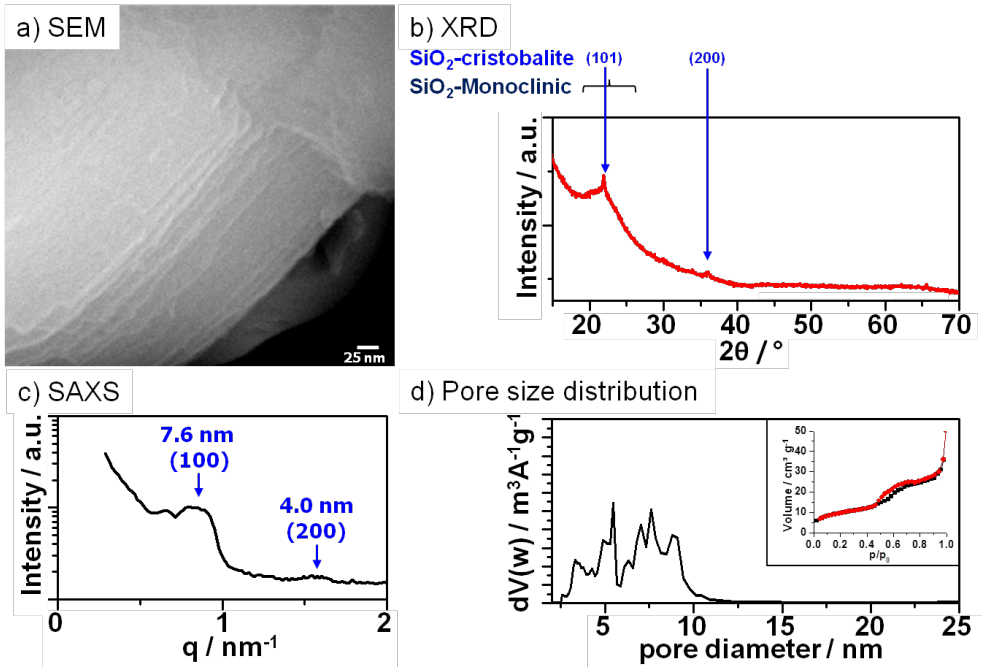

Figure 6.15.: Characterisation of W-Mn/SiO_2 prepared with P123 after catalysis by a) SEM, b) XRD, c) SAXS and d) NLDFT-pore size distribution (Quantachrom NLDFT-Modell: N2 at 77K on silica (cylindr./sphere. pore NLDFT ads. Modell) with an inset showing N_2-adsorption (black) and desorption (red) isotherms

after catalysis shows two broad Bragg diffractions corresponding to 7.6 nm (100) and 4.0 nm (200) indicating a hexagonal pore system with a lattice constant of 9.1 nm. The lattice constant is reduced compared to 11.3 nm of the pristine material suggesting an isotropic shrinkage of the catalyst. The adsorption and desorption isotherms (see Figure 6.15d inset) feature an increase of adsorbed gas volume at low relative presure indicative for remaining microporosity after OCM testing. The physisorption isotherms show a hysteresis loop (H1-type) suggesting the existence of cylindrically shaped mesopores. The BET surface area decreases drastically from 640 m^2/g to 33 m^2/g after OCM. The NLDFT pore size distribution (Figure 6.15d) indicates a broad distribution of remaining pore diameters between 3 to 10 nm. The X-ray diffractogram (see Figure 6.15b) features a broad peak at $2\theta = 24°$ corresponding to monoclinic SiO_2 (PDF: 00-039-1425). Additional peaks at $2\theta = 21.8°$ and 33.7° indicate the formation of tetragonal α-cristobalite (PDF: 00-039-1425) during catalysis. No diffraction signals corresponding to manganese or tungsten containing phases can be detected.

W-Mn/SiO_2 templated with P123 and 0.25 ml TMB

Figure 6.16 presents a) SEM image, b) XRD, c) SAXS and d) NLDFT-pore size distribution (with an inset showing N_2-adsorption and desorption isotherms) of the catalyst structured with P123 and 0.25 ml TMB after 120 h of OCM reaction up to 825 °C (note: corresponding data for the freshly prepared catalyst are shown in Figure 6.5). The SEM image of the materials synthesized with P123 and 0.25 ml TMB (see Figure 6.16a) does not evidence the existence of pores in the material. However, parallel lines on of the catalyst surface could result from collapsed cylindrical pores. The SAXS measurement (see Figure 6.16c) features Bragg reflexes corresponding to d-spacings of 7.6 nm (100) and 4.3 nm (110) indicating remaining pore order though with reduced lattice constants of 8.8 nm. The physisorption isotherms (see Figure 6.16d inset) feature a weak increase of adsorbed gas volume at low relative pressure indicative for remaining microporosity after OCM testing. The isotherms show a H1-type hysteresis loop between $0.4 < p/p_0 < 0.8$

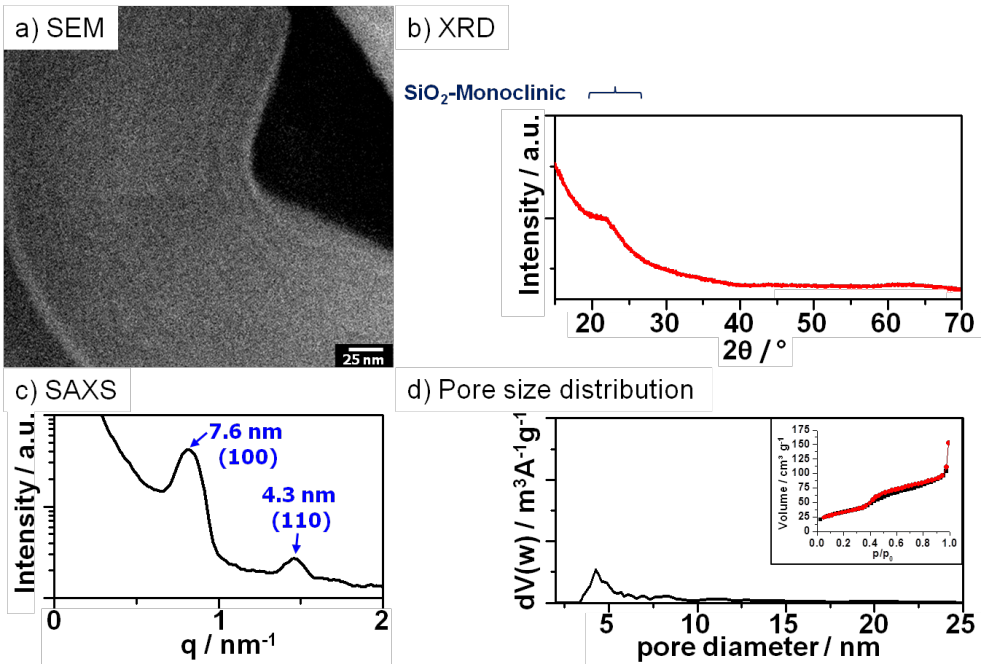

Figure 6.16.: Characterisation of W-Mn/SiO_2 prepared with P123 and 0.25 ml TMB after catalysis by a) SEM, b) XRD, c) SAXS,and d) NLDFT-pore size distribution (Quantachrom NLDFT-Modell: N2 at 77K on silica (cylindr./sphere. pore NLDFT ads. Modell) with an inset showing N_2-adsorption (black) and desorption (red) isotherms

suggesting the presence of cylindrical pores in the used catalyst. The N_2-BET surface area amounts to 118.7 m^2/g indicating a strong loss of internal surface area during OCM. The NLDFT pore size distribution (see Figure 6.16d) features one maximum corresponding to a pore diameter of 4.3 nm. This pore size suggests a strong shrinkage of the pore size and is in agreement with the SAXS results. The X-ray diffractogram (see Figure 6.16b) features a broad peak at $2\theta = 24°$ corresponding to monoclinic SiO_2 (PDF: 00-039-1425). Neither diffraction signals corresponding to manganese or tungsten containing phase nor of the SiO_2 modifications cristobalite or quartz were detected.

W-Mn/SiO_2 templated with P123 and 0.5 ml TMB

Figure 6.17 presents a) SEM image, b) XRD, c) SAXS and d) NLDFT-pore size distribution (with an inset showing N_2-adsorption and desorption isotherms) of the catalyst structured with P123 and 0. 5 ml TMB after 120 h of OCM reaction up to 825 °C (note: corresponding data for the freshly prepared catalyst are shown in Figure 6.6). The SEM image (see Figure 6.17a) of the materials synthesized 0.5 ml TMB does not evidence the existence of pores in the material. The SAXS investigation (Figure 6.17c) shows one broad Bragg reflex which corresponds to d-spacing of 9.0 nm and indicates remaining pore order with diminished periodical distance compared to the fresh catalyst. The adsorption and desorption isotherms (see Figure 6.15d inset) feature an increase of adsorbed gas volume at low relative pressure indicative for remaining microporosity after OCM testing. The physisorption isotherms show a hysteresis loop between 0.48 and 0.98. The loop appear to be a super position of a H1-type ($0.48 < p/p_0 < 0.8$) and a H2-type ($0.8 < p/p_0 < 0.98$) hysteresis indicating a mixture of cylindrical and larger spherical pores, respectively. The principle shape of the hysteresis loop is the same in comparison with the freshly prepared catalyst suggesting that the mesopore system does not change during OCM testing. However, the BET surface area is decreased from 682 m^2/g (fresh catalyst) to 166 m^2/g after OCM testing. The X-ray diffractogram (see Figure 6.17b) features a broad peak at $2\theta = 24°$ corresponding to monoclinic SiO_2 (PDF: 00-

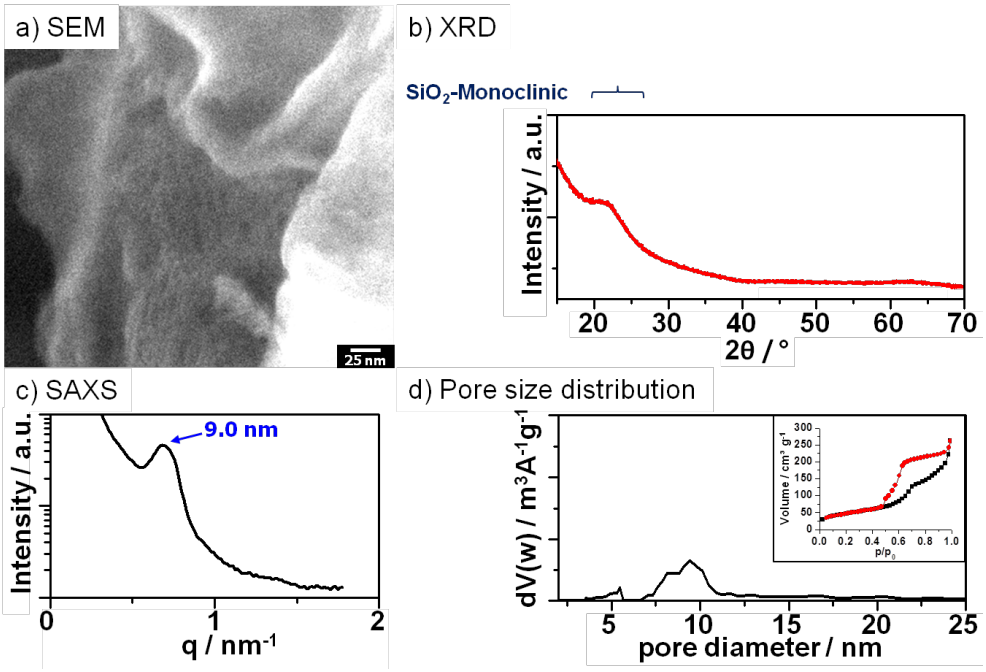

Figure 6.17.: Characterisation of W-Mn/SiO_2 prepared with P123 and 0.5 ml TMB after catalysis by a) SEM, b) XRD, c) SAXS and d) NLDFT-pore size distribution (Quantachrom NLDFT-Modell: N2 at 77K on silica (cylindr./sphere. pore NLDFT ads. Modell) with an inset showing N_2-adsorption (black) and desorption (red) isotherms

039-1425). Neither diffraction signals corresponding to manganese or tungsten containing phase nor of the SiO_2 modifications cristobalite or quartz were detected.

W-Mn/SiO_2 templated with P123 and 0.75 ml TMB

Figure 6.18 presents a) SEM image, b) XRD, c) SAXS and d) NLDFT-pore size distribution (with an inset showing N_2-adsorption and desorption isotherms) of the catalyst structured with P123 and 0.75 ml TMB after 120 h of OCM reaction up to 825 °C (note: corresponding data for the freshly prepared catalyst are shown in Figure 6.7). The SEM image (see Figure 6.18a) of the silica templated with P123 and 0.75 ml TMB shows spherical pores with an average diameter of 10 nm. The SAXS measurement (see Figure 6.18c) of the sample prepared with P123 and 0.75 ml TMB shows a very weak signal corresponding to a d-spacing of 10.7 nm also indicating a shrinkage of the pore system and nearly a loss of pore order. The adsorption and desorption isotherms (see Figure 6.18d inset) show a weak increase of adsorbed gas volume at low relative pressure ($p/p_0 < 0.1$) indicating a remaining amount of intrinsic microporosity. The isotherms feature a hysteresis loop between $0.45 < p/p_0 < 0.98$. The shape of the hysteresis loop can be classified as H1-type hysteresis and is indicative for a cubic pore structure. Further, the existence of the hysteresis loop evidences the existence of accessible mesopores after catalysis. In addition, the BET surface area is decreased during catalysis from 604 m^2/g (fresh catalyst) to 74.1 m^2/g (after OCM). The X-ray diffractogram (see Figure 6.18b) feature a broad peak at $2\theta = 24°$ corresponding to monoclinic SiO_2 (PDF: 00-039-1425). Neither diffraction signals corresponding to manganese or tungsten containing phase nor of the SiO_2 modifications cristobalite or quartz were detected.

In summary, the catalysts show strong morphological and compositional changes between the freshly prepared and the tested catalysts after 120 h of OCM up to 825 °C. The catalyst surface imaged by SEM mostly does not show clear evidence of remaining mesoporosity. However, SAXS measurements suggest remaining pore order, although the periodical distance is decreased probably by shrinkage due to volume loss during catalysis. The XRD does not show any signals

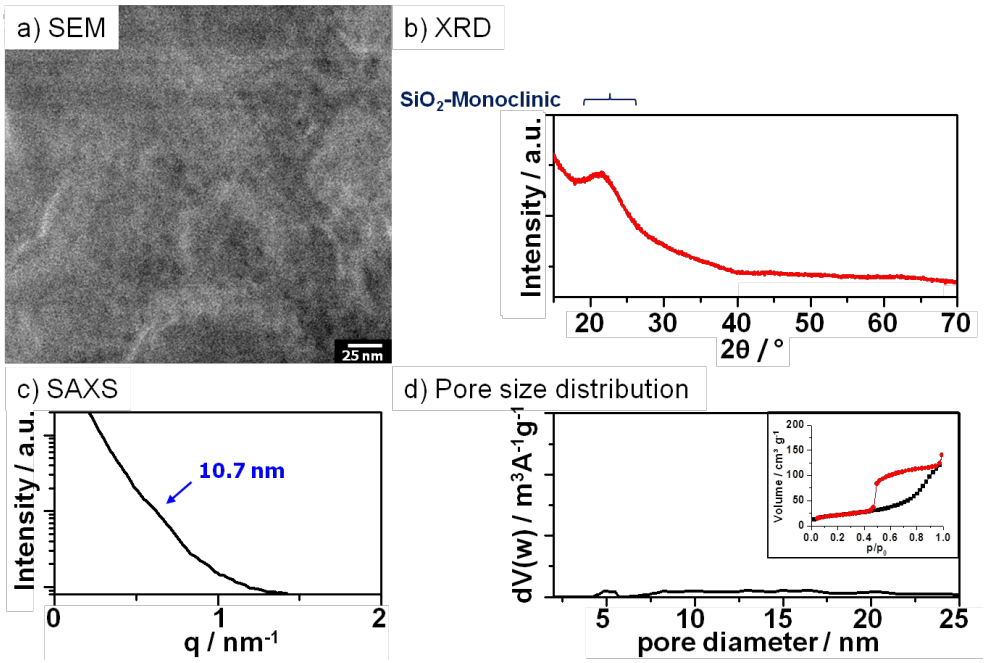

Figure 6.18.: Characterisation of W-Mn/SiO_2 prepared with P123 and 0.75 ml TMB after catalysis by a) SEM, b) XRD, c) SAXS and d) NLDFT-pore size distribution (Quantachrom NLDFT-Modell: N2 at 77K on silica (cylindr./sphere. pore NLDFT ads. Modell) with an inset showing N_2-adsorption (black) and desorption (red) isotherms

corresponding to tungsten or manganese containing phases. However, all catalyst show reflexes indicative for remaining mostly amorphous SiO_2. The catalyst prepared with P123 and swelling agent TMB does not feature Bragg diffraction signals corresponding to further silica modification. The catalyst prepared with Brij56, F108, F127 and P123 feature additional XRD signals indicative for α-cristobalite. This silica phase is often reported to be found as a crystalline phase after OCM.[12]

6.6. Discussion

In this chapter a new synthesis for W-Mn/SiO_2 OCM catalysts with templated porosity was presented and the yielded materials were tested in OCM. The pore size of the catalysts was successfully varied by employing different sized block-copolymers and was further increased by swelling of a P123 template with the swelling agent trimethylbenzene. This variation yields a set of OCM catalysts with pore diameters between 3.5 and 18 nm. The resulting pore sizes and structures of most of the catalysts were in good agreement with the reported results for porous silica SBA.[49,152] Only the catalyst with the smallest (prepared with F127) and largest (prepared with P123 and 0.75 ml TMB) pore diameter yielded significantly different pore diameters compared to the data presented by Zhao et. al.[49,57] Moreover, Zhao et al. did not report a change of the pore structure from hexagonal to cubic when larger amounts of the swelling agent were employed. However, the pore size and structure of the catalyst is not fully comparable to the results of pure silica due to the additional introduction of Na_2WO_4 and $Mn(NO_3)_2$ into the synthesis. Possibly, the tungsten and manganese species interact with the polymer template during the synthesis and influencing the micelle formation resulting in different pore diameters and structures in the final material. This interaction can be investigated by, for example, liquid-phase SAXS but has to be a subject of future investigations.

Tungsten and manganese are present in the crystalline phases WO_3 and Mn_3O_4. These phases are contradictory to the reported crystalline composition mostly observed in W-Mn/SiO_2 OCM

catalyst, although the same precursors Na_2WO_4 and $Mn(NO_3)_2$ were employed in the synthesis. Most of the reported catalysts prepared by wet impregnation observed Na_2WO_4 as crystalline tungsten species on the catalyst surface.[26–28,12,30,11] Only Langfeld et al.[11] reported the presence of WO_3 additionally to sodium tungstate in an OCM active catalyst. This difference of reported materials and the materials presented in this thesis is originated in the applied synthesis procedure. For wet impregnation synthesis sodium tungstate is dissolved in pure water with a pH of nearly seven. However, the synthesis procedure developed in this thesis uses strongly acidic condition to initiate the sol-gel reaction. It is known from textbook[154] that Na_2WO_4 forms polymeric WO_3 at pH < 1.5. Therefore, it was unlikely to indentify Na_2WO_4 in the resulting catalyst. However, the group of Lin and Wang[28] prepared W-Mn/SiO_2 catalysts by a sol-gel route in the presence of HNO_3, but did not mentioned the presence of a WO_3 phase.

In addition, manganese was found in the spinel structure Mn_3O_4 and not in the thermodynamically preferred modification Mn_2O_3 as reported.[26–28,12,30,11] The reason for the less oxidized modification of manganese oxide can probably be originated in the presence of reductive hydrocarbon groups of the polymer template. Moreover, catalysts presented in this thesis were calcined at 600 °C to ensure an calcination unaffected pore system according to Zhao et al.[49,57] However, the catalysts reported by other groups were calcined at elevated temperatures between 800 and 900 °C. These higher temperature can also initiate the formation of Mn_2O_3 as thermodynamically preferred modification.[154]

No crystallisation of SiO_2 occured at the employed calcination temperature. The lower calcination temperature is most probably the reason for the formation of mainly amorphous SiO_2 in the freshly prepared catalyst. In literature, the silica phase in W-Mn/SiO_2 catalysts is reported to consist mainly of α-cristobalite for the freshly prepared catalysts.[26,27,12,30,11] Therefore, α-cristobalite is often discussed as essential for the catalytic activity in the OCM reaction. This assumption is in contrast to OCM testing and characterisation after catalytic testing presented in this thesis.

All prepared catalysts were active in OCM, although they showed mediocre performance with C_2-selectivity between 12 - 40% at methane conversions $< 12\%$. However, the catalyst prepared with P123 and swelling agent (0.25 - 0.75) showed the best OCM performance with C_2-selectivities up to 40%, but did not feature any diffraction signals corresponding to crystalline α-cristobalite. Hence, α-cristobalite is not necessarily essential for a well performing OCM catalyst, although Lin et al. (sol-gel catalyst: $S_{C2}= 69\%$ at $X_{CH4}=22\%$ and 820 °C) and Arndt et al. (wet impregnation: $S_{C2}= 78\%$ at $X_{CH4}=4\%$ and 750 °C) reported higher performance with initially characterized α-cristobalite. In addition, Lin et al. reported stable long time activity of the catalytic performance for 500 h and 820 °C.[28,30] In contrast to this observation, the catalysts presented in this thesis have shown a slight deactivation over 120 h up to 850 °C and a strong initial loss at the beginning of the catalytic test. The reason for these changes in the catalytic performance are most likely originated in morphological and compositional changes occured during OCM testing.

The loss of activity is probably correlated to the strong loss of BET surface area. The decrease in surface area can result in the loss of accessible active sites for the methane activation and, therefore, will result in diminished methane conversion. The surface area is mostly determined by the amount of microporosity in the material, although mesoporosity contribute. One possible explanation for this loss is the transformation of amorphous silica into crystalline α-cristobalite. This transformation was observed for the catalyst prepared with Brij56, F127, F108 and P123. The catalyst at which this transformation was not observed (P123 + 0.25 - 0.75 ml swelling agent) also show significantly less diminished surface area. In addition, Simon et al. suggested partly melting of the catalyst. Molten material could fill micropores or mesopores and diminish the accessibility of the pore network for the reactant gas during catalysis or the probe gas (N_2) during physisorption experiments.

The physisorption experiments indicate significant changes in the templated mesopore structure during catalysis. Especially the catalyst prepared with small mesopores < 10 nm show significantly

changed shapes of the hysteresis loop indicative for the loss of mesoporosity. The catalyst prepared with the larger mesopores with diameters of 10 - 18 nm features a nearly unchanged shape of the hysteresis loop indicating a nearly unaffected mesopore structure.

In contrast to physisorption, the SAXS measurement indicated remaining pore information for all catalysts. This result implies that parts of the pore system were still intact. In comparison with physisorption experiments, SAXS can yield bulk information, while physisorption can only probe the parts of the sample which are accessible for the probe gas. When only the surface of the material was restructured (for example by a melt) the bulk would undergo less structural changes, then SAXS could still evidence the periodical order in the material. However, the degree and the location of the structural changes in the catalysts cannot be ultimately decided from the present data. TEM measurements could enlighten this question, but this remains subject of future investigations.

In addition, for all catalysts the SAXS investigations show a diminished d-spacing of the pore system indicative for a shrinkage of the catalyst during catalysis. This shrinkage occurs due to volume loss of the catalyst powder maybe by dehydration of remaining hydroxide groups of the initial silica. In contrast to layers where the shrinkage occurs unidirectional during calcination due to the contact to the substrate, an isotropic shrinkage can be observed for powders.[49] However, the templated pore information survives at least partly after the OCM testing up to 825 °C.

The influence of the templated mesoporosity correlates to the C_2-selectivity in the OCM reaction. The correlation of S_{C2} with pore diameter at 775 °C and a methane conversion of 5% showed an apparent linear increase of the selectivity with the pore diameter. With increasing pore diameter d the volume per pore increases by a factor of d^3 while the surface area per pore increases only by a factor of d^2. Therefore, the pore volume increases stronger than the pore surface with increasing diameter. Lunsford et al.[4] suggested that the formation of ethane by the combination methyl radicals takes place in the gas phase while the oxidation to CO_x occurs on the catalyst surface. Hence, at higher pore diameters more gas volume for the formation of C_2-products is accessible, while less pore surface area for the overoxidation is available which would diminish the C_2 selectivity. Thus, the observed trend in the correlation of C_2-selectivity versus the pore diameter supports the suggestion of Lunsford. In addition, only an influence of the pore diameter on the C_2-selectivity was distinguished. A dependence of the pore shape could not be observed.

However, the influence of the pore diameter is not the only interpretation that could explain the observed trend of the selectivity. The characterisation of the catalysts after catalysis suggested a dependence of the morphological restructuring of the initial pore diameter. The W-Mn-SiO_2 with largest pore diameters showed less pronounced change in the mesopore structure than the catalysts with smaller mesopores. Therefore, the observed trend of the correlation between C_2-selectivity and the pore diameter at 775 °C is possibly an effect of different equilibration times due to morphological changes. This suggestion is supported by the significantly less pronounced trend of selectivity versus pore diameter observed at 800 °C when the morphological change is further progressed.

In future works, this trend can be verified by OCM test at only 775 °C and fast cool down of the catalyst bed after catalysis. The morphological characterisation of the catalysts at this point can result in information about the structural decay of the pore system at this point.

Moreover, the trend should be further validated by extending the pore size range to smaller and larger pores in the catalyst material. Smaller pores in silica can be templated with smaller templates. This was already shown by the Mobil Company in the MCM-41 materials by employing cetyltrimethylammonium bromid (CTAB) as template.[48] The larger pore diameters in the catalyst could be obtained by employing more swelling agent. However, according to Zhao et al. enlargement of the pores was only investigated up to pore diameters up 32 nm.[49,57] Even larger pores could be obtained by employing larger block-copolymers or polymer latex as template.

In addition, the dependence of the C_2-selectivity on the pore diameter should be investigated on a structurally more stable catalyst to ensure the preservation of the templated pore system

over the whole temperature range between 750 °C and 850 °C. It can be assumed that a SiC matrix instead of SiO_2 is more stable at these elevated temperatures. Therefore, the synthesis of W-Mn/SiC catalyst with templated mesoporosity and testing in OCM reaction could provide more reliable results for the influence of the pore diameter on the C_2-selectivity.

7. Summary and Outlook

The oxidative coupling of methane can contribute to overcome the dependence on fossil oil of many branches of the chemical industry as methane is abundant in natural gas or biogas. However, the mechanistic steps of the reaction are not fully understood, yet. In particular, the role of the pore system in the proposed coupling between surface reaction and radical-based gas phase reaction has not been revealed so far. For the investigation of such effects OCM catalysts with narrow pore size distribution and the ability to control and tune the pore size are required.

Goal of this thesis was the development of synthesis methods to obtain OCM catalysts with template-controlled tuneable mesoporosity. The influence of the templated pore size was evaluated by testing synthesised catalyst in OCM.

The syntheses of ordered mesoporous oxides and OCM catalysts were realized in the form of micelle-templated model systems. The developed synthesis concept is based on chemical complexes formed by metal nitrate and citric acid as a new type of material precursor. This type of precursor helped to overcome limitation of typically employed precursor e.g. insolubility in typical solvents, crystallisation upon drying, melting during calcination or the fast progression of hydrolyse-condensation reaction preventing the formation of the required mesophase. In contrast to the typically employed precursors, the citric acid complex decomposes at first into a structural stable carbonate before transforming into the final oxide material.

The developed synthesis concept consists of the following subsequent steps: First metal nitrate and citric acid form a chemical complex in solution. A micelle structured mesophase is then obtained by co-dissolving the precursor complex with a micelle forming template followed by a coating process. The precursor complex is thereafter transformed into a structural stable carbonate at low temperatures by calcination. The corresponding mesoporous metal carbonate is obtained subsequently by thermal removal of the template. In the last step of the synthesis concept the amorphous carbonate is transformed into a nanocrystalline metal oxide.

The interaction of the citric acid ligand and the metal nitrate was proven by mass spectrometry. By comparison of the decomposition behaviour of the precursor complex and the polymer template, the accessibility of the mesoporous metal carbonate can be predicted as well as optimal calcination conditions. The mesoporous carbonates can only be synthesised when the template decomposes at temperatures where the carbonates are still thermally stable.

Applying the new concept, the synthesis of magnesium, zinc and aluminium carbonates as micelle templated films was successful for the first time. The direct synthesis of cobalt carbonate was not possible, because the carbonate decomposes at lower temperature than the employed template. Moreover, Co_3O_4, MgO and ZnO were obtained as micelle templated layers for the first time applying this new synthesis concept. The additional variation of the pore size by employing different sized templates demonstrated the versatility of the new concept.

The presented synthesis strategy for creating functional metal oxides and carbonates can be easily tuned and optimized for energy storage, electro catalysis, sunlight harvesting or biomedical applications. In particular amorphous $CaCO_3$ could be of interest for biocompatible implant coating and defined model systems in bone cell culturing[155] and biomineralisation research.[156] However, the synthesis should be further refined based on improved fundamental understanding. Physico-chemical investigations could reveal the type of interaction between precursor complex and micelles, guide the tailoring of the complex structure and explain how crystallites are formed. Most importantly, extending the synthesis strategy to yield also bimetallic carbonates and oxides with optimized pore structure such as the Cu/ZnO_x-based catalysts employed in industrial methanol

synthesis[137] or indium-free transparent conductive oxides could result for many applications in a tremendous increase in performance.

After successfully developing a synthesis concept for micelle templated MgO films, the concept was transferred to obtain mesoporous MgO and Li@MgO in the form of powders as OCM catalyst. The synthesis successfully yields MgO and Li@MgO with good precision of the target lithium content. Unfortunately, the analysis of the pore system indicates no pore order. The obtained powders were compared with the untemplated analogous in terms of composition, pore morphology and performance in OCM reaction.

The MgO based powders are active in OCM and yield C_2-products at temperatures > 600 °C. In comparison, the lithium doped MgO shows higher methane conversion and C_2-selectivity at any given temperature. This is in good agreement with the literature. Moreover, all catalysts show significant loss of activity over time-on-stream indicating a restructuring of the catalysts. In the case of Li-containing catalysts also a loss of Li contributes to the observed deactivation. The morphological characterisation of the catalysts after OCM testing confirms a strong crystallite growth and significantly changes in pore structure. Due to these morphological changes the catalysts never fully equilibrate preventing a reliable examination of the pore size influence on MgO based OCM catalyst.

Therefore, a synthesis procedure was developed to introduce controlled porosity into a catalyst system with potentially higher stability. The OCM catalyst system W-Mn/SiO_2 was synthesised by combining a sol-gel approach to introduce the OCM active elements in mesoporous SBA-type silicas. The pore diameters of the obtained materials could be tuned by employing different sized polymer templates as well as by swelling of the Pluronic P123 micelles yielding a pore size range of 3.5 - 18 nm in the composite material. Hence, the pore templating enabled a systematic pore size variation in one OCM catalyst.

The obtained templated powders are active and selective in the OCM reaction. Compared to the literature data the catalysts show a typical performance expected for this catalyst composition. Moreover, the synthesis and the OCM performance show reasonable reproducibility. All the synthesised catalysts show the same typical behaviour under OCM-conditions, i.e. an initial loss of activity followed by equilibration. The stabilisation of the activity at the lowest applied temperature (775 °C) allowed the investigation of the influence of the size of templated mesopores on the observed C_2-selectivity at 5% methane conversion. The extracted data indicate a monotone increase of the selectivity with increasing pore sizes. This increase of selectivity with increasing pore diameter supports the hypothesis of coupling methyl radicals in the gas phase and the formation of CO_x on the catalyst surface.

However, this clear correlation between the size of templated mesopores and S_{C2} was in this thesis studied on only one catalyst composition. The trend has to be validated with different compositions. Moreover, the state of the equilibrated catalyst is not known. Therefore, an additional OCM test at only 775 °C has to be performed to confirm the existence of a stable pore system during the test. Further, the volume to surface ratio is only one possible explanation for the observed selectivity trend. The results should thus be validated on a more stable OCM-catalyst system in the future.

Bibliography

[1] F. Jiao, H. Frei, *Energy & Environmental Science* **2010**, *3*, 1018–1027.

[2] F. F. Abdi, L. H. Han, A. H. M. Smets, M. Zeman, B. Dam, R. van de Krol, *Nature Communications* **2013**, *4*, 2195.

[3] E. Kondratenko, *Proceedings of the DGMK-Conference* **2008**, 45.

[4] T. Ito, J. X. Wang, C. H. Lin, J. H. Lunsford, *Journal of the American Chemical Society* **1985**, *107*, 5062–5068.

[5] C. Sanchez, C. Boissiare, D. Grosso, C. Laberty, L. Nicole, *Chemistry of Materials* **2008**, *20*, 682–737.

[6] G. Ertel, J. Knözinger, J. Weitkamp, *Handbook of Heterogeneous Catalysis*, Wiley-VCH, Weinheim, **1997**.

[7] H. H. Kung, *Catalysis Reviews-Science and Engineering* **1980**, *22*, 235–259.

[8] M. Kamperman, A. Burns, R. Weissgraeber, N. van Vegten, S. C. Warren, S. M. Gruner, A. Baiker, U. Wiesner, *Nano Letters* **2009**, *9*, 2756–2762.

[9] C. K. Narula, J. E. Allison, D. R. Bauer, *Chemistry of Materials* **1996**, *4756*, 984–1003.

[10] J. H. Lunsford, *Angewandte Chemie-International Edition* **1995**, *34*, 970–980.

[11] K. Langfeld, B. Frank, V. E. Strempel, C. Berger-Karin, G. Weinberg, E. V. Kondratenko, R. Schomacker, *Applied Catalysis A-General* **2012**, *417*, 145–152.

[12] S. Arndt, T. Otremba, U. Simon, M. Yildiz, H. Schubert, R. Schomacker, *Applied Catalysis A-General* **2012**, *425*, 53–61.

[13] S. Arndt, G. Laugel, S. Levchenko, R. Horn, M. Baerns, M. Scheffler, R. Schlogl, R. Schomacker, *Catalysis Reviews-Science and Engineering* **2011**, *53*, 424–514.

[14] C. T. Au, K. D. Chen, C. F. Ng, *Applied Catalysis A-General* **1998**, *171*, 283–291.

[15] C. T. Au, X. P. Zhou, Y. W. Liu, W. J. Ji, C. F. Ng, *Journal of Catalysis* **1998**, *174*, 153–163.

[16] V. R. Choudhary, V. H. Rane, S. T. Chaudhari, *Fuel* **2000**, *79*, 1487–1491.

[17] A. Palermo, J. P. H. Vazquez, R. M. Lambert, *Catalysis Letters* **2000**, *68*, 191–196.

[18] Y. Zeng, F. T. Akin, Y. S. Lin, *Applied Catalysis A-General* **2001**, *213*, 33–45.

[19] A. G. Dedov, A. S. Loktev, I. Moiseev, A. Aboukais, J. F. Lamonier, I. N. Filimonov, *Applied Catalysis A-General* **2003**, *245*, 209–220.

[20] E. A. Hazbun, assigned to Arco Chemical **1989**, Patent, US 4791079.

[21] H. Abbas, H. Azzis, E. a. t. H. C. U. Bagherzadeh, N. P. C. (Iran), **2005**.

[22] F. T. Akin, Y. S. Lin, *Catalysis Letters* **2002**, *78*, 239–242.

[23] G. E. Keller, M. M. Bhasin, *Journal of Catalysis* **1982**, *73*, 9–19.

[24] W. Hinsen, M. Baerns, *Chemiker-Zeitung* **1983**, *107*, 223–226.

[25] S. Arndt, U. Simon, S. Heitz, A. Berthold, B. Beck, O. Gorke, J. D. Epping, T. Otremba, Y. Aksu, E. Irran, G. Laugel, M. Driess, H. Schubert, R. Schomacker, *Topics in Catalysis* **2011**, *54*, 1266–1285.

[26] X. . Fang, S. Li, J. Lin, Y. Chu, *Journal of Molecular Catalysis (China)* **1992**, *6*, 427–433.

[27] X. Fang, S. Li, J. Lin, J. Gu, D. Yan, *Journal of Molecular Catalysis (China)* **1992**, *6*, 255–262.

[28] J. X. Wang, L. J. Chou, B. Zhang, H. L. Song, J. Zhao, J. Yang, S. B. Li, *Journal of Molecular Catalysis a-Chemical* **2006**, *245*, 272–277.

[29] S. F. Ji, T. C. Xiao, S. B. Li, C. Z. Xu, R. L. Hou, K. S. Coleman, M. L. H. Green, *Applied Catalysis a-General* **2002**, *225*, 271–284.

[30] U. Simon, O. Gorke, A. Berthold, S. Arndt, R. Schomacker, H. Schubert, *Chemical Engineering Journal* **2011**, *168*, 1352–1359.

[31] F. Raji, M. Pakizeh, *Applied Surface Science* **2013**, *282*, 415–424.

[32] Y. H. Kim, C. M. Kim, I. H. Choi, S. Rengaraj, J. H. Yi, *Environmental Science & Technology* **2004**, *38*, 924–931.

[33] T. Wagner, T. Waitz, J. Roggenbuck, M. Froba, C.-D. Kohl, M. Tiemann, *Thin Solid Films* **2007**, *515*, 8360–8363.

[34] T.-Y. Wei, C.-H. Chen, K.-H. Chang, S.-Y. Lu, C.-C. Hu, *Chemistry of Materials* **2009**, *21*, 3228–3233.

[35] C. Guan, X. Li, Z. Wang, X. Cao, C. Soci, H. Zhang, H. J. Fan, *Advanced materials* **2012**, *24*, 4186–4190.

[36] H. Tuysuz, M. Comotti, F. Schuth, *Chemical communications* **2008**, 4022–4024.

[37] K. S. W. Sing, D. H. Everett, R. A. W. Haul, L. Moscou, R. A. Pierotti, J. Rouquerol, T. Siemieniewska, *Pure and Applied Chemistry* **1985**, *57*, 603–619.

[38] F. Schuth, *Angewandte Chemie-International Edition* **2003**, *42*, 3604–3622.

[39] B. Smarsly, M. Antonietti, *European Journal of Inorganic Chemistry* **2006**, 1111–1119.

[40] E. Ortel, T. Reier, P. Strasser, R. Kraehnert, *Chemistry of Materials* **2011**, *23*, 3201–3209.

[41] D. Grosso, G. Soler-Illia, E. L. Crepaldi, F. Cagnol, C. Sinturel, A. Bourgeois, A. Brunet-Bruneau, H. Amenitsch, P. A. Albouy, C. Sanchez, *Chemistry of Materials* **2003**, *15*, 4562–4570.

[42] S. Lepoutre, B. Julin-Lopez, C. Sanchez, H. Amenitsch, M. Linden, D. Grosso, *Journal of Materials Chemistry* **2010**, *20*, 537.

[43] M. Scharrer, X. Wu, a. Yamilov, H. Cao, R. P. H. Chang, *Applied Physics Letters* **2005**, *86*, 151113.

[44] D. Ramirez, P. Bartlett, M. Abdelsalam, H. Gomez, D. Lincot, *Physica Status Solidi (a)* **2008**, *205*, 2365–2370.

[45] X. Xia, J. Tu, J. Zhang, X. Huang, X. Wang, X. Zhao, *Electrochimica Acta* **2010**, *55*, 989–994.

[46] B. Duan, Q. Cao, *Electrochimica Acta* **2012**, *64*, 154–161.

[47] P. Innocenzi, L. Malfatti, G. J. A. A. Soler-Illia, *Chemistry of Materials* **2011**, *23*, 2501–2509.

[48] J. S. Beck, J. C. Vartuli, W. J. Roth, M. E. Leonowicz, C. T. Kresge, K. D. Schmitt, C. T. W. Chu, D. H. Olson, E. W. Sheppard, S. B. McCullen, J. B. Higgins, J. L. Schlenker, *Journal of the American Chemical Society* **1992**, *114*, 10834–10843.

[49] D. Y. Zhao, Q. S. Huo, J. L. Feng, B. F. Chmelka, G. D. Stucky, *Journal of the American Chemical Society* **1998**, *120*, 6024–6036.

[50] F. Kleitz, S. H. Choi, R. Ryoo, *Chemical Communications* **2003**, 2136–2137.

[51] M. Kang, S. H. Yi, H. I. Lee, J. E. Yie, J. M. Kim, *Chemical Communications* **2002**, 1944–1945.

[52] R. Ryoo, S. H. Joo, M. Kruk, M. Jaroniec, *Advanced Materials* **2001**, *13*, 677–681.

[53] S. Jun, S. H. Joo, R. Ryoo, M. Kruk, M. Jaroniec, Z. Liu, T. Ohsuna, O. Terasaki, *Journal of the American Chemical Society* **2000**, *122*, 10712–10713.

[54] D. Gu, F. Schuth, *Chemical Society Reviews* **2013**, *43*, 313–344.

[55] J. X. Li, W. L. Dai, K. Fan, *Journal of Physical Chemistry C* **2008**, *112*, 17657–17663.

[56] H. Tuysuz, C. W. Lehmann, H. Bongard, B. Tesche, R. Schmidt, F. Schuth, *Journal of the American Chemical Society* **2008**, *130*, 11510–11517.

[57] D. Y. Zhao, J. L. Feng, Q. S. Huo, N. Melosh, G. H. Fredrickson, B. F. Chmelka, G. D. Stucky, *Science* **1998**, *279*, 548–552.

[58] J. Fan, S. W. Boettcher, G. D. Stucky, *Chemistry of Materials* **2006**, *18*, 6391–6396.

[59] E. L. Crepaldi, G. Soler-Illia, D. Grosso, M. Sanchez, *New Journal of Chemistry* **2003**, *27*, 9–13.

[60] T. J. Ha, H. H. Park, E. S. Kang, S. Shin, H. H. Cho, *Journal of Colloid and Interface Science* **2010**, *345*, 120–124.

[61] J. Joo, J. Shim, H. Seo, N. Jug, U. Wiesner, J. Lee, S. Jeon, *Analytical Chemistry* **2010**, *82*, 3032–3037.

[62] J. Lee, M. C. Orilall, S. C. Warren, M. Kamperman, F. J. Disalvo, U. Wiesner, *Nature Materials* **2008**, *7*, 222–228.

[63] M. Groenewolt, T. Brezesinski, H. Schlaad, M. Antonietti, P. W. Groh, B. Ivan, *Advanced Materials* **2005**, *17*, 1158.

[64] T. Brezesinski, M. Groenewolt, M. Antonietti, B. Smarsly, *Angewandte Chemie-International Edition* **2006**, *45*, 781–784.

[65] Y. D. Wang, T. Brezesinski, M. Antonietti, B. Smarsly, *ACS Nano* **2009**, *3*, 1373–1378.

[66] E. Ortel, A. Fischer, L. Chuenchom, J. Polte, F. Emmerling, B. Smarsly, R. Kraehnert, *Small* **2012**, *8*, 298–309.

[67] M. Kuemmel, J. H. Smatt, C. Boissiere, L. Nicole, C. Sanchez, M. Linden, D. Grosso, *Journal of Materials Chemistry* **2009**, *19*, 3638–3642.

[68] K. Yu, A. J. Hurd, A. Eisenberg, C. J. Brinker, *Langmuir* **2001**, *17*, 7961–7965.

[69] B. Smarsly, G. Xomeritakis, K. Yu, N. G. Liu, H. Y. Fan, R. A. Assink, C. A. Drewien, W. Ruland, C. J. Brinker, *Langmuir* **2003**, *19*, 7295–7301.

[70] K. Yu, B. Smarsly, C. J. Brinker, *Advanced Functional Materials* **2003**, *13*, 47–52.

[71] E. Bloch, P. L. Llewellyn, T. Phan, D. Bertin, V. Hornebecq, *Chemistry of Materials* **2009**, *21*, 48–55.

[72] J. Y. Zhang, Y. H. Deng, D. Gu, S. T. Wang, L. She, R. C. Che, Z. S. Wang, B. Tu, S. H. Xie, D. Y. Zhao, *Advanced Energy Materials* **2011**, *1*, 241–248.

[73] L. Cao, H. C. Dong, L. Huang, K. Matyjaszewski, M. Kruk, *Adsorption-Journal of the International Adsorption Society* **2009**, *15*, 156–166.

[74] X. X. Liu, Y. Hua, G. Villemure, *Microporous and Mesoporous Materials* **2009**, *117*, 317–325.

[75] E. L. Crepaldi, G. Soler-Illia, D. Grosso, P. A. Albouy, C. Sanchez, *Chemical Communications* **2001**, 1582–1583.

[76] S. Sokolov, E. Ortel, R. Kraehnert, *Materials Research Bulletin* **2009**, *44*, 2222–2227.

[77] C. J. Brinker, Y. Lu, A. Sellinger, H. Fan, *Advanced Materials* **1999**, *11*, 579–585.

[78] Y. Y. Won, H. T. Davis, F. S. Bates, *Macromolecules* **2003**, *36*, 953–955.

[79] S. Jain, M. H. E. Dyrdahl, X. Gong, L. E. Scriven, F. S. Bates, *Macromolecules* **2008**, *41*, 3305–3316.

[80] G. Riess, *Progress in Polymer Science* **2003**, *28*, 1107–1170.

[81] M. Luechinger, G. D. Pirngruber, B. Lindlar, P. Laggner, R. Prins, *Microporous and Mesoporous Materials* **2005**, *79*, 41–52.

[82] H. Yang, A. Kuperman, N. Coombs, S. Mamiche-Afara, G. A. Ozin, *Nature* **1996**, *379*, 703–705.

[83] T. Brezesinski, J. Wang, J. Polleux, B. Dunn, S. H. Tolbert, *Journal of the American Chemical Society* **2009**, *131*, 1802–1809.

[84] Y. F. Lu, R. Ganguli, C. A. Drewien, M. T. Anderson, C. J. Brinker, W. L. Gong, Y. X. Guo, H. Soyez, B. Dunn, M. H. Huang, J. I. Zink, *Nature* **1997**, *389*, 364–368.

[85] W. Q. Cai, J. G. Yu, C. Anand, A. Vinu, M. Jaroniec, *Chemistry of Materials* **2011**, *23*, 1147–1157.

[86] X. M. Wu, H. Q. Cao, G. Yin, J. F. Yin, Y. X. Lu, B. J. Li, *Physical Chemistry Chemical Physics* **2011**, *13*, 5047–5052.

[87] S. Polarz, A. V. Orlov, F. Schuth, A. H. Lu, *Chemistry-a European Journal* **2007**, *13*, 592–597.

[88] P. D. Yang, D. Y. Zhao, D. I. Margolese, B. F. Chmelka, G. D. Stucky, *Chemistry of Materials* **1999**, *11*, 2813–2826.

[89] G. J. A. A. Soler-Illia, P. C. Angelome, M. C. Fuertes, D. Grosso, C. Boissiere, *Nanoscale* **2012**, *4*, 2549–2566.

[90] J. H. Pan, X. S. Zhao, W. I. Lee, *Chemical Engineering Journal* **2011**, *170*, 363–380.

[91] E. L. Crepaldi, G. Soler-Illia, A. Bouchara, D. Grosso, D. Durand, C. Sanchez, *Angewandte Chemie-International Edition* **2003**, *42*, 347.

[92] P. D. Yang, D. Y. Zhao, D. I. Margolese, B. F. Chmelka, G. D. Stucky, *Nature* **1998**, *396*, 152–155.

[93] L. L. Hench, J. K. West, *Chemical Reviews* **1990**, *90*, 33–72.

[94] S. C. Warren, L. C. Messina, L. S. Slaughter, M. Kamperman, Q. Zhou, S. M. Gruner, F. J. DiSalvo, U. Wiesner, *Science* **2008**, *320*, 1748–1752.

[95] C. Weidmann, K. Brezesinski, C. Suchomski, K. Tropp, N. Grosser, J. Haetge, B. M. Smarsly, T. Brezesinski, *Chemistry of Materials* **2012**, *24*, 486–494.

[96] I. E. Rauda, R. Buonsanti, L. C. Saldarriaga-Lopez, K. Benjauthrit, L. T. Schelhas, M. Stefik, V. Augustyn, J. Ko, B. Dunn, U. Wiesner, D. J. Milliron, S. H. Tolbert, *ACS nano* **2012**, *6*, 6386–6399.

[97] Y. J. Liu, G. Stefanic, J. Rathousky, O. Hayden, T. Bein, D. Fattakhova-Rohlfing, *Chemical Science* **2012**, *3*, 2367–2374.

[98] D. Grosso, F. Cagnol, G. Soler-Illia, E. L. Crepaldi, H. Amenitsch, A. Brunet-Bruneau, A. Bourgeois, C. Sanchez, *Advanced Functional Materials* **2004**, *14*, 309–322.

[99] G. Wanka, H. Hoffmann, W. Ulbricht, *Macromolecules* **1994**, *27*, 4145–4159.

[100] D. Grosso, F. Babonneau, P. A. Albouy, H. Amenitsch, A. R. Balkenende, A. Brunet-Bruneau, J. Rivory, *Chemistry of Materials* **2002**, *14*, 931–939.

[101] D. Grosso, *Journal of Materials Chemistry* **2011**, *21*, 17033–17038.

[102] C. Sassoye, C. Laberty, H. Le Khanh, S. Cassaignon, C. Boissiere, M. Antonietti, C. Sanchez, *Advanced Functional Materials* **2009**, *19*, 1922–1929.

[103] D. Grosso, C. Boissiere, L. Nicole, C. Sanchez, *Journal of Sol-Gel Science and Technology* **2006**, *40*, 141–154.

[104] T. Brezesinski, M. Antonietti, M. Groenewolt, N. Pinna, B. Smarsly, *New Journal of Chemistry* **2005**, *29*, 237–242.

[105] Q. S. Huo, D. I. Margolese, U. Ciesla, P. Y. Feng, T. E. Gier, P. Sieger, R. Leon, P. M. Petroff, F. Schuth, G. D. Stucky, *Nature* **1994**, *368*, 317–321.

[106] G. S. Attard, J. C. Glyde, C. G. Goltner, *Nature* **1995**, *378*, 366–368.

[107] F. Schuth, *Chemistry of Materials* **2001**, *13*, 3184–3195.

[108] Q. Yuan, A. X. Yin, C. Luo, L. D. Sun, Y. W. Zhang, W. T. Duan, H. C. Liu, C. H. Yan, *Journal of the American Chemical Society* **2008**, *130*, 3465–3472.

[109] D. M. Antonelli, J. Y. Ying, *Angewandte Chemie-International Edition* **1995**, *34*, 2014–2017.

[110] D. T. On, *Langmuir* **1999**, *15*, 8561–8564.

[111] F. Schuth, U. Ciesla, S. Schacht, M. Thieme, Q. Huo, G. Stucky, *Materials Research Bulletin* **1999**, *34*, 483–494.

[112] P. Liu, I. L. Moudrakovski, J. Liu, A. Sayari, *Chemistry of Materials* **1997**, *9*, 2513–2520.

[113] D. M. Antonelli, J. Y. Ying, *Angewandte Chemie-International* **1996**, *35*, 426–430.

[114] D. M. Antonelli, A. Nakahira, J. Y. Ying, *Inorganic Chemistry* **1996**, *35*, 3126–3136.

[115] D. M. Antonelli, J. Y. Ying, *Chemistry of Materials* **1996**, *8*, 874–881.

[116] U. Ciesla, D. Demuth, R. Leon, P. Petroff, G. Stucky, K. Unger, F. Schuth, *Journal of the Chemical Society-Chemical Communications* **1994**, 1387–1388.

[117] A. Stein, M. Fendorf, T. P. Jarvie, K. T. Mueller, A. J. Benesi, T. E. Mallouk, *Chemistry of Materials* **1995**, *7*, 304–313.

[118] J. A. Martens, J. Jammaer, S. Bajpe, A. Aerts, Y. Lorgouilloux, C. E. A. Kirschhock, *Microporous and Mesoporous Materials* **2011**, *140*, 2–8.

[119] G. S. Armatas, A. P. Katsoulidis, D. E. Petrakis, P. J. Pomonis, M. G. Kanatzidis, *Chemistry of Materials* **2010**, *22*, 5739–5746.

[120] B. Z. Tian, X. Y. Liu, L. A. Solovyov, Z. Liu, H. F. Yang, Z. D. Zhang, S. H. Xie, F. Q. Zhang, B. Tu, C. Z. Yu, O. Terasaki, D. Y. Zhao, *Journal of the American Chemical Society* **2003**, *126*, 865–875.

[121] Y. Q. Wang, C. M. Yang, W. Schmidt, B. Spliethoff, E. Bill, F. Schuth, *Advanced Materials* **2005**, *17*, 53.

[122] B. Z. Tian, X. Y. Liu, H. F. Yang, S. H. Xie, C. Z. Yu, B. Tu, D. Y. Zhao, *Advanced Materials* **2003**, *15*, 1370.

[123] K. Jiao, B. Zhang, B. Yue, Y. Ren, S. X. Liu, S. R. Yan, C. Dickinson, W. Z. Zhou, H. Y. He, *Chemical Communications* **2005**, 5618–5620.

[124] W. Yue, W. Z. Zhou, *Chemistry of Materials* **2007**, *19*, 2359–2363.

[125] X. Y. Lai, X. T. Li, W. C. Geng, J. C. Tu, J. X. Li, S. L. Qiu, *Angewandte Chemie-International Edition* **2007**, *46*, 738–741.

[126] B. Yue, H. L. Tang, Z. P. Kong, K. Zhu, C. Dickinson, W. Z. Zhou, H. Y. He, *Chemical Physics Letters* **2005**, *407*, 83–86.

[127] H. F. Yang, Q. H. Shi, B. Z. Tian, Q. Y. Lu, F. Gao, S. H. Xie, J. Fan, C. Z. Yu, B. Tu, D. Y. Zhao, *Journal of the American Chemical Society* **2003**, *125*, 4724–4725.

[128] J. Roggenbuck, M. Tiemann, *Journal of the American Chemical Society* **2005**, *127*, 1096–1097.

[129] J. Roggenbuck, G. Koch, M. Tiemann, *Chemistry of Materials* **2006**, *18*, 4151–4156.

[130] A. H. Lu, W. Schmidt, A. Taguchi, B. Spliethoff, B. Tesche, F. Schuth, *Angewandte Chemie-International Edition* **2002**, *41*, 3489.

[131] M. Kuemmel, D. Grosso, C. Boissiere, B. Smarsly, T. Brezesinski, P. a. Albouy, H. Amenitsch, C. Sanchez, *Angewandte Chemie-International Edition* **2005**, *44*, 4589–4592.

[132] P. Kim, Y. Kim, C. Kim, H. Kim, Y. Park, J. H. Lee, I. K. Song, J. Yi, *Catalysis Letters* **2003**, *89*, 185–192.

[133] J. Schaep, C. Vandecasteele, B. Peeters, J. Luyten, C. Dotremont, D. Roels, *Journal of Membrane Science* **1999**, *163*, 229–237.

[134] Z. Ecsedi, I. Lazau, C. Pacurariu, *Processing and Application of Ceramics* **2007**, *1-2*, 5–9.

[135] W. D. Yu, X. M. Li, X. D. Gao, *Applied Physics Letters* **2004**, *84*, 2658–2660.

[136] C. C. Li, X. M. Yin, T. H. Wang, H. C. Zeng, *Chemistry of Materials* **2009**, *21*, 4984–4992.

[137] M. Behrens, F. Studt, I. Kasatkin, S. Kuehl, M. Haevecker, F. Abild-Pedersen, S. Zander, F. Girgsdies, P. Kurr, B.-L. Kniep, M. Tovar, R. W. Fischer, J. K. Norskov, R. Schloegl, *Science* **2012**, *336*, 893–897.

[138] Y.-B. Hahn, *Korean Journal of Chemical Engineering* **2011**, *28*, 1797–1813.

[139] X. D. Bai, P. X. Gao, Z. L. Wang, E. G. Wang, *Applied Physics Letters* **2003**, *82*, 4806.

[140] G. Zheng, F. Patolsky, Y. Cui, W. U. Wang, C. M. Lieber, *Nature biotechnology* **2005**, *23*, 1294–1301.

[141] X. F. Duan, C. M. Niu, V. Sahi, J. Chen, J. W. Parce, S. Empedocles, J. L. Goldman, *Nature* **2003**, *425*, 274–278.

[142] Z. L. Wang, *Journal of Physics: Condensed Matter* **2004**, *16*, R829–R858.

[143] D. Esken, H. Noei, Y. Wang, C. Wiktor, S. Turner, G. Van Tendeloo, R. a. Fischer, *Journal of Materials Chemistry* **2011**, *21*, 5907.

[144] P. Poizot, S. Laruelle, S. Grugeon, L. Dupont, J. M. Tarascon, *Nature* **2000**, *407*, 496–499.

[145] K. T. Nam, D.-W. Kim, P. J. Yoo, C.-Y. Chiang, N. Meethong, P. T. Hammond, Y.-M. Chiang, A. M. Belcher, *Science* **2006**, *312*, 885–888.

[146] B.-C. Yu, J.-O. Lee, J. H. Song, C.-M. Park, C. K. Lee, H.-J. Sohn, *Journal of Solid State Electrochemistry* **2012**, *16*, 2631–2638.

[147] M. W. Kanan, D. G. Nocera, *Science* **2008**, *321*, 1072–1075.

[148] Y. Liang, Y. Li, H. Wang, J. Zhou, J. Wang, T. Regier, H. Dai, *Nature Materials* **2011**, *10*, 780–786.

[149] G. C. Li, Y. Q. Liu, L. L. Guan, X. F. Hu, C. G. Liu, *Materials Research Bulletin* **2012**, *47*, 1073–1079.

[150] U. Chellam, Z. P. Xu, H. C. Zeng, *Chemistry of Materials* **2000**, *12*, 650–658.

[151] S. Arndt, U. Simon, S. Heitz, A. Berthold, B. Beck, O. Gorke, J. D. Epping, T. Otremba, Y. Aksu, E. Irran, G. Laugel, M. Driess, H. Schubert, R. Schomacker, *Topics in Catalysis* **2011**, *54*, 1266–1285.

[152] Z. W. Jin, X. D. Wang, X. G. Cui, *Journal of Colloid and Interface Science* **2007**, *307*, 158–165.

[153] S. S. Soni, G. Brotons, M. Bellour, T. Narayanan, A. Gibaud, *Journal of Physical Chemistry B* **2006**, *110*, 15157–15165.

[154] A. Holleman, E. Wiberg, N. Wiberg, *Lehrbuch der Anorganischen Chemie*, *Vol. 91.-100.*, Walter de Gruyter, Berlin-New York, **1985**.

[155] D. C. Popescu, E. N. M. van Leeuwen, N. A. A. Rossi, S. J. Holder, J. A. Jansen, N. Sommerdijk, *Angewandte Chemie-International Edition* **2006**, *45*, 1762–1767.

[156] H. Colfen, S. Mann, *Angewandte Chemie-International Edition* **2003**, *42*, 2350–2365.

A. Appendix

Characterisation of Citric Acid Complexes with Metal Nitrates

Precursor Complex Characterisation by ESI-MS

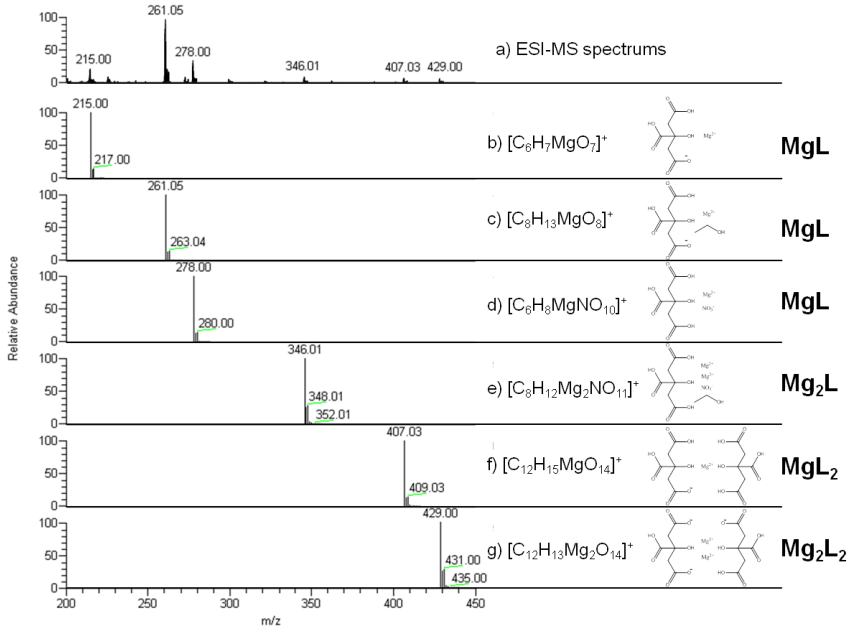

Figure A.1.: Electrospray ionization mass spectrometry analysis of a mixture of $Mg(NO_3)_2$ and citric acid in ethanol. a) ESI-mass spectrum recorded in cation mode and b - g) calculated MS-spectra of the corresponding mass fragments as well as the stoichiometry for magnesium and citric acid ligand (L).

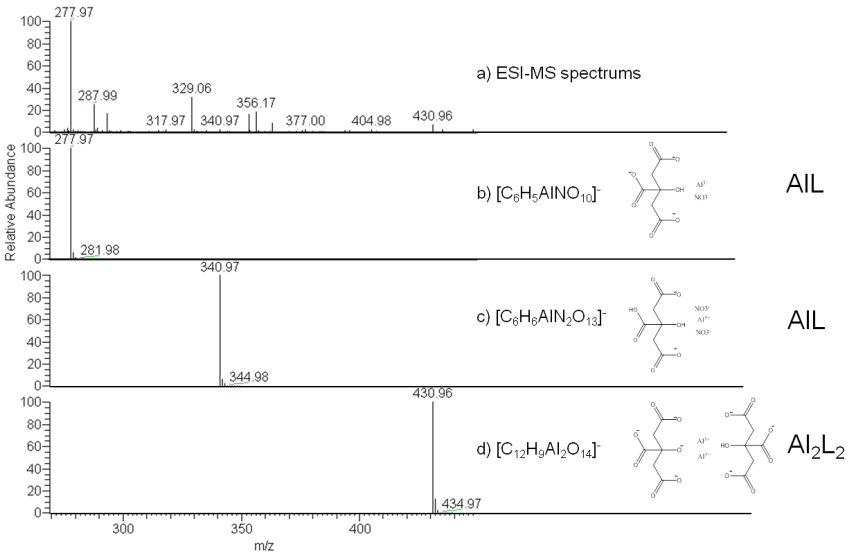

Figure A.2.: Electrospray ionization mass spectrometry analysis of a mixture of $Al(NO_3)_3$ and citric acid in ethanol. a) ESI-mass spectrum recorded in anion mode and b - d) calculated MS-spectra of the corresponding mass fragments as well as the stoichiometry for aluminum and citric acid ligand (L).

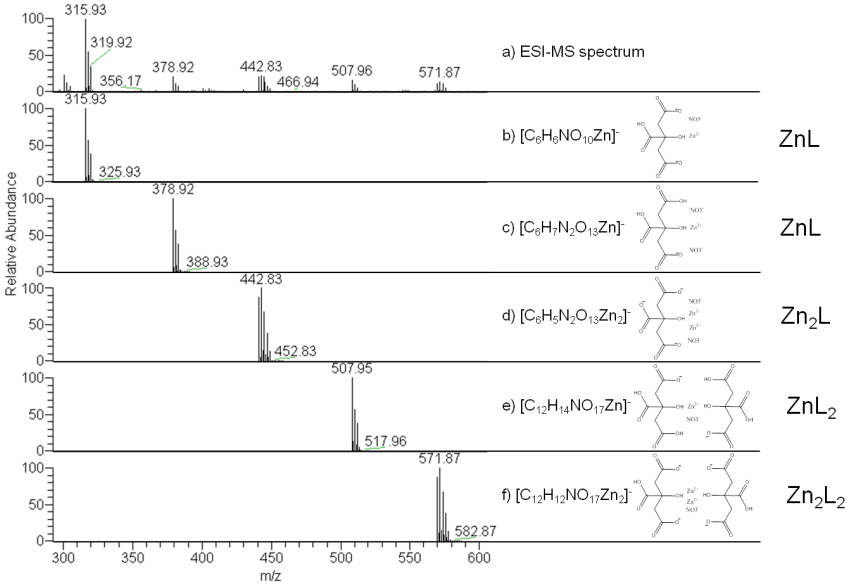

Figure A.3.: Electrospray ionization mass spectrometry analysis of a mixture of $Zn(NO_3)_2$ and citric acid in ethanol. a) ESI-mass spectrum recorded in anion mode and b - f) calculated MS-spectra of the corresponding mass fragments as well as the stoichiometry for zinc and citric acid ligand (L).

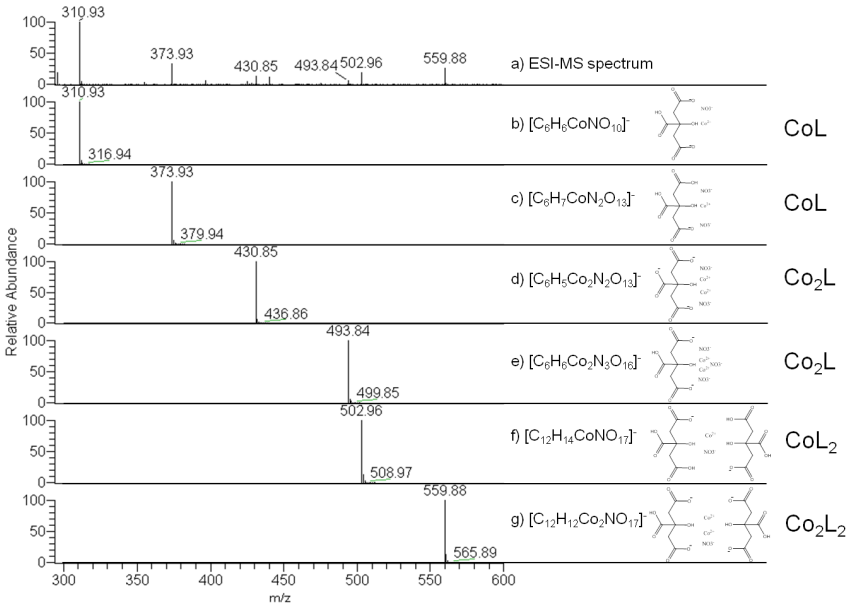

Figure A.4.: Electrospray ionization mass spectrometry analysis of a mixture of $Co(NO_3)_2$ and citric acid in ethanol. a) ESI-mass spectrum recorded in anion mode and b - g) calculated MS-spectra of the corresponding mass fragments as well as the stoichiometry for cobalt and citric acid ligand (L).

Analysis of Gaseous Decomposition Products of the Precursor Complex

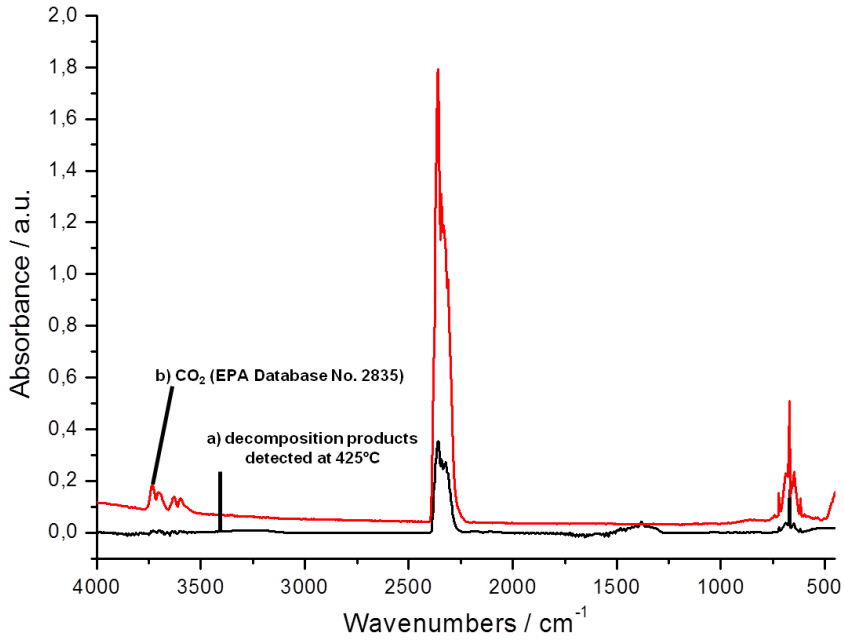

Figure A.5.: Infrared spectrum of the gaseous decomposition products recorded at 425 °C during thermal decomposition analysis of the precursor complex in air (a). Curve (b) shows for comparison the reference spectrum of carbon dioxide (EPA Database No. 2835). Based on the spectra CO_2 is concluded to be the major decomposition product. The CO_2 formation results from decomposition of the carbonate intermediate.

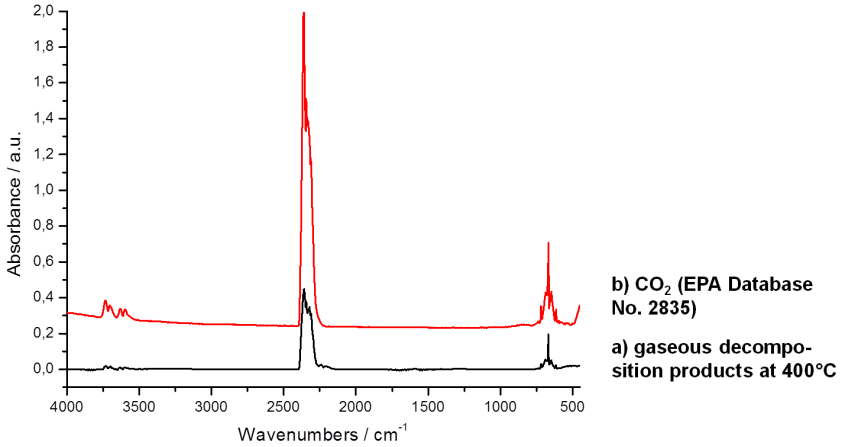

Figure A.6.: Infrared spectrum of (a) the gaseous decomposition products recorded during thermal decomposition analysis of the aluminum precursor complex in air at 400 °C. Curve (b) shows for comparison the reference spectrum of carbon dioxide (EPA Database No. 2835). The spectra evidence that CO_2 is the main decomposition product, whereas no significant amounts of water are detected. CO_2 formation can result from two processes, either the decomposition of aluminum carbonate or the oxidation of organic residue. However, since water formation is not observed, thermal decomposition of a carbonate intermediate is concluded to be the main source of CO_2 formation.

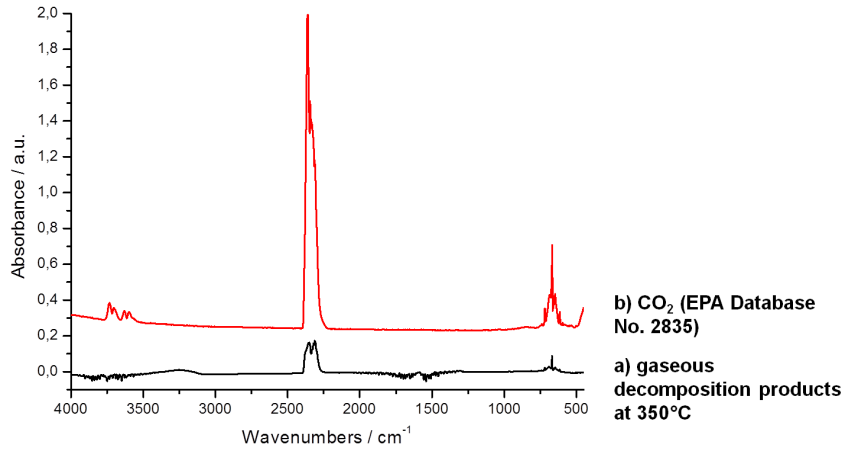

Figure A.7.: Infrared spectrum of (a) the gaseous decomposition products recorded during thermal decomposition of the zinc-precursor complex in air at 350 °C. Curve (b) shows for comparison the reference spectrum of carbon dioxide (EPA Database No. 2835). The spectra evidence that CO_2 is the main decomposition product, whereas no significant amounts of water are detected. CO_2 formation can result from two processes, either the decomposition of zinc carbonate or the oxidation of organic residue. However, since water formation is not observed, thermal decomposition of a ZnCO3 intermediate is concluded to be the main source of CO_2 formation.

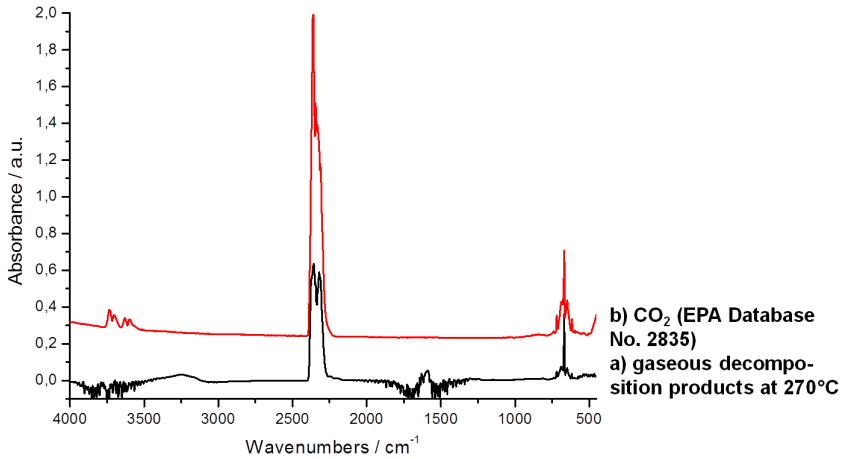

Figure A.8.: Infrared spectrum of (a) the gaseous decomposition products recorded at 270 °C during thermal decomposition analysis of the cobalt precursor complex in air. Curve (b) shows for comparison the reference spectrum of carbon dioxide (EPA Database No. 2835). The spectra evidence that CO_2 is the main decomposition product, whereas a significant amount of water is detected as well as signals corresponding to C-H vibrations. CO_2 formation can result from two processes, either the decomposition of cobalt carbonate or the oxidation of organic residue. Although, water formation is observed, thermal decomposition of a carbonate intermediate is concluded to be the main source of CO_2 formation. Nevertheless, additional bands corresponding to C-H vibrations and water suggesting the presence of residues of citric acid in the cobalt-precursor complex.

Characterisation of Micelle-Templated Metal Carbonates and Oxides by TEM

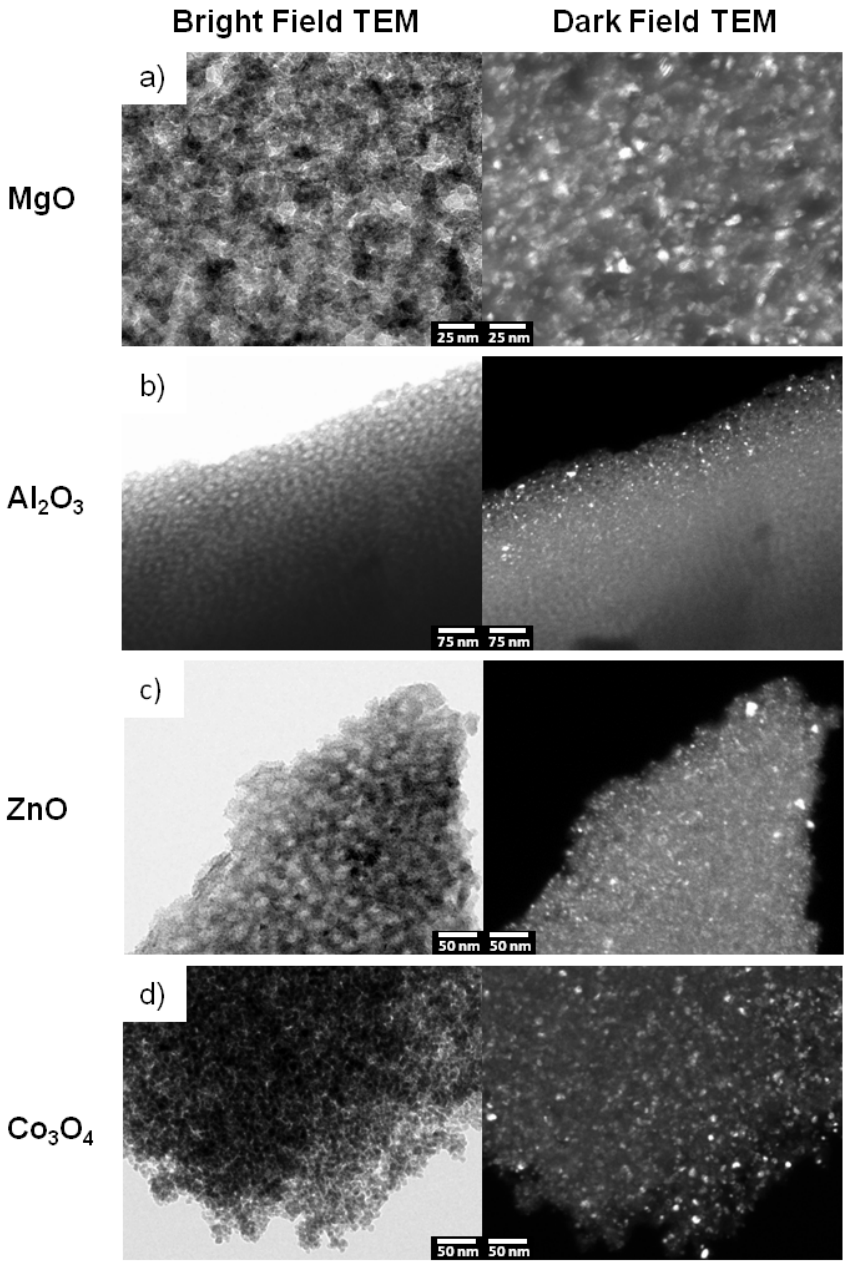

Figure A.9.: Bright field and dark field TEM images of a) MgO b) Al_2O_3 c) ZnO and Co_3O_4

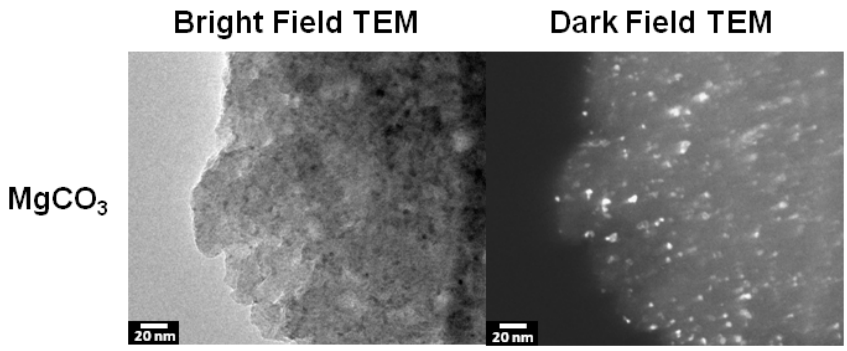

Figure A.10.: Bright field and dark field TEM images of $MgCO_3$

Characterisation of MgO and Li@MgO OCM Catalyst

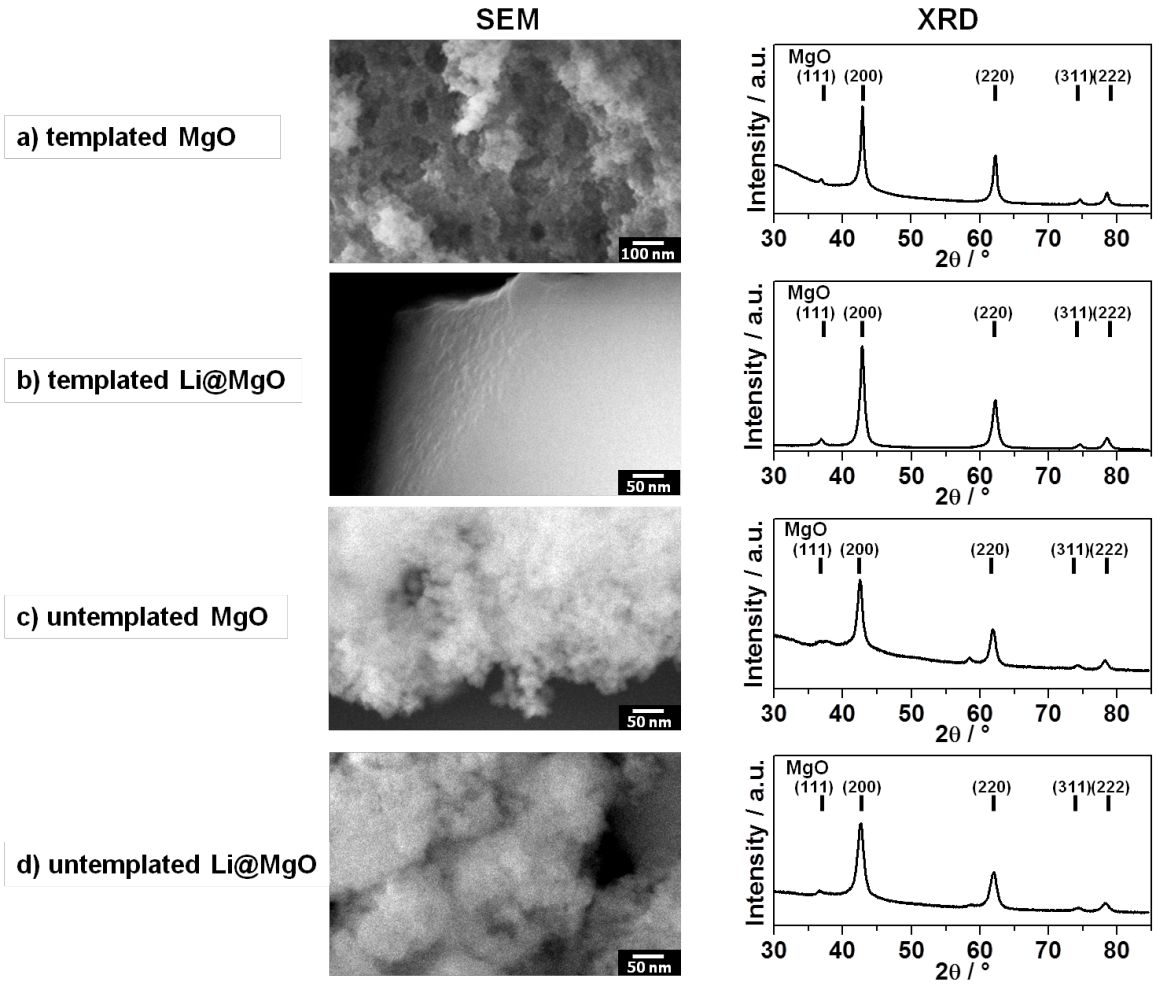

Figure A.11.: SEM images and XRD results obtained before catalytic testing of a) MgO powder prepared with PEO_{213}-PB_{184}-PEO_{213} template b) Li@MgO powder prepared with PEO_{213}-PB_{184}-PEO_{213} template c) MgO prepared without template d) Li@MgO prepared without template; the peak positions corresponding to MgO in periclase structure (PDF: 00-045-0946)

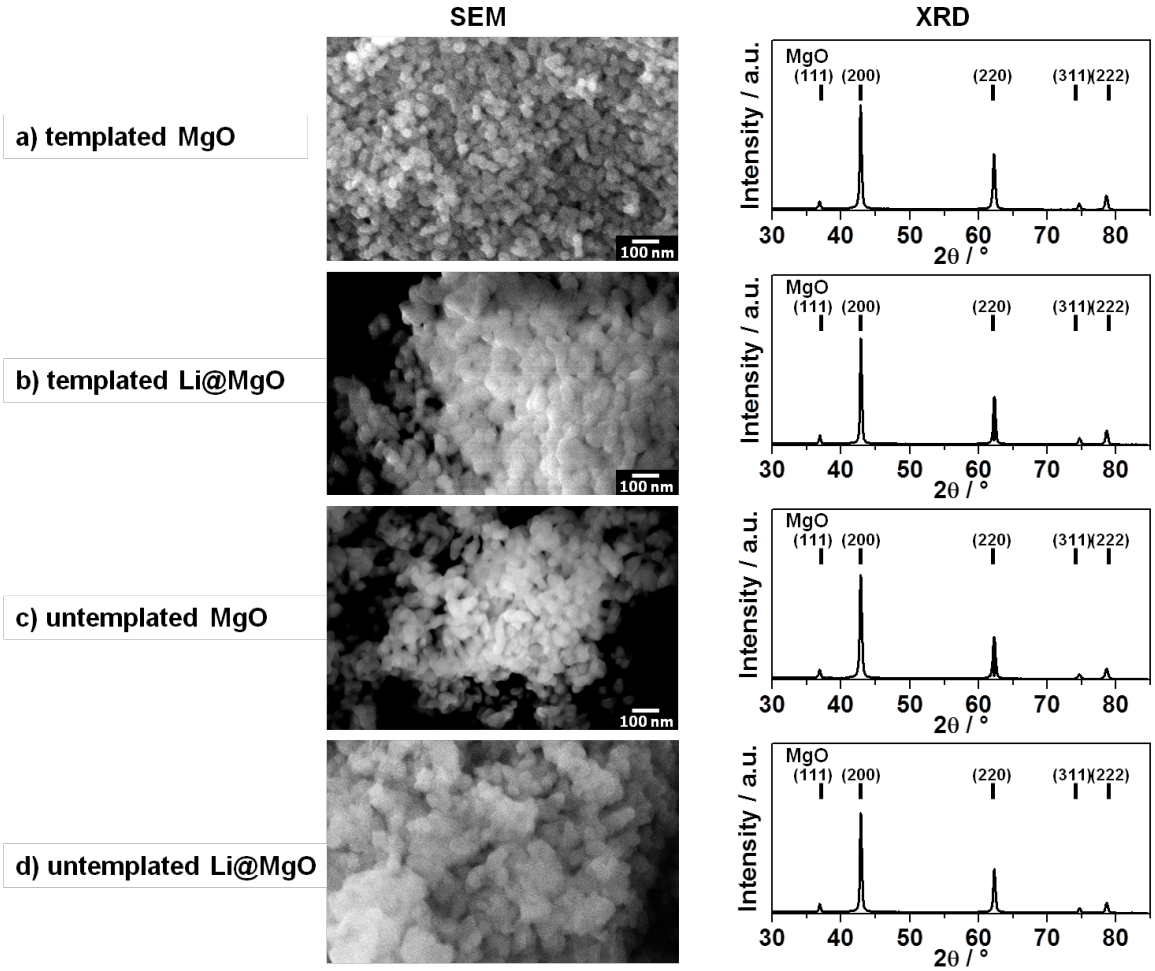

Figure A.12.: SEM images and XRD results obtained after catalytic testing of a) MgO powder prepared with PEO_{213}-PB_{184}-PEO_{213} template b) Li@MgO powder prepared with PEO_{213}-PB_{184}-PEO_{213} template c) MgO prepared without template d) Li@MgO prepared without template; the peak positions corresponding to MgO in periclase structure (PDF: 00-045-0946)

B. Acronyms

BET	Brunauer-Emmett-Teller method
BFTEM	Bright-field-transmission electron microscopy
BJH	Barrett-Joyner-Halenda
Brij56	$C_{16}H_{33}$-PEO_{10}-OH
cmc	Critical micelle concentration
CMK	Templated mesoporous carbon
CTAB	Cetyltrimethylammonium bromide
CTACl	Cetyltrimethylammonium chloride
DFTEM	Dark-field-transmission electron microscopy
EIMA	Evaporation-induced micelle assembly
EISA	Evaporation-induced self-assembly
ESI-MS	Electron spray ionisation mass spectra
F127, P123, F108	PEO_x-PPO_y-PEO_x (Pluronic)
FFT	Fast fourier transformed
FTIR	Fourier transform infrared spectroscopy
HRTEM	High-resolution-transmission electron microscopy
KLE	PHB_x-PEO_y
Li@MgO	Lithium doped magnesium oxide
MCM	Mobil crystalline materials - type of templated mesoporous silica
NLDFT	Non-local density functional theory
OAc	Acetate
OCM	Oxidative coupling of methane
OER	Oxygen evolution reaction
PB	Polybutadiene
PDF	Power diffraction file
PEO	Polyethylenoxide
PI	Polyisoprene

PIB	Polyisobutylene
PMA	Polymethyacrylate
PPO	Polypropylenoxide
PS	Polystyrene
PSD	Pore size distribution
SAED	Selected area electron diffraction
SAXS	Small angle X-ray scattering
SBA	Santa Barbara amorphous - type of templated mesoporous silica
SEM	Scanning electron microscopy
TEM	Transmission electron microscopy
TG	Thermogravimetry
XRD	X-ray diffraction

C. Curriculum Vitae

Persönliche Daten

Name:	Björn Eckhardt
Geburtsdatum und -ort:	07.08.1984 in Königs Wusterhausen

Schulische Ausbildung

1991 - 1997	Grundschule 3 Königs Wusterhausen
1997 - 2004	Friedrich-Schiller-Gymnasium in Königs Wusterhausen
Abschluss:	Abitur

Studium

2004 - 2009	Technische Universität Berlin im Fach Chemie mit Vertiefung der anorganischen und metallorganischen Chemie
Thema der Diplomarbeit:	"Beiträge zur Synthese p-dotierter transparenter leitender Oxide (TCO)"

Promotion

2010 - 2011	"Abscheidung von Halbleiternanopartikeln auf transparenten Kontaktflächen" am Helmholtz Zentrum Berlin
seit 01.02.2011	Promotion im AK Krähnert

List of Publications

BE1	B. Eckhardt, E. Ortel, J. Polte, D. Bernsmeier, O. Görke, P. Strasser, R. Kraehnert, "Micelle-Templated Mesoporous Films of Magnesium Carbonate and Magnesium Oxide", *Advanced Materials* **2012**, 24, 3115-3119
BE2	B. Eckhardt, E. Ortel, D. Bernsmeier, J. Polte, P. Strasser, U. Vainio, F. Emmerling, R. Kraehnert, "Micelle-Templated Oxides and Carbonates of Zinc, Cobalt, and Aluminum and a Generalized Strategy for Their Synthesis" *Chemistry of Materials* **2013**, 25, 2749-2758
BE3	B. Eckhardt, E. Ortel, D. Bernsmeier, R. Kraehnert, Patent, DE 10 2012 212 237 A1, *registered for patent approval*
BE4	S. Enthaler, K. Schröder, S. Inoue, B. Eckhardt, K. Junge, M. Beller, M. Drieß, "Formamidines - Versatile Ligands for Zinc-Catalyzed Hydrosilylation and Iron-Catalyzed Epoxidation Reactions", *European Journal of Organic Chemistry* **2010**, 4893-4901
BE5	S. Enthaler, S. Krackl, J. D. Epping, B. Eckhardt, S. M. Weidner, A. Fischer, "Iron-based precatalyst supported on polyformamidine for C-C bond formation" *Polymer Chemistry* **2012**, 3, 751-756

BE6 E. Zillner, J. Kavalakkatt, B. Eckhardt, T. Dittrich, A. Ennaoui, M. Lux-Steiner, "Formation of a heterojunction by electrophoretic deposition of CdTe/CdSe nanoparticles from an exhaustible source", *Thin Solid Films* **2012**, 520, 17, 5500-5503